

NORTHWESTERN UNIVERSITY

Combined *In Situ* Experimental and Computational Study on the Intrinsic Fracture Properties  
and Toughening of Two-dimensional Materials

A DISSERTATION

SUBMITTED TO THE GRADUATE SCHOOL  
IN PARTIAL FULFILLMENT OF THE REQUIREMENTS

for the degree

DOCTOR OF PHILOSOPHY

Field of Theoretical and Applied Mechanics

By

Xu Zhang

EVANSTON, ILLINOIS

June 2022

© Copyright by Xu Zhang 2022

All Rights Reserved

## ABSTRACT

Combined *In Situ* Experimental and Computational Study on the Intrinsic Fracture Properties and Toughening of Two-dimensional Materials

Xu Zhang

The successful isolation of graphene marked the advent of two-dimensional (2D) materials. Their atomically thin structures enable unprecedented electrical, optical, and mechanical properties, which have triggered significant research interests in the past decade. For instance, they are promising candidates for the fabrication of flexible electronics, biological sensors, battery electrodes, and electronic interconnects, etc. Despite the intriguing properties measured in the laboratories, industrial applications of 2D materials are still in the embryo. A major reason of such lag is the difficulties in the fabrication of 2D materials-based devices, which arise from their brittle nature. Toughening of 2D materials has thus become necessary toward reliable large-scale applications of 2D materials.

A better understanding of the mechanical failure of 2D materials necessitates detailed mechanistic studies at the atomic scale. Experimentally, such investigation requires the usage of *in situ* mechanical testing techniques inside transmission electron microscopy (TEM), with both high-fidelity mechanical testing capabilities and high-resolution characterizations. Computationally, molecular dynamics simulations enable one-to-one comparison to the atomic behaviors captured by TEM, and allow energetic and kinetic studies on lattice reconstructions and structural transitions associated to the fracture. Nevertheless, such combined study requires parametrized interatomic potentials with *ab initio* level accuracy on large deformation pathways, as well as a robust experimental protocol for conducting *in situ* fracture

tests inside TEM. As such, combined *in situ* experimental/computational studies on the fracture of 2D materials are scarcely reported.

The thesis is aimed at filling such a gap of knowledge. It describes a systematic *in situ* experimental/computational investigation on the fracture and toughening of 2D materials. It first presents a generally applicable framework for parameterizing interatomic potentials to accurately capture large deformation pathways with molecular dynamics simulations. The framework enables iterative definition of properties in the training and screening sets, guided by correlation relationships between properties, aiming to achieve optimal parametrizations for properties of interest. We parameterized interatomic potentials with *ab initio* level accuracy on large deformation pathways of monolayer MoSe<sub>2</sub> for the subsequent *in silico* study of the fracture of monolayer MoSe<sub>2</sub>. Next, a *in situ* TEM investigation on the edge-mediated annihilation of vacancy clusters in monolayer MoSe<sub>2</sub> was described. We showed that such behavior, triggered by electron beam irradiation, could be used to engineer the properties of 2D materials. Then, the thesis describes an integrated high-resolution TEM-numerical exploration on the intrinsic fracture properties of 2D materials. We reported the first experimental-computational measurements of the fracture toughness of 2D materials that agrees with each other, and with theoretical predictions according to the Griffith criterion. It next shows *in situ* TEM fracture tests conducted on monolayer MoSe<sub>2</sub> and reveals the extrinsic toughening effect from an ultra-thin polystyrene adlayer, which enhances the energy release rate of monolayer MoSe<sub>2</sub> by a maximum of 15 fold. Lastly, the thesis shows a systematic, quantitative study on the nanoscale toughening of monolayer graphene oxide (GO) by an ultra-thin polymer adlayer, which impedes the propagation of cracks during intraplanar fracture. Those results are anticipated to facilitate better understanding on the fracture of the 2D materials, and offer insights toward more reliable deployment of 2D materials in large-scale applications.

## Acknowledgements

The thesis is under my name but is not possible without the instruction, help, and encouragement of many others. First of all, I would like to thank my advisor, Professor Horacio D. Espinosa, for his consistent guidance through the six years of my PhD. Of all the things you have taught me, your extreme care on the subtlest details of research justifies your accomplishments and will always remind me of how high-quality work should be conducted. I would like to thank my committee members, Professor SonBinh Nguyen, Professor Sridhar Krishnaswamy, and Professor Cheng Sun for their guidance and help in evaluating the work I have conducted, and their suggestions for improving the quality of it.

Besides my advisor and committee members, I am also fortunate to receive the guidance from several senior researchers and professors. I would like to thank Dr. Jianguo Wen at Argonne National Laboratory for his continuous help on the experimental part of my thesis. I thank Professor Yip-Wah Chung for his instruction and guidance during my Master's study. I appreciate the help from Dr. Nicolaie Moldovan, Dr. Ralu Divan, Dr. Dafei Jin, Dr. Suzanne Miller at Argonne National Laboratory. I acknowledge the helpful suggestions from Professor Jeffrey Paci at University of Victoria. I would like to thank Professor Jose Mendoza-Cortes at Michigan State University on his suggestions.

I would like to thank many co-workers and collaborators for their contribution and help toward the completion of this thesis. In no particular order, I would like to thank Professor Matthew Daly at University of Illinois at Chicago, Yulin Lin at Argonne National Laboratory, Yu Lei at Argonne National Laboratory, Dr. Joon-Seok Kim at Northwestern University, and Dr. Xiang Zhang at Rice University for their help on different aspects of my thesis.

I would like to acknowledge the following funding agencies that support my PhD research: Ryan Fellowship of Northwestern University and the National Science Foundation through award CMMI 1953806. I would like to acknowledge the following institutes that provide resources and technological support for

the work I have conducted in my thesis: the NUFAB facility at Northwestern University, the Center of Nanoscale Materials at Argonne National Laboratory.

My colleagues at the Micro and Nanomechanics Laboratory make this lab feel like my second home. I thank Dr. Rafael Soler-Crespo who served as a senior mentor for me. I thank Dr. Samba Shiva Prasad Nathamgari for being a good example of a senior student. I thank Dr. Siyan Dong for his continuous guidance on the experimental aspect of my thesis. I thank Hoang T. Nguyen who works closest with me and teaches me with his expertise. I thank Zhaowen Lin for his help on the *in situ* experiments and accompany. I thank Graham Pritchard for assisting me with the experiments even at odd times. Toward the end of my PhD, I received numerous warm regards and encouragements from my colleagues. I would not be able to hold on without the emotional support from all of you. In no particular orders, I would like to thank Nicolas Alderete, Mohamed Ali, Jin Choi, Jin Hwang, Hanxun Jin, Prithvijit Mukherjee, Nibir Pathak, Cesar Patino. In no particular order, I thank the following previous colleagues: Professor Weidong Wang, Professor Lingqian Chang, Dr. Michael Chon, Dr. Rajaprakash Ramachondramoorthy, Dr. Ehsan Hosseinian, Professor David Restrepo, Dr. Alireza Zaheri, Dr. Zhenfei Song, Dr. Na Fan, Dr. Lior Medina and Dr. Meisam Asgari.

I thank the administrative staff at the Department of Mechanical Engineering, Pat Dyess, Sinta Kulanda, Rick Marzec, for their help on registration, purchasing, and IT-related issues.

I appreciate the love and support from my friends. I thank Drs. Ming Du, Songting Cai, Yanming Zhang, Weizi Yuan, and Furui Zhang, who filled the rest of my PhD beyond research with joy and happiness.

I would like to thank my parents (Chongli Zhang and Zhiye Xu), my brother (Hui Zhang), and my sister-in-law (Yuanyuan Feng) for their unconditional love that supports me through hard times. I thank my wife's parents (Wenying Wan and Deliang Du) for allowing me to have a lovely wife.

I thank my wife, Yao Du, who completes my life.

## Table of Contents

ABSTRACT	3
Acknowledgements	5
Table of Contents	7
List of Tables	10
List of Figures	11
Chapter 1. Introduction and Motivation	15
1.1. Two-dimensional Materials: Promises and Challenges	15
1.2. Bridging the Gap: Combined <i>In Situ</i> Experimental and Computational Explorations	17
1.3. Ongoing Challenges and Summary of Work	19
Chapter 2. Core Computational and Experimental Methods and Techniques	21
2.1. Materials Synthesis	21
2.2. Material Characterizations	21
2.3. Transfer of Two-Dimensional Materials	22
2.4. <i>In Situ</i> Experimental Methods	25
2.5. Computational Methods and Techniques	26
Chapter 3. Multiobjective Parametrization for Large Deformation Pathways of 2D Materials	37
3.1. Introduction	37
3.2. Parametrization Workflow	39
3.3. Parametrization Results	48

3.4. Correlation and Principal Component Analyses	54
3.5. Examination on Transferability	58
3.6. Chapter Summary	60
Chapter 4. Edge-Mediated Vacancy Annihilation of Monolayer Molybdenum Diselenide	64
4.1. Introduction	64
4.2. <i>In Situ</i> HRTEM Study of Vacancy Annihilation	65
4.3. Exploration of Thermodynamic Driving Force through Monte-Carlo Simulations	72
4.4. Kinetics Study via Nudged Elastic Band Simulations	79
4.5. Chapter Summary	84
Chapter 5. Quantification of Intrinsic Fracture Toughness of 2D Materials through Indirect Mechanical Testing	86
5.1. Introduction	86
5.2. <i>Ab Initio</i> Calculations for the Generation of Training, Screening, and Validation Data	87
5.3. Molecular Dynamics (MD) Simulations	88
5.4. Potential Optimization Framework	89
5.5. Calculation of Atomic Strain and the J-integral from HRTEM Images	90
5.6. Atomistic-to-continuum Mapping of the Displacement, Stress, and Strain Field	94
5.7. Indirect <i>In Situ</i> High-resolution Transmission Electron Microscopy (HRTEM) Fracture Tests	97
5.8. Molecular Dynamics (MD) Fracture Simulations	99
5.9. Atomic Configuration at the Crack Tip	100
5.10. Fracture Toughness Quantification	101
5.11. Chapter Summary	106
Chapter 6. <i>In Situ</i> Fracture Test of 2D MoSe <sub>2</sub> /Polymer	108
6.1. Introduction	108
6.2. <i>In Situ</i> Fracture Test	109

6.3. Chapter Summary	116
Chapter 7. Computational Exploration of Extrinsic Toughening of Graphene Oxide with Ultra-thin Polymer Adlayers	118
7.1. Introduction	118
7.2. General Considerations of the Molecular Dynamics Simulations	120
7.3. Crack-opening Simulation Setup	120
7.4. Single-chain Pull-off Simulation Setup	122
7.5. Selection of Model Systems	124
7.6. Adsorption of Polymer Chains on GO	127
7.7. Crack-opening Simulation Results	129
7.8. Single-chain Pull-off Simulation Results	135
7.9. Comparison Between the Multi-chain Crack-opening and Single-chain Pull-off Simulations	138
7.10. Chapter Summary	142
Chapter 8. Concluding Remarks and Outlook	144
References	146

## List of Tables

2.1	Allowable range for parameters of the Buckingham potential in the optimization	29
2.2	Allowable range for the SW potential parameters during the optimization	30
2.3	Tersoff parameters for Mo-Mo pair interactions	33
2.4	Allowable range for the parameters of the Tersoff potential during optimization	34
3.1	Weights for bond dissociation energy landscapes and uniaxial tension	47
3.2	Comparison of the parameterized interatomic potentials with <i>ab initio</i> results	50
3.3	Parameters of the parameterized Buckingham potential	51
3.4	Parameters of the parameterized SW potential	51
3.5	Parameters of the parameterized Tersoff potential	52
4.1	Probability of annihilation for the vacancy clusters under different initial edge configurations	77
5.1	Probability of annihilation for the vacancy clusters under different initial edge configurations	92

## List of Figures

1.1	Schematic of the potential applications of representative two-dimensional materials	16
1.2	Characteristic size and resolution of nanoscale computer simulations and experimental techniques	18
2.1	Raman spectra of monolayer MoS <sub>2</sub> and MoSe <sub>2</sub>	22
2.2	Schematics of the PDMS-based transfer method	23
2.3	Schematic of the polystyrene-assisted sample transfer method	25
3.1	Schematic of force field selection and parametrization approach	41
3.2	Target properties of monolayer MoSe <sub>2</sub> and Se systems	43
3.3	<i>Ab initio</i> uniaxial stress-strain curves	44
3.4	Prediction results of the parameterized interatomic potentials in comparison to <i>ab initio</i> results as well as existing SW and SNAP potentials.	53
3.5	Correlation matrix of the Tersoff potential	56
3.6	Correlation matrix for the Buckingham potential	57
3.7	Correlation matrix for the SW potential	58
3.8	Transferability test for the parametrized potentials (Tersoff and Tersoff-ZTL) on edge stability of monolayer MoSe <sub>2</sub>	60
3.9	Transferability test for the parameterized Tersoff potentials (Tersoff and Tersoff-ZTL) on thermal properties of monolayer MoSe <sub>2</sub>	61
4.1	Quantification of vacancy density	66

4.2	(a) A MoSe <sub>2</sub> flake that fractures after transfer. (b) Selected area diffraction of a region in (a)	67
4.3	Evolution of the morphology of monolayer MoSe <sub>2</sub> under electron beam irradiation of (a) 4.8 s and (b) 44.8 s	67
4.4	Vacancy annihilation under electron beam irradiation	69
4.5	Vacancy annihilation under electron beam irradiation, conducted under the same experimental condition as that shown in Fig. 4.4 for (a) 1.6 s and (b) 24 s of beam irradiation	70
4.6	Atom column mapping from intensity profile	71
4.7	VA representative Monte Carlo (MC) simulation of the vacancy annihilation process at 300 K	73
4.8	Coordination number of a vacancy cluster	75
4.9	Initial configuration for the MC simulation with Mo-Klein edge introduced randomly into the system	76
4.10	NEB simulation results of first-principle simulations versus the parameterized Tersoff potential for diffusion of Mo vacancy	78
4.11	NEB simulation results of first-principle simulations versus the parameterized Tersoff potential for diffusion of Se <sub>2</sub> divacancy	80
4.12	Proposed vacancy annihilation process for vc1	81
4.13	NEB simulation results of first-principle simulations versus the parameterized Tersoff potential for diffusion of Se <sub>2</sub> divacancy	83
5.1	(a) Definition of the area for the computation of J-integral. (b) $\frac{\partial q}{\partial x_1}$ for the corresponding area in (a)	93
5.2	Comparison between <i>ab initio</i> and fitted Green-Lagrangian strain-2 <sup>nd</sup> Piola-Kirchhoff stress for uniaxial tension along the armchair (a) and zigzag (b) direction	94

5.3	The continuum stress, strain, and displacement fields mapped from the discrete atoms	96
5.4	Lattice structures, crack initiation, and atomic configurations at the crack tip	98
5.5	Atomic strain and stress field near the crack tip	102
5.6	Fracture toughness measurements of various two-dimensional materials	105
5.7	Integrated experimental/computational framework to explore the intrinsic fracture properties of 2D materials.	106
6.1	<i>In situ</i> TEM fracture test setup and results of test 1	112
6.2	<i>In situ</i> TEM fracture test setup and results of test 2	113
6.3	Energy release rate computed from test 1 and test 2	115
6.4	<i>In situ</i> TEM fracture test under cyclic loading conditions with different maximum displacements	116
7.1	Rate-dependent behaviors of the crack-opening simulations for representative hydrogen-bonding and vdW-interaction GO-polymer systems	121
7.2	Single-chain pull-off simulations for various polymers. The letter a-e represent curves for PAA, PMA, PBA, PVA and PEG, respectively. The numeral 1-3 represent $F$ , $F/N$ and $N_{HB}/N$ for each polymer, respectively	123
7.3	Model polymer systems including poly(acrylic acid) (PAA), poly(methyl acrylate) (PMA), poly(butyl acrylate) (PBA), poly(vinyl alcohol) (PVA), and poly(ethylene glycol) (PEG) classified according to the type of HB species and relative strength of vdW interactions	126
7.4	Adsorption of polymer chains on GO	129
7.5	Critical energy release rate with polymer crack-bridging	131
7.6	Schematic illustrations of the GO-PAA simulation system	133
7.7	Results of the crack-opening simulations	134

7.8	Results of the single-chain pull-off simulations for models comprising a 9.7-nm-long polymer chain (27 repeating units for PEG and 40 for all other polymers) adsorbed on an 11 x 3.2 nm <sup>2</sup> GO sheet	137
7.9	HB analysis in the single-chain pull-off simulations	141

## CHAPTER 1

## Introduction and Motivation

### 1.1. Two-dimensional Materials: Promises and Challenges

Advancement of human civilization is triggered by evolution of materials. In the current era, space explorations require lightweight materials with excellent strength and toughness; electronics demand further shrinking of transistor sizes while maintaining performance and reliability. Continuous improvements on the synthesis, manufacturing, and processing of traditional materials have caught up with those requirements but seem to approach the bottleneck due to intrinsic limitations of the materials. For example, the carrier mobility and transport along the thin-body channel of bulk semiconductor materials degrade significantly for thicknesses below 3 nm. Such intrinsic limitations restrict further reduction of the size of the materials, and call for new materials that are fundamentally different from their bulk counterparts.

Two-dimensional (2D) materials represent a growing family of materials that may lead to breakthroughs in several areas including structural materials, electronics, and sensors, etc. Since the successful isolation of graphene, numerous groups of 2D materials have been discovered and stabilized in their monolayer forms, as shown in Fig. 1.1. Some representative 2D materials and their potential applications are discussed below.

MXenes are described by the general formula  $M_{n+1}X_nT_n$ , where M is a transition metal, X is either carbon or nitrogen, and T is surface terminations such as O, OH, F, and Cl. The first MXene ( $Ti_3C_2$ ) was discovered in 2001 [1], and since then, numerous applications of MXenes have been explored including batteries [2, 3], catalysis [1, 2, 4], sensors [1, 2], pollution treatment [5], electromagnetic shielding [6], and cancer treatment [7]. Specifically,  $Ti_3C_2$  possesses a high theoretical adsorption capacity of Li-ion (320 mAh/g), approaching that of the commonly used graphite and thus making it a promising anode material for lithium ion batteries [1].

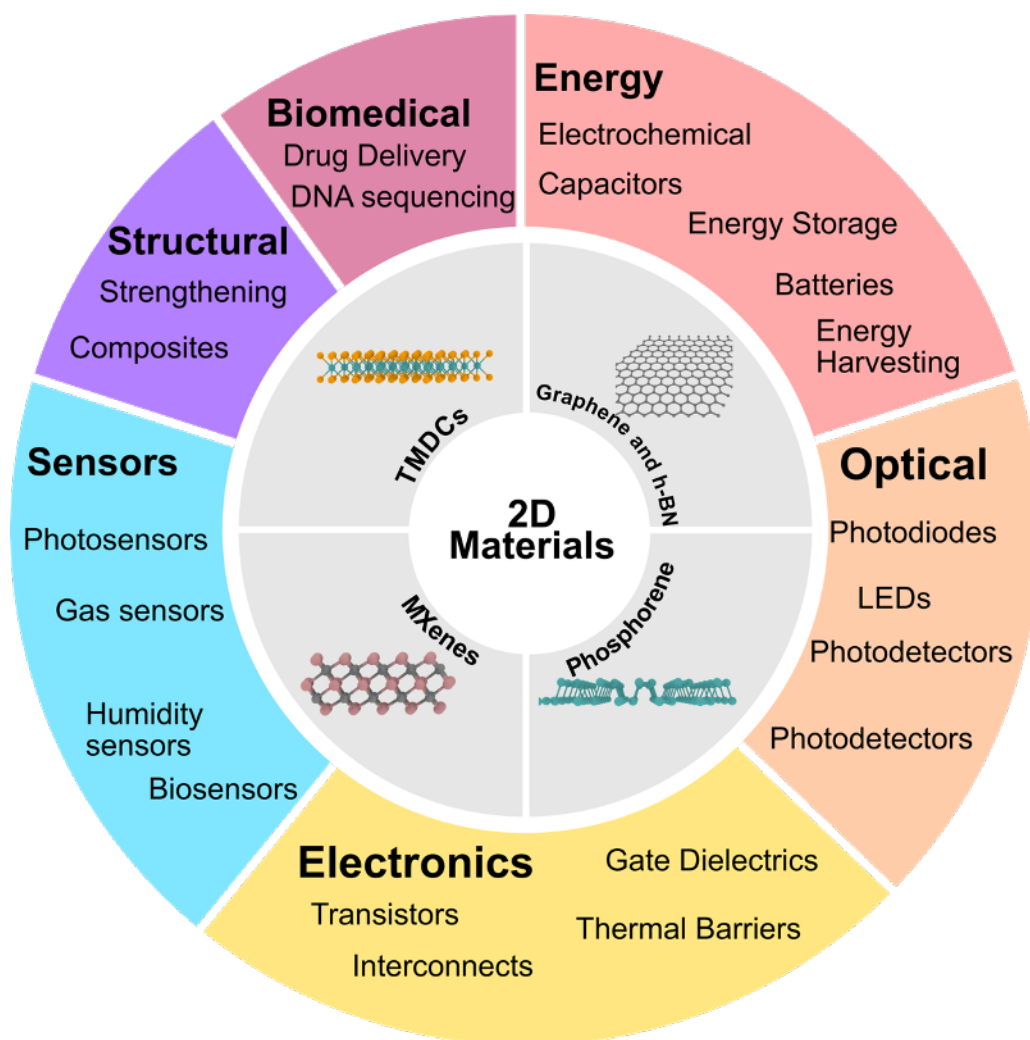


Figure 1.1. Schematic of the potential applications of representative two-dimensional materials.

Transition metal dichalcogenides (TMDCs) are a family of 2D materials of the type  $\text{MX}_2$ , where M is a transition metal atom (such as Mo or W) and X is a chalcogen atom (such as S, Se or Te) [8]. TMDCs have been extensively investigated due to their unique optical [9], electrical [10], electronic [11], and mechanical properties [12], which enable new applications and technological breakthroughs. For instance, TMDCs have contributed to the development of next-generation electronics and sensor technologies, as well as energy production and storage techniques [13], including supercapacitors [14], solar cells [15], and hydrogen production [16].

One advantage of 2D materials over conventional materials is their intrinsic flexibility originating from their atomic thicknesses. Alongside their excellent electro-mechanical properties, this flexibility offers huge potential for energy storage and harvest in wearable electronics [17], such as a recent MoS<sub>2</sub>-based flexible device that can harvest energy from a Wi-Fi-band channel. This functionality opens possibilities for ubiquitous wireless charging of wearable and implantable medical sensors [18]. However, such applications involve frequent mechanical deformations such as stretching and bending, so the lifespan (integrity and reliability) of the material is a critical feature. Its assessment requires an in-depth understanding of atomic interactions and the role of defects on mechanical properties. Most 2D materials exhibit high strength and stretchability but their failure is abrupt and unpredictable. Moreover, it is difficult to make devices based on defect-free 2D materials. Hence, fracture is a major concern in most applications. Fracture in 2D materials is also of high scientific significance [19]. Indeed, these materials exhibit several atomistic features associated with the progression of fracture. For instance, discrete lattice-trapping effects can lead to a toughness higher than the material surface energy [20]. Likewise, atomic lattice reconstruction at crack tips, from hexagon to pentagon, have been observed in graphene [21] and MoS<sub>2</sub> [22] via atomistic simulations and *in situ* transmission electron microscopy experiments. The interaction of cracks with defects near the crack tip can also lead to localized vs. catastrophic failure mode transition, as shown by AFM membrane deflection experiments performed on defective graphene [23]. Likewise, some TMDCs exhibit phase transformations [24]. These features (especially phase transformation and its interaction with atomic defects) are of high scientific importance, as their presence increases the energy required to propagate cracks and therefore favorably affect the integrity and reliability of 2D materials in applications of interest.

## 1.2. Bridging the Gap: Combined *In Situ* Experimental and Computational Explorations

The atomically-thin thickness of 2D materials, together with the local lattice reconstructions at the crack tip during crack propagation, necessitates atomic-scale characterization and exploration of the failure of 2D materials. Some unique experimental and computational techniques that are powerful at this

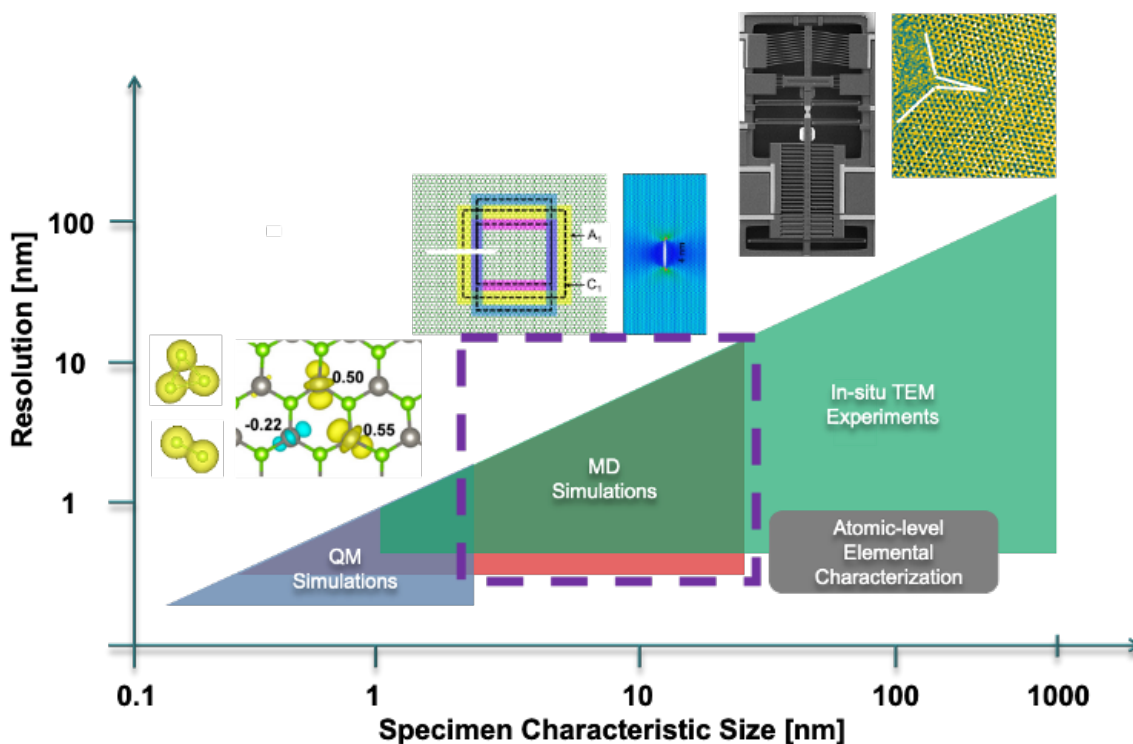


Figure 1.2. Characteristic size and resolution of nanoscale computer simulations and experimental techniques.

scale are summarized in Fig. 1.2. Computationally, *ab initio* simulation based on density functional theories (DFT) provides accurate results at the sub-to-few nanometers regime. For typical supercomputer clusters, the scale of *ab initio* simulations remains within a few nanometers. Nevertheless, equilibrium properties obtained from such simulations are representative and often serve as benchmarks for simulations at larger scale. Molecular dynamics (MD) simulations expand from *ab initio* simulations in both spatial (up to 100 nanometers) and temporal limits (up to nanoseconds). It is particularly powerful in revealing transient behaviors at the non-equilibrium regime, e.g., during crack propagation.

Experimentally, transmission electron microscopy (TEM) have pushed the spatial resolution to sub-angstrom scale with the aid of field emission gun and aberration correction, enabling detection of single atoms and buried defects in three dimensions. In the past decade, many sophisticated additions have been introduced into the TEM, which enable heating, mechanical deformation, and liquid environment in

an *in situ* manner [25]. In particular, The Espinosa group was one of the first to develop microelectromechanical systems (MEMS) for *in situ* electron microscopy mechanical testing of nanomaterials, providing electronic measurement of the load while enabling simultaneous acquisition of atomic structures. Using this technology, we have obtained the first satisfactory correlation of experimental measurements of carbon nanotube (CNT) elasticity and strength with quantum mechanical predictions.

Combined computational/*in situ* experimental explorations offer unprecedented insights toward the investigation of atomistic mechanisms. Ideally, the same atomic behaviors, e.g., lattice reconstructions, structural transitions, would be captured by both atomistic simulations and *in situ* experiments. Such an agreement enables not only validation of the atomistic simulations but also detailed mechanistic understanding through the energetic and kinetic explorations. However, to bridge the gap between computer simulations and experimental explorations, several barriers await to be overcome, as discussed below.

### 1.3. Ongoing Challenges and Summary of Work

Due to the complexity in deformation processes present in 2D materials, there are significant computational and experimental barriers that need to be overcome. Computationally, there are discrepancies in the results reported in the literature even based on first-principle calculations, e.g., in the mechanical behavior of single-layer MoS<sub>2</sub> [26]. Furthermore, despite properly configured density functional theory (DFT) calculations, the domain sizes required to model fracture exceed computational capabilities, even in state-of-the-art supercomputers. While MD simulations of such domains can be carried out, there is a scarcity of validated potentials (force fields) that can capture the chemistry of bond breaking, especially beyond graphene. For instance, several force fields have been obtained for MoS<sub>2</sub> [22, 27], yet their predictive capability in simulating other TMDCs remains unclear. For example, in MoS<sub>2</sub>, some models show a stiffening effect, while others predict a relatively brittle behavior under uniaxial tension.

Experimentally, scarcity is even more pronounced due to challenges in preparation of monolayer samples and availability of testing microsystems that can provide needed resolution in force and displacement measurements. The most common technique to study the mechanical properties of 2D materials is atomic force microscopy (AFM) membrane deflection tests. Using this technique, elasticity and strength

of certain materials such as graphene, graphene oxide, and MoS<sub>2</sub> have been extensively studied [28]. However, while the approach is popular due to its simplicity, it has notable limitations. It introduces highly non-uniform local stress and strain distributions within the 2D membrane, which complicates the extraction of intrinsic mechanical properties-especially if sources of nonlinearity arise. Furthermore, atom displacements and atomic bond breakage, which dominate the fracture of 2D materials, cannot be directly quantified or visualized during AFM indentation tests. This highlights the need for the development of an *in situ* electron microscopy nanomechanical testing method where displacement, load, and atomic scale imaging can be acquired simultaneously. Furthermore, direct observation of crack tips under stress facilitates the formulation of a computational framework that would fill the gap in current measurements and analyses.

The work in this thesis is aimed at addressing the aforementioned challenges in exploring the fracture of 2D materials through combined *in situ* experimental/computational approach. The rest of the thesis is organized as follows. Chapter 2 summarizes the key experimental and computational techniques. Chapter 3 describes multi-objective parametrization of interatomic potentials for large deformation pathways and fracture of two-dimensional (2D) materials. Chapter 4 summarizes an *in situ* TEM investigation of vacancy annihilation observed in monolayer MoSe<sub>2</sub> under continuous electron beam irradiation, which could be utilized for defect-engineering in 2D materials. In Chapter 5, an integrated *in situ* TEM/computational exploration on the intrinsic fracture properties of 2D materials is discussed. Chapter 6 discusses the *in situ* fracture tests conducted on monolayer MoSe<sub>2</sub> with polystyrene adlayer, which toughens the monolayer MoSe<sub>2</sub> through an extrinsic toughening mechanism. Chapter 7 discusses computational exploration of the design criteria toward better extrinsic toughening of graphene oxide ultrathin polymer adlayer. Finally, Chapter 8 summarizes the thesis and discusses future work.

## CHAPTER 2

**Core Computational and Experimental Methods and Techniques****2.1. Materials Synthesis**

MoS<sub>2</sub> and MoSe<sub>2</sub> flakes were synthesized by chemical vapor deposition. MoO<sub>3</sub> and Se/S powders were used as the precursors, and placed at the center and upstream of a tube furnace, respectively. SiO<sub>2</sub>/Si wafer was used as the substrate and placed on the top of MoO<sub>3</sub> powder. The growth was conducted at 750 °C for 15 min with H<sub>2</sub>/Ar (15%H<sub>2</sub>) as the carrier gas.

**2.2. Material Characterizations****2.2.1. Atomic Force Microscopy**

Atomic force microscopy (AFM) characterization was used to quantify the thickness of the polystyrene adlayer on monolayer MoSe<sub>2</sub>. The images were obtained in the tapping mode using a Park XE-120 AFM system (Park Systems, South Korea). Bruker TESP-V2 probe was used to scan a region of 5 x 5 μm<sup>2</sup>. A scan rate of 0.2-0.5 Hz was used to collect images. A 2.5:1 ratio was employed between proportional and integral gains, respectively.

**2.2.2. Raman Spectroscopy**

Raman spectroscopy was used to evaluate the quality of the as-received CVD-grown monolayer specimen. A 532 nm laser was used as the excitation source. The laser was focused on the sample to a spot of ~ 2 μm. A grating of 1800 grooves/mm was used. The peak location of Si (520.7 cm<sup>-1</sup>) was used to account for any drift in the spectrograph. The Raman spectra for a representative MoS<sub>2</sub> and MoSe<sub>2</sub> flake are shown in Fig. 2.1.

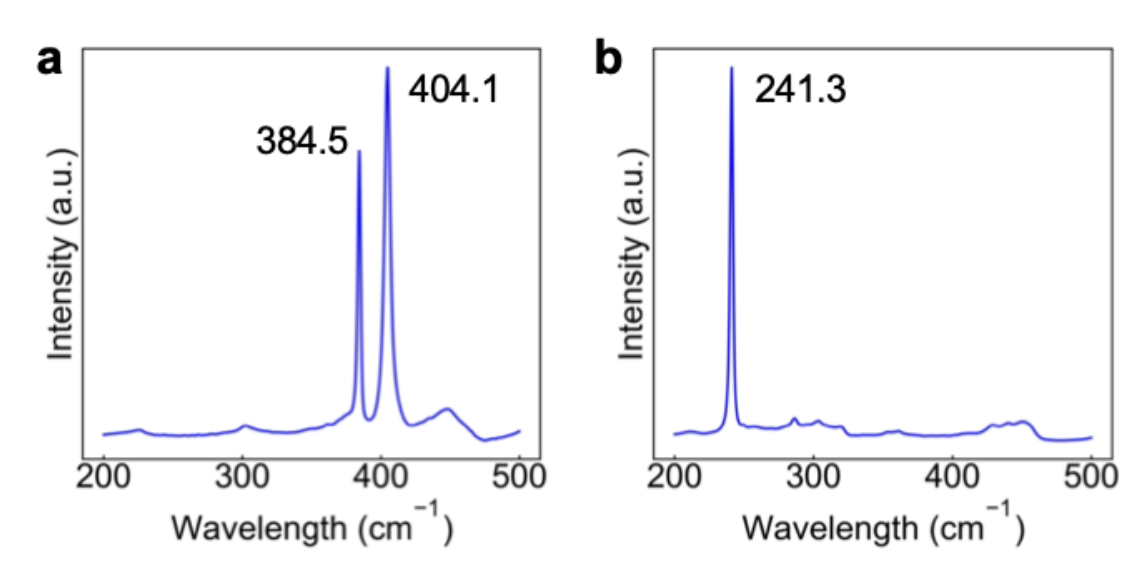


Figure 2.1. Raman spectra of monolayer MoS<sub>2</sub> and MoSe<sub>2</sub>.

### 2.3. Transfer of Two-Dimensional Materials

#### 2.3.1. PDMS-based Dry Stamping

The PDMS-based Dry Stamping was developed by Dr. Siyan Dong. A schematic of the transfer method is shown in Fig. 2.2. In this work, PDMS with protrusions of  $\sim 100 \mu\text{m}$  in lateral size and  $\sim 40 \mu\text{m}$  in height was prepared from an SU8 mold. Then, under an optical microscope, the protrusion was stamped gently on the flake of interest, followed by addition of water droplet near the protrusion to facilitate separation of 2D flakes from the growth substrate. Then, the flakes were stamped onto the holey Si<sub>3</sub>N<sub>4</sub> TEM grids (Ted Pella PELCO) TEM grid at  $\sim 70 \text{ }^\circ\text{C}$ .

#### 2.3.2. Polymer-assisted Transfer

Fig. 2.3 summarizes the protocols to transfer monolayer MoSe<sub>2</sub> flakes onto the push-to-pull (PTP) device with the polystyrene-assisted transfer method. We modified the polystyrene (PS)-based transfer method used by Gurarslan et al [29] by enabling better control on the quantity and positioning of the flakes per transfer attempt. 0.9 g of PS (Mw = 280000 g/mol) was dissolved in 20 mL of toluene at  $\sim$

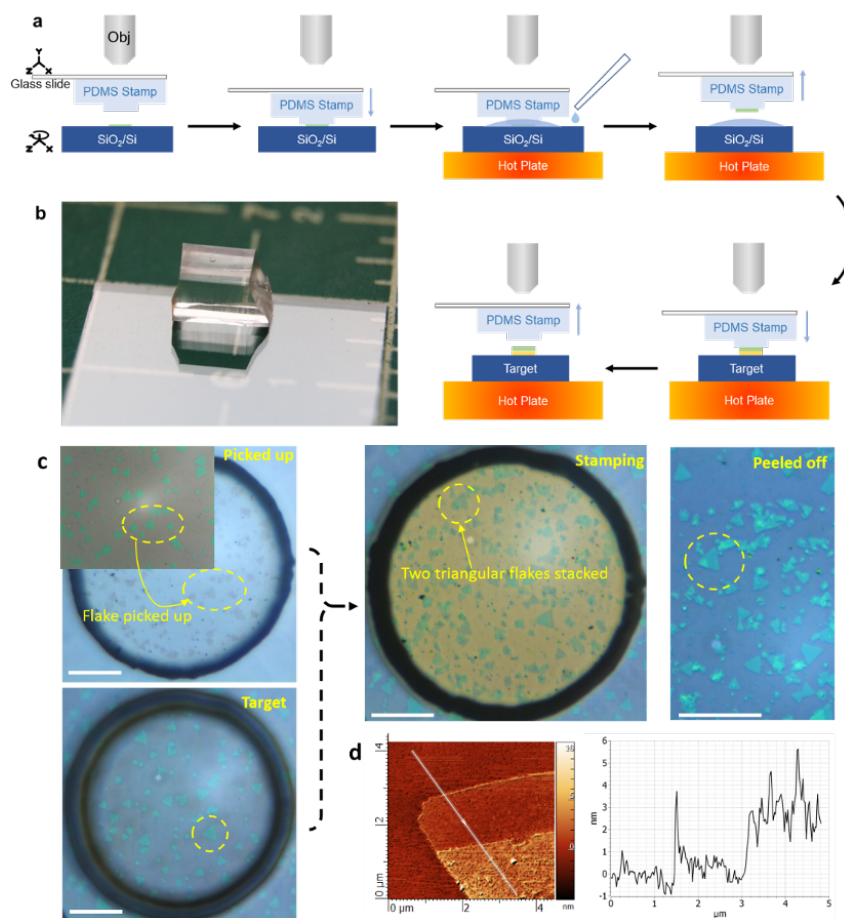


Figure 2.2. **Schematics of the PDMS-based transfer method.** (a) Pre-fabricated PDMS stamp with small rectangular extrusion is adhered to a glass slide and aligned to 2D materials of interest for pick-up. Then water is added around the interface to allow penetration and separation. After picking up the bottom is swapped with the target substrate and the picked up 2D material can be precisely positioned and transferred to any location on the target substrate. (b) Optical image of a PDMS stamp fabricated from a SU-8 mold. (c) Demonstration of the PDMS stamp selective transfer process. CVD MoSe<sub>2</sub> flakes were identified and picked up by the PDMS stamp with a circular protrusion area. Then the stamp was brought into contact with the target substrate. Using a slow peeling rate, all the flakes on the stamp were transferred to the target substrate and no changes of flake geometry or fractures were observed. Scale bars: 50  $\mu\text{m}$ . (d) AFM topography reveals perfect alignment accuracy and confirms 2D material steps assembled by the reported process.

50 °C and then spin-coated onto the growth substrate at 3500 rpm for 60 s. The substrate was baked at 90 °C for 15 minutes. Next, a rectangular piece of the PS film covering MoSe<sub>2</sub> flakes was sliced with

a scalpel blade (Integra<sup>TM</sup> Miltex<sup>TM</sup> Sterile #11 Scalpels), as shown in Fig. 2.3(b). The scalpel blade was mounted on a micro-manipulator and operated under a probe station for precise profiling. Next, an injection microcapillary (Eppendorf Femtotips) was used to inject water droplet next to the sliced PS film. The position of the microcapillary and injection of water was controlled by Eppendorf Injectman 2 and Eppendorf FemtoJet 4i. After injection, the PS film was poked from the edge to let water penetrate through the sliced PS film. As SiO<sub>2</sub>/Si wafer is more hydrophilic than the PS film and monolayer MoSe<sub>2</sub> flakes, the penetrated water preferably attacked the SiO<sub>2</sub>-MoSe<sub>2</sub> interface, causing the monolayer MoSe<sub>2</sub> flakes to stick onto the PS film. The as-purchased Femtotip has a very sharp tip ( $\sim 500$  nm) and tends to fracture during the poking process. Nevertheless, we found that a fractured Femtotip with a tip diameter of  $\sim 1$   $\mu$ m was more effective in poking the film. After the sliced PS film was completely separated from the underlying substrate, it was picked up by the microcapillary [30] and then dropped onto the push-to-pull (PTP) device (Fig. 2.3(c)). Prior to the drop-off process, water was injected onto the PTP device to facilitate the removal of the sliced PS film that typically stuck onto the sidewall of the microcapillary. A mild oxygen plasma cleaning on the PTP device prior to the drop-off process lowered the water contact angle and enabled easier positioning of the PS film. Next, the PS film was moved by the microcapillary to the target location on the PTP device. To align the crystallographic direction of the flake to the pulling direction of the PTP device, rotation of the PS film was also conducted. The PTP device surface was prevented from drying throughout the drop-off process. After successful positioning, the PTP device was heated on a hot plate at 70 °C for 1 hour and then at 110 °C for 5 minutes. The PTP device was then immersed in toluene/acetone mixture of 1:5 volume ratio at 25 °C. Fig. 2.3(d) shows successfully transferred monolayer MoSe<sub>2</sub> flake across the region of interest on the PTP device. The successfully transferred flakes were then cut into regular strips with focused ion beam (FIB) milling (30 kV, 9 pA, 2 nm cutting depth).

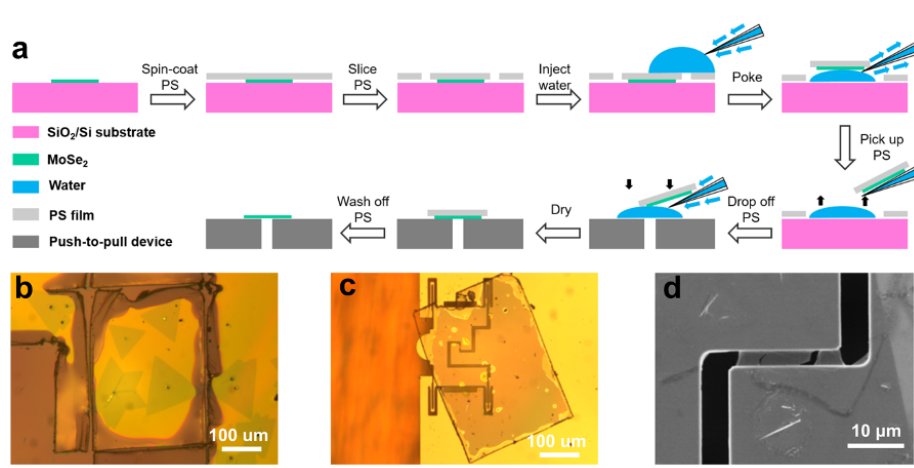


Figure 2.3. **Schematic of the polystyrene-assisted sample transfer method.** (a) Protocols for the transfer of CVD-grown MoSe<sub>2</sub> flakes onto the PTP device. (b) Optical microscopy (OM) image of a sliced PS film on top of monolayer MoSe<sub>2</sub> flakes. Scale bar: 100  $\mu\text{m}$ . (c) OM image of the PS film in (b) after being transferred to the PTP device. Scale bar: 100  $\mu\text{m}$ . (d) A suspended monolayer MoSe<sub>2</sub> across the gap of the PTP device.

## 2.4. *In Situ* Experimental Methods

### 2.4.1. TEM Characterization and Beam Irradiation

TEM characterization was conducted inside FEI Titan 80-300 (S)TEM and FEI Talos F200X (S)TEM. Specifically, the Titan 80-300 (S)TEM was equipped with image correctors that can correct both spherical and chromatic aberrations, enabling sub-angstrom resolution. Samples on TEM grids were heated to 120 °C for 30 minutes before the imaging to reduce the amount of adsorbed hydrocarbons. Acceleration voltage of 80 kV and 200 kV was used. HRTEM images were taken under conditions when spherical and chromatic aberration coefficients are corrected such that  $C_s < 5 \mu\text{m}$ , and  $C_c < 5 \mu\text{m}$ .

Electron beam irradiation was used to generate defects, heal vacancy clusters, and create cracks in the monolayer 2D specimens. For defect generation and healing of vacancy clusters, the intensity of the electron beam was adjusted such that the dose rate ( $\text{e}^- \cdot \text{nm}^{-1} \cdot \text{s}^{-1}$ ) approaches specified values. For the creation of cracks, the electron beam was shrunk to the shape of a slit by controlling both the intensity and the astigmatism. The direction of the slit was aligned to the crystallographic direction of the sample,

which was determined by selected area diffraction. Alternatively, the electron beam was focused to a spot at high-magnification ( $> 185$  kx), and moved manually along certain directions.

#### 2.4.2. *In Situ* Mechanical Testing

In situ fracture testing on monolayer MoSe<sub>2</sub> was conducted with Hysitron PI95 Picoindenter inside FEI Titan 80-300 (S)TEM and FEI Talos F200X (S)TEM. The Picoindenter was used with push-to-pull (PTP) devices to convert the indentation motion of the indenter tip to tensile force applied to the sample. The suspended monolayer sample was trimmed by focused ion beam to define a rectangular geometry. Next, the sample was loaded into the TEM followed by focused electron beam irradiation to create an initial crack and define a single-edge notched specimen. The initial crack was created to follow the zigzag direction of the suspended monolayer MoSe<sub>2</sub>. To achieve that, we took HRTEM images of the suspended sample and extracted the FFT pattern. The six spots closest to the center spot corresponded to the zigzag surface, and direction in the real space that is perpendicular to the six reciprocal vectors is thus the zigzag direction. A displacement-controlled fracture test was conducted by indenting at the protrusion of the PTP device, which drove one edge of the suspended sample away from the other and then stretched the sample. The interfacial adhesion was sufficient to prevent sliding of the suspended monolayer. The measured force was the sum of both the PTP device (which has an intrinsic stiffness) and the sample. To extract force from the sample, the measured force was subtracted from force from the PTP device (calculated by indenting on the PTP device after the sample failed completely).

### 2.5. Computational Methods and Techniques

#### 2.5.1. *Ab initio* Calculations

The training data for the optimization were created by *ab initio* calculations. These simulations were carried out using the density functional approach via SIESTA 4.0.2 software [31]. We applied the non-spin-polarized generalized gradient approximation (GGA) in the Perdew-Burke-Ernzerhof (PBE) form [32] together with the split polarized valence double-zeta (DZP) basis set [33]. For the molybdenum and selenium atoms, non-relativistic norm-conserving Troullier-Martins pseudopotentials [34] were utilized.

The energy shift and mesh cutoff were selected to be 250 eV and 300 Ry ( $\sim 4081$  eV), respectively, at which the energy convergence was attained. Geometry optimization was conducted without any symmetry constraints, until the forces acting on the atoms became lower than  $0.01 \text{ eV } \text{\AA}^{-1}$ . The interaction between monolayers (or molecules) were prevented by a  $40 \text{ \AA}$  vacuum layer. A monolayer thickness of  $7.726 \text{ \AA}$  was used to calculate per-area quantities (e.g. monolayer stresses). To achieve accurate electronic structure calculations, we allowed a  $15 \text{ \AA}$  cutoff for the set of k-points in the first Brillouin zone. The resultant k-grids were chosen in an optimal way, according to the method of Moreno and Soler (which utilized an effective supercell close to spherical shape, thus minimizing the number of k-points for a given precision) [35]. The self-consistent and the conjugate gradient minimization schemes were employed for the electronic-structure calculation and for the geometry optimization, respectively. The cohesive energy of a compound was computed from

$$E_{coh} = E_{pristine} - n_{Mo}E_{Mo} - n_{Se}E_{Se} \quad (2.1)$$

where  $E_{pristine}$  is the energy of the compound,  $E_{Mo}$  and  $E_{Se}$  are the energies of an isolated Mo and Se atom, and  $n_{Mo}$  and  $n_{Se}$  are the number of the corresponding atoms in the compound. The elastic constants were extracted from uniaxial stress-strain curves in the small-deformation regime. A fitting procedure reported by Cooper et al. [36] was used to extract the polynomial of the finite-deformation Green tensor of different orders, and the second-order terms were used in the screening process. Vacancy formation energies were calculated with the following equation:

$$E_f = E_{defected} + n_{Mo}\mu_{Mo} + n_{Se}\mu_{Se} - E_{pristine} \quad (2.2)$$

where  $E_{defected}$  is the energy of the defected system,  $E_{pristine}$  is the energy of the pristine system,  $n_{Mo}$  and  $n_{Se}$  are the number of missing Mo and Se atoms in the vacancy, and  $\mu_{Mo}$  and  $\mu_{Se}$  are chemical potentials for Mo in its stable BCC structure and Se in  $\text{Se}_8$  rings, respectively.

### 2.5.2. Phonon Dispersion Calculation

In order to obtain the phonon dispersion curves and densities of states, the theory of lattice dynamics on a Born-Oppenheimer surface was applied. Assuming that atomic displacements are in the form of plane-wave functions with different wave numbers, lattice vibration turns into an eigenvalue problem. Siesta [31] offers utility functions (e.g., *vibra* and *fcbuild*) that displace each atom in the monolayer and measure the reaction of other atoms to form the stiffness matrix. The wave dispersion along the path connecting symmetry points of the hexagonal lattice  $\Gamma - M - K - \Gamma$  in the first Brillouin zone for MoSe<sub>2</sub> monolayers were investigated. These points are located at (0,0,0), (0.5,0,0), and (0.333,0.333,0) in reciprocal space. These symmetry directions stem from the hexagonal lattice 2H MoSe<sub>2</sub>, similar to graphene. To sample the dispersion within the first Brillouin zone, a super cell of 4x4x1 repetitive unit cells was utilized to include all possible attenuations of the real-space force constants within it. To avoid interactions between monolayers, a vacuum layer of 40 Å was set.

### 2.5.3. Formulation of Interatomic Potentials

**2.5.3.1. Buckingham Potential.** The Buckingham potential has the following form:

$$E_{\text{total}} = E_{\text{short}} + E_{\text{long}} \quad (2.3)$$

where  $E_{\text{short}}$  represents short-range interactions given as

$$E_{\text{short}} = \sum_i \sum_{j>i} A \exp\left(-\frac{r_{ij}}{\rho}\right) - \frac{C}{r_{ij}^6} \quad r_{ij} < r_{c1} \quad (2.4)$$

$E_{\text{long}}$  denotes long-range Coulombic interactions. We adopted the Wolf summation method, a computationally efficient method in comparison to the Ewald summation, given as

$$E_{\text{long}}(r_{ij}) = \frac{1}{2} \sum_{j \neq i} \frac{q_i q_j \operatorname{erfc}(\alpha r_{ij})}{r_{ij}} + \frac{1}{2} \sum_{j \neq i} \frac{q_i q_j \operatorname{erf}(\alpha r_{ij})}{r_{ij}} \quad r_{ij} < r_{c2} \quad (2.5)$$

The  $q_{\text{Mo}}$  and  $q_{\text{Se}}$  were calculated from *ab initio* simulations as  $0.072 e$  and  $-0.036 e$ , respectively. Table 2.1 summarizes the allowable range for parameters that were optimized during the optimization. A total of 12 parameters were optimized.

Table 2.1. Allowable range for parameters of the Buckingham potential in the optimization

Parameter	Range
$A_{\text{Mo-Mo}}, A_{\text{Mo-Se}}, A_{\text{Se-Se}} (\text{eV})$	0 – 10000
$\rho_{\text{Mo-Mo}}, \rho_{\text{Mo-Se}}, \rho_{\text{Se-Se}} (\text{\AA}^{-1})$	0 – 1
$C_{\text{Mo-Mo}}, C_{\text{Mo-Se}}, C_{\text{Se-Se}}, (\text{eV}\text{\AA}^6)$	0 – 1000
$\alpha$	0 – 1
$r_{c1} (\text{\AA})$	7 – 10
$r_{c2} (\text{\AA})$	7 – 10

**2.5.3.2. Stillinger-Weber (SW) Potential.** The formulation of SW potential is as follows:

$$E = \sum_i \sum_{i>j} \phi_2(r_{ij}) + \sum_i \sum_{j \neq i} \sum_{k>i} \phi_3(r_{ij}, r_{ik}, \theta_{ijk}) \quad (2.6)$$

where  $\phi_2(r_{ij})$  is the two-body interaction term given as

$$\phi_2(r_{ij}) = A_{ij} \epsilon_{ij} \left[ B_{ij} \left( \frac{\sigma_{ij}}{r_{ij}} \right)^{p_{ij}} - \left( \frac{\sigma_{ij}}{r_{ij}} \right)^{q_{ij}} \right] \exp \left( \frac{\sigma_{ij}}{r_{ij} - a_{ij} \sigma_{ij}} \right) \quad (2.7)$$

and  $\phi_3(r_{ij}, r_{ik}, \theta_{ijk})$  is the three-body interaction term defined as

$$\phi_3(r_{ij}, r_{ik}, \theta_{ijk}) = \lambda_{ijk} \epsilon_{ijk} [\cos \theta_{ijk} - \cos \theta_{0ijk}]^2 \exp \left( \frac{\gamma_{ij} \sigma_{ij}}{r_{ij} - a_{ij} \sigma_{ij}} \right) \exp \left( \frac{\gamma_{ik} \sigma_{ik}}{r_{ik} - a_{ik} \sigma_{ik}} \right) \quad (2.8)$$

In the above equations, subscripts with three elements denote three-body interactions; the first element is the center atom  $i$ , followed by two atoms  $j$  and  $k$  that bond to it. Table 2.2 summarizes the allowable range for the parameters of SW potential during optimization. We set  $p$  and  $q$  for all pairs

(Mo-Mo, Mo-Se, and Se-Se) to be 5 and 0, respectively. Also, three-body interactions except Mo-Se-Se and Se-Mo-Mo were ignored. For such a purpose,  $\lambda$ ,  $\cos\theta_0$ , and  $\gamma$  for all the three-body terms except Mo-Se-Se and Se-Mo-Mo were set as zero. Lastly, we introduced an additional cutoff ( $4.05\text{\AA}$ ) to exclude three-body interactions for Mo-Se<sub>up</sub>-Se<sub>down</sub>, where Se<sub>up</sub> and Se<sub>down</sub> denote the Se atom above and below the center Mo atom. This pair of atoms has a different bond angle in comparison to the rest of the Mo-Se-Se pairs, and the exclusion of which was found to increase the overall accuracy of the SW potential. The bond angle of the rest of the Mo-Se-Se pairs and the Se-Mo-Mo pair are close ( $82.6^\circ$  versus  $81.2^\circ$ ). Thus, we used the same  $\cos\theta_0$  parameter for them.

Table 2.2. Allowable range for the SW potential parameters during the optimization

Parameter	Range or specified value
$A_{\text{Mo-Mo}}, A_{\text{Mo-Se}}, A_{\text{Se-Se}}$	0 – 30
$B_{\text{Mo-Mo}}, B_{\text{Mo-Se}}, B_{\text{Se-Se}}$	0 – 30
$p_{\text{Mo-Mo}}, p_{\text{Mo-Se}}, p_{\text{Se-Se}}$	5
$q_{\text{Mo-Mo}}, q_{\text{Mo-Se}}, q_{\text{Se-Se}}$	0
$\lambda_{\text{Mo-Mo-Mo}}, \lambda_{\text{Se-Se-Se}}$	0
$\lambda_{\text{Mo-Se-Se}}, \lambda_{\text{Se-Mo-Mo}}$	0 – 30
$\cos\theta_{0\text{Mo-Mo-Mo}}, \cos\theta_{0\text{Se-Se-Se}}$	0
$\cos\theta_{0\text{Mo-Se-Se}} = \cos\theta_{0\text{Se-Mo-Mo}}$	-1 – 1
$\gamma_{\text{Mo-Mo}}, \gamma_{\text{Se-Se}},$	0
$\gamma_{\text{Mo-Se}}$	0 – 2
$\epsilon_{\text{Mo-Mo}}, \epsilon_{\text{Mo-Se}}, \epsilon_{\text{Se-Se}} (\text{eV})$	1
$a_{\text{Mo-Mo}}, a_{\text{Mo-Se}}, a_{\text{Se-Se}}$	1 – 3
$\sigma_{\text{Mo-Mo}}, \sigma_{\text{Mo-Se}}, \sigma_{\text{Se-Se}} (\text{\AA})$	1 – 3

**2.5.3.3. Tersoff Potential.** The functional form for the Tersoff potential is described below:

$$E = \frac{1}{2} \sum_i \sum_{j \neq i} V_{ij} \quad (2.9)$$

$$V_{ij} = f_C(r_{ij}) [f_R(r_{ij}) + b_{ij} f_A(r_{ij})] \quad (2.10)$$

where  $f_C(r_{ij})$  is the cutoff function to ensure smooth transition to zero from inner cutoff ( $R - D$ ) to outer cutoff ( $R + D$ ), and is defined as

$$f_C(r) = \begin{cases} 1, & r < R - D \\ \frac{1}{2} - \frac{1}{2} \sin\left(\frac{\pi}{2} \frac{r-R}{D}\right), & R - D < r < R + D \\ 0, & r > R + D \end{cases} \quad (2.11)$$

$f_R(r)$  represents the repulsive part given as

$$f_R(r) = A \exp(-\lambda_1 r) \quad (2.12)$$

and  $f_A(r)$  represents the attractive part with the form

$$f_A(r) = -B \exp(-\lambda_2 r) \quad (2.13)$$

$b_{ij}$  is the bond-order term and has the form

$$b_{ij} = (1 + \beta^n \xi_{ij}^n)^{-\frac{1}{2n}} \quad (2.14)$$

where  $\xi_{ij}$  is

$$\xi_{ij} = \sum_{k \neq i, j} f_C(r_{ik}) g(\theta_{ijk}) \exp[\lambda_3^m (r_{ij} - r_{ik})^m] \quad (2.15)$$

$g(\theta)$  is given as

$$g(\theta) = \gamma_{ijk} \left( 1 + \frac{c^2}{d^2} - \frac{c^2}{[d^2 + (\cos \theta - \cos \theta_0)^2]} \right) \quad (2.16)$$

For the Tersoff potential, three sets of parameters are needed to describe the Mo-Mo, Mo-Se, and Se-Se pair interactions, respectively. The parameters for Mo-Mo are summarized in Table 2.3. We adjusted parameters  $R$  and  $D$  to remove the artificial stiffening due to the cutoff function for MoSe<sub>2</sub>. We note that the original parameters,  $R = 3.5\text{\AA}$ ,  $D = 0.3\text{\AA}$  should be used if one wants to simulate a pure Mo system. The allowable range for Mo-Se and Se-Se parameters in the optimization are summarized in Table 2.4. Following Chan et al. [37], the same set of three-body parameters ( $\gamma, \lambda_3, c, d, \cos \theta_0$ ) were used for Mo-Se-Se, Se-Mo-Mo, Mo-Mo-Se, and Se-Se-Mo interactions, where the first element is the center atom bonded to the other two atoms in the array. Similarly, three-body parameters of Mo-Mo-Mo were used for Mo-Se-Mo, and three-body parameters of Se-Se-Se were used for Se-Mo-Se.

#### 2.5.4. Molecular Dynamics (MD) Simulations

MD simulations were conducted with LAMMPS [38] (3Mar20, serial version for optimization and mpi version for simulating larger systems). To compare MD simulations with *ab initio* calculations, we used the same atomic systems for most objectives except for the lattice structures and cohesive energies, in which we enlarged the size of the system for better sampling. For energy landscapes (equation of states, bond dissociation, phase transition, and dissociation of Se clusters), single point calculations were performed on the equilibrated structures from *ab initio* calculations without energy minimization. For the remaining objectives, an energy minimization step was carried out on the input structures with the conjugate gradient algorithm (energy tolerance 0 eV, force tolerance  $10^{-10}$  eV  $\text{\AA}^{-1}$ ) before calculating the energies. For simulations with MD steps, a time step of 1 fs was used. Phonon dispersion calculations were performed with phonopy (2.4.1.post5) [39]. Thermal conductivity was calculated using the equilibrium Green-Kubo formalism [40, 41]. A monolayer MoSe<sub>2</sub> flake of 2.3 by 2.3 nm was first equilibrated with an NVT ensemble for 0.1 ns, followed by an NVE step of 1 ns during which the ensemble average of the auto-correlation of the heat flux was measured for calculating the thermal conductivity. We computed in-plane thermal conductivities as the average over conductivities along the armchair and zigzag direction. The thermal conductivity at a given temperature was further averaged over 6 replicas with different initial random velocities. Atomic visualizations were created with OVITO [42].

Table 2.3. Tersoff parameters for Mo-Mo pair interactions.  $R$  and  $D$  were modified to eliminate the artificial stiffening behavior observed in MoSe<sub>2</sub>

Parameter	Value
$m$	1
$\gamma$	0.00124572
$\lambda_3 (\text{\AA}^{-1})$	2.09348000
$c$	7.58380771
$d$	0.28598932
$\cos \theta_{0\text{Mo-Mo}}$	-0.18562373
$n$	1
$\beta$	1
$\lambda_2 (\text{\AA}^{-1})$	0.49188490
$B(\text{eV})$	13.49671513
$R(\text{\AA})$	3.54
$D(\text{\AA})$	1.14
$\lambda_1 (\text{\AA}^{-1})$	4.22401184
$A(\text{eV})$	24161.62003453

### 2.5.5. Setup of Multiobjective Optimizations

The population size was set to be 156 for the genetic algorithm optimizations following Deb and Jain [43]. Each optimization was conducted for 500 generations with which the optimization converged. We submitted 20 runs concurrently with different random seeds. We used a simulated binary crossover operator with a crossover probability of 1 and a crowding degree,  $\eta$  of 30. For mutation operations, we used polynomial mutation with a mutation probability of 1 and a  $\eta$  value of 20. We stored and output statistics of the entire population for every certain number of generations to monitor the optimization

Table 2.4. Allowable range for the parameters of the Tersoff potential during optimization

Parameter	Range or specified value
$m_{\text{Mo-Se}}, m_{\text{Se-Se}}$	1
$\gamma_{\text{Mo-Se}}, \gamma_{\text{Se-Se}}$	0 – 10
$\lambda_{3\text{Mo-Se}} (\text{\AA}^{-1})$	-0.1 – 0.1
$\lambda_{3\text{Se-Se}} (\text{\AA}^{-1})$	0
$c_{\text{Mo-Se}}, c_{\text{Se-Se}}$	0 – 10
$d_{\text{Mo-Se}}, d_{\text{Se-Se}}$	0 – 10
$\cos \theta_{0\text{Mo-Se}}, \cos \theta_{0\text{Se-Se}}$	-5 – 5
$n_{\text{Mo-Se}}$	0 – 2
$n_{\text{Se-Se}}$	1
$\beta_{\text{Mo-Se}}$	0 – 2
$\beta_{\text{Se-Se}}$	1
$\lambda_{2\text{Mo-Se}}, \lambda_{2\text{Se-Se}} (\text{\AA}^{-1})$	0 – 2
$B_{\text{Mo-Se}}, B_{\text{Se-Se}} (eV)$	0 – 1000
$R_{\text{Mo-Se}}, R_{\text{Se-Se}} (\text{\AA})$	2.82 – 3.8
$D_{\text{Mo-Se}}, D_{\text{Se-Se}} (\text{\AA})$	0 – 1
$\lambda_{1\text{Mo-Se}}, \lambda_{1\text{Se-Se}} (\text{\AA}^{-1})$	2 – 6
$A_{\text{Mo-Se}}, A_{\text{Se-Se}} (eV)$	1000 – 5000

progress. After all runs finished, we combined the optimized parameters from all runs for the subsequent screening process. The optimization environment was set up with Python (3.7.7) and the genetic algorithm optimization was based on the DEAP framework (1.3.0) [44]. Parameter initialization, genetic algorithm operations, and calculations of statistics were conducted with DEAP. When the evaluation for an individual was needed, the code initiated a LAMMPS calculation via a system-level call, and read

the output from LAMMPS log files. Parallel programming was enabled by SCOOP (0.7.1.1) [45] to offer accelerated performance on supercomputer clusters. The optimization time scaled with the complexity of the interatomic potentials and was in the range of several hours to several days.

### 2.5.6. Monte-Carlo Simulations

The Monte Carlo (MC) simulations were carried out in a canonical system (constant number of atoms, volume and temperature). The initial simulation system was configured to match our experimental observation. Since the exact edge configuration (for both the vacancy cluster and the free edge) is not discernable from our HRTEM images, we introduced variations in edge configurations according to those identified in monolayer MoS<sub>2</sub> [46]. A padding layer of pristine MoSe<sub>2</sub> was included at the top, bottom, and left of the system in Figure 2a to eliminate the boundary effects. In each MC step, each vacancy is attempted to swap with a corresponding atom(s), i.e., a Mo atom for Mo vacancy and Se<sub>2</sub> (above and below the Mo layer) for Se<sub>2</sub> divacancy, within a cutoff distance  $d_{max}$ . After the swap, the energy of the new system is evaluated by running a single point calculation using a Tersoff potential parameterized for the mechanical and thermal properties of monolayer MoSe<sub>2</sub> [47]. The probability for accepting or rejecting the swap attempt follows the Metropolis MC [41], namely,

$$p = \exp\left(-\frac{\Delta E}{k_b T}\right) (\text{for } \Delta E > 0) \quad (2.17)$$

$$p = 1 (\text{for } \Delta E \leq 0) \quad (2.18)$$

In equation 2.17 and 2.18,  $\Delta E$  is the change of the total energy (ignoring thermal vibration) after the swap attempt,  $k_b$  is the Boltzmann constant, and  $T$  is the temperature. For cases where  $\Delta E > 0$ , a random number  $\xi \in [0.0, 1.0)$  is generated and the attempt is accepted if  $\xi < p$ . With the above setting, the swap move satisfies the requirement of ergodicity and detailed balance. Throughout the simulation, the energy of the system, the success rate, and the configuration of the system were recorded periodically for

the subsequent analysis. The Large-Scale Atomic/Molecular Massively Parallel Simulator (LAMMPS) software package [38] was used for energy calculations.

The minimum energy pathway was computed by climbing image nudged elastic band method in LAMMPS [48, 49]. The system configuration is identical to that of the MC simulations. Fourteen replicas including the initial and final configurations were created for each individual hopping event in Figure 3a. The energy and force cutoff for the minimization were selected as 0.01 eV and 0.01 eV  $\text{\AA}^{-1}$ , respectively. The spring constant for the nudging force was set as 0.1 eV  $\text{\AA}^{-1}$ . The energy of the system was computed with the parameterized Tersoff potential. First-principle simulations were conducted with SIESTA [31] and the setup is documented in our earlier work [47].

### 2.5.7. Nudged Elastic Band Simulations

Climbing image nudged elastic band simulations were carried out with LAMMPS. Fourteen replicas including the initial and final configurations were used. The energy and force cutoff for energy minimization were selected to be 0.1 eV and 0.01 eV  $\text{\AA}^{-1}$ . The spring constant for the nudging force was set as 1 eV  $\text{\AA}^{-1}$ . The minimum energy path was found using the Tersoff potential and was adopted by *ab initio* simulations and other interatomic potentials.

## CHAPTER 3

# Multiobjective Parametrization for Large Deformation Pathways of 2D Materials

## 3.1. Introduction

Molecular dynamics (MD) simulation based on force fields is a powerful tool for studying the temporal behaviors of materials at submicron scales. With continual improvements in hardware and algorithms, MD simulations are becoming increasingly accurate and widely adopted in several frontier problems in materials science and biology [50]. While such advances have greatly expanded the capability of MD simulations in size, timescale and complexity, their predictive powers rely heavily on the accuracy of empirical interatomic potentials in approximating the electronic interactions between atoms. Given the rapid emergence of new two-dimensional (2D) materials [51, 52] that have demonstrated promising electrical, chemical, optical, thermal, and mechanical properties, an increasing demand for accurate interatomic potentials needs to be fulfilled to facilitate mechanistic understandings of their behaviors at scales representative of those used in applications.

Typically, interatomic potentials are formulated for a specific class of materials and are parameterized for a selected list of properties. Consequently, their accuracies on materials beyond the target class or for properties not included in the parametrization need further validation by more accurate methods, i.e., *ab initio* calculations. When those validations are conducted, in general they fail to achieve accurate predictions and re-parametrization or new formulations are necessary. For instance, a reactive many-body potential parameterized for molybdenum disulfide [53] was found to yield artificial stiffening at large strain, and an ad-hoc parameter-tuning was conducted to correct such behavior [22]. A more systematic interatomic potential parametrization would be indispensable in this case but becomes a complex and specialized task that requires strong domain expertise and in most cases deep chemical

intuition. One of the complexity of the parametrizing procedure is to reasonably capture non-equilibrium properties such as vacancy formation energies and uniaxial tension behaviors at the same time. Typical training data (structures, energies, and bond stiffness of atomic clusters or primitive cells [54–56]) are found insufficient to accurately reflect such properties [22, 57]. Furthermore, there is little guidance beyond chemical intuition for choosing more appropriate training data, thus posing potential limitations on the accuracy and efficiency of the parametrization. Another complication arises due to the fact that interatomic potentials are often parameterized for a finite number of target properties, and some multi-objective optimization schemes may inevitably rely on human interventions. Specifically, a common approach, the weighted sum method, converts the multi-objective problems into single-objective problems with user-defined, objective-specific weights [58–60]. However, the choice of a priori weights may bias the optimization [61], thus limiting a holistic evaluation of the performance of interatomic potentials on various properties. This motivated researchers to formulate other optimization approaches, e.g., the Pareto front approach [62, 63]. The last problem of the parametrization is to obtain a set of parameters for a chosen potential form. The selection of a potential form for a new material requires a vast domain knowledge of not only the physics of the material at hand but also the specific details of such a form. This limitation inevitably hinders the big-picture view of whether interatomic potentials can be parametrized to simulate the behaviors of some special class of materials, e.g., 2D materials, whose atomic structures and properties are distinct from bulk crystals. As a result, it prevents a direct comparison of performance between various potentials for the same material.

Despite several successful parametrizations over the last decade [37, 53, 58, 64–69], an in-depth evaluation of the suitability of existing interatomic potentials for the prediction of phase transition and fracture of 2D materials is still lacking. We propose a robust parametrization method built upon density functional theory (DFT) data sets (considered as ground-truth) and the evolutionary multi-objective optimization algorithm, NSGA-III [43]. Similar to other genetic algorithms, NSGA-III avoids the dependence on gradient computation, hence it can be applied to any functional form (potential). In addition, this algorithm enables a generation of more widely distributed points on the Pareto front in the criterion space, allowing a more thorough search for an optimum interval. As a result, this algorithm,

along with adoption of a machine-learning-inspired protocol, shows good transferability and performance and offer higher parametrization flexibility. The proposed method is applied to several interatomic potentials of increasing complexity, namely, Buckingham [70], Stillinger-Weber [55], and Tersoff [56] for the structural, mechanical, and thermal properties of monolayer 2D materials in both the equilibrium and non-equilibrium regimes. The reactive empirical bond order (REBO-TMDC) [53] potential is also considered for comparison. As a case study, we perform the parametrization of MoSe<sub>2</sub> and prioritize its mechanical behavior. We use the structure and stability of various surfaces, and thermal properties to examine the interatomic potentials' transferability. All of the parameterized potentials have better accuracy in non-equilibrium properties when compared with existing MoSe<sub>2</sub> potentials, highlighting the effectiveness of the proposed parametrization method. We further explore the parametrization flexibility of the selected interatomic potentials by conducting correlation and principal component analyses on their prediction errors, which reveals a positive correlation between the complexities of interatomic potentials, their flexibility, and their performances on MoSe<sub>2</sub>. Together, these results suggest a robust potential parametrization approach and a quantitative potential selection criterion, which may be generalized for a wide range of materials and materials properties beyond those explored in this study.

## 3.2. Parametrization Workflow

### 3.2.1. Selection of Materials and Interatomic Potentials

Among existing 2D materials, transition metal dichalcogenides (TMDC) are one group of materials described by MX<sub>2</sub>, where M is a transition metal (Mo, W, etc.) and X is from the oxygen family (S, Se, etc.). Most TMDCs in monolayer form are semiconducting with strong photoluminescence [8], thus making them promising candidates for applications such as transistors [71], photo-detectors [72], supercapacitor electrodes [73], and solar cells [74]. We set out to parameterize interatomic potentials for TMDCs with a focus on failure-related properties, which are critical to the stability and reliability of systems that require frequent mechanical deformation, e.g., flexible electronics. Specifically, we selected monolayer MoSe<sub>2</sub> and its stable phase 2H for which existing interatomic potentials, parameterized primarily for equilibrium properties (structures at equilibrium, phonon dispersion etc.) [64, 75], show major

deviations in comparison to DFT for non-equilibrium properties including surface stability and uniaxial stress-strain response. This implies necessities to expand the parametrization to the non-equilibrium regime, defined as states with large perturbations from the equilibrium positions or systems possessing point defects.

We selected interatomic potentials according to their applicability for TMDCs and ability to describe atomic chemical environments. To the best of our knowledge, existing parametrizations for TMDCs include Stillinger-Weber (SW) potentials for the mechanical and thermal properties of MoS<sub>2</sub> [58, 64, 66, 68], MoSe<sub>2</sub> [64, 76], and WSe<sub>2</sub> [76], a Tersoff potential for the thermal properties of WSe<sub>2</sub> [37], a ReaxFF potential for the mechanical and transitional behaviors of MoS<sub>2</sub> [65, 77], and a REBO-TMDC potential for the interfacial and mechanical properties of MoS<sub>2</sub> [22, 53]. Those interatomic potentials can be segmented into cluster potentials (SW), cluster functionals (Tersoff) and reactive cluster functionals (ReaxFF and REBO-TMDC) with increased levels of complexity and capabilities [78]. Specifically, from the simplest pair potentials (e.g. Lennard-Jones potentials), cluster potentials introduce many-body ( $> 2$ ) interactions, cluster functionals incorporate bond-order terms for coordination-dependent bond strength, and reactive cluster functionals enable simulation of atomic chemical reactions. Herein, we chose SW, Tersoff, REBO-TMDC, and also the Buckingham potential [70], a simple pair potential widely used for ionic crystals.

### 3.2.2. Parametrization Method

Parametrization of the selected interatomic potentials was performed in an iterative manner. Each iteration consists of three steps, referred to as training, screening, and evaluation (Fig 3.1). In the training step, the parameters of the interatomic potentials are optimized with the multi-objective genetic algorithm to minimize the errors for a selected group of properties in comparison to *ab initio* data. Next, the optimized parameters are screened for the remaining properties with a set of user-specified maximum percentage errors to identify promising candidates. Such a protocol is inspired by machine-learning methods, in which the full dataset is separated into training and validation sets to balance underfitting and overfitting [79]. The evaluation step, including correlation and principal component analyses, is

deployed to identify the correlation relationships between properties and redundancy in them. The information is used to (a) guide the selection of training and screening properties for the next iteration and (b) to quantify parametrization flexibilities of interatomic potentials.

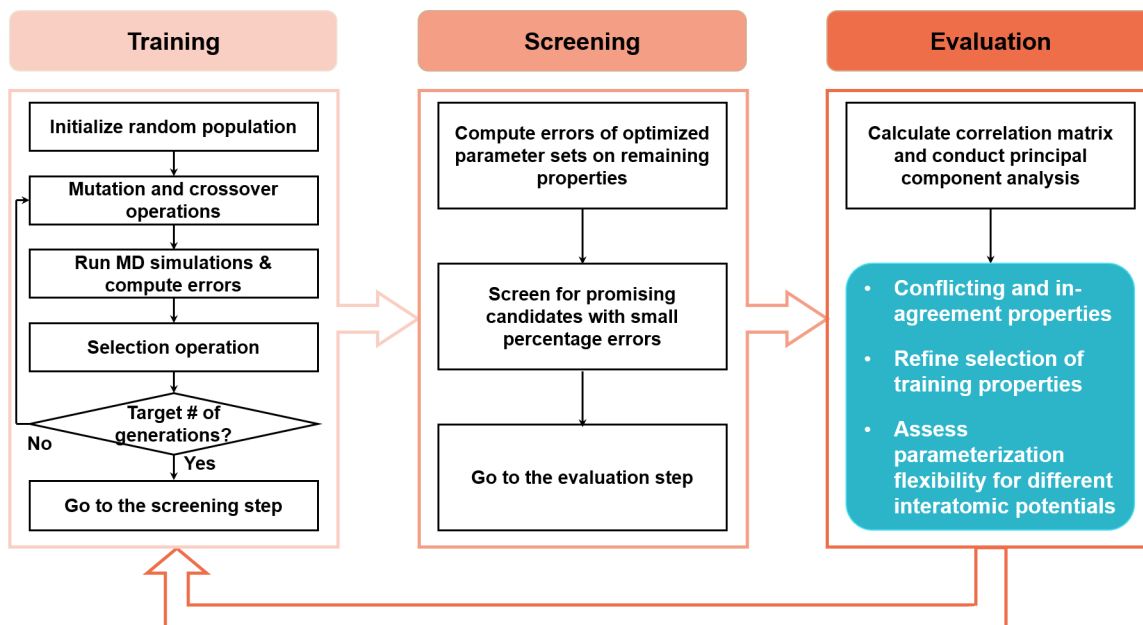


Figure 3.1. **Schematic of force field selection and parametrization approach.**

In the training step, the multi-objective genetic algorithm NSGA-III is used to optimize the parameters of the interatomic potentials for the training properties (Fig 3.2). MD simulations are integrated into the genetic algorithm workflow for the evaluation of errors. After reaching a predefined number of generations, the optimization terminates, and the optimized parameters are passed to the screening step for the evaluation of the screening properties (Fig 3.2). The training and screening properties together are considered for the selection of promising candidates with percentage errors for all properties within a user-specified threshold. Meanwhile, correlation and principal component analyses are carried out in the evaluation step to reveal the correlation relationships between properties and the performance of interatomic potentials. This information guides the selection of training properties for the next iteration of parametrization.

To predict the failure of MoSe<sub>2</sub>, we hypothesized that an essential list of materials properties (Fig 3.2), in both the equilibrium and non-equilibrium regime, needs to be captured by the interatomic potentials. In the equilibrium regime, we selected the lattice structure and cohesive energy of MoSe<sub>2</sub> at equilibrium, equation of state (near equilibrium), elastic constants ( $C_{11}$  and  $C_{12}$ ), surface energies (AC

and ZZ surfaces), and surface stability. For non-equilibrium properties, we selected the following: bond dissociation energy landscapes (along the armchair (AC) and zigzag (ZZ) directions), vacancy formation energies (7 types), and uniaxial stress-strain curves under elastic instability and soft mode (along the AC and ZZ directions, see Supplementary Note 1 for discussion on elastic instability and soft mode). Moreover, the energy landscape of a 2H-1T phase transition was included to characterize phase changes observed in TMDCs under uniaxial and biaxial strain [24], doping [80], or vacancy reorganization [77]. For the Tersoff and REBO-TMDC potential, an additional set of properties for Se systems is needed. Following Chan et al. [37], we selected the structures and cohesive energies of Se clusters ( $\text{Se}_2$ ,  $\text{Se}_3$ ,  $\text{Se}_6$ , and  $\text{Se}_8$ ), stability and dissociation of  $\text{Se}_6$  and  $\text{Se}_8$  and expanded the non-equilibrium regime by including the dissociation energy landscapes for  $\text{Se}_3$ ,  $\text{Se}_6$ , and  $\text{Se}_8$ . *Ab initio* calculations at the DFT level of theory were carried out on all the above properties, which were used as ground-truth for parameterizing the interatomic potentials.

The properties are divided into optimization and validation sets. The former is further segmented into training and screening sets, and the optimized parameters are then applied into the validation set after the optimization is finalized. Some training properties imply screening properties and vice versa, although they contain some inherently different information, e.g., the near-equilibrium data points of uniaxial stress-strain curves versus elastic constants, uniaxial stress-strain curves under elastic instability versus curves under soft mode. To explore uniaxial stress-strain response with *ab initio* simulations, a common approach is to apply homogeneous deformation on an infinite, defect-free crystal along the strained direction at zero temperature. The maximum strength acquired from such simulations is deemed the ideal strength of that material, and its magnitude is controlled by elastic instability. However, a finite-wave-vector phonon instability may occur at stress lower than the ideal strength, thus limiting the maximum stress a material can withstand. Such phonon instability, known as the soft mode, has been observed in two-dimensional (2D) materials including monolayer graphene, boron nitride, and  $\text{MoS}_2$  in *ab initio* simulations when symmetry breaking was introduced by random perturbation of ionic positions. Herein, we examined both the elastic instability and soft mode of monolayer  $\text{MoSe}_2$  under uniaxial tension along the armchair and zigzag directions. We applied homogeneous deformation on a pristine

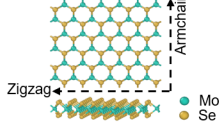
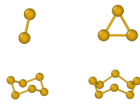
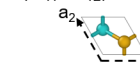
		MoSe <sub>2</sub>		Se (for Tersoff and REBO-TMDC potentials)	
		Equilibrium properties	Non-equilibrium properties	Equilibrium properties	Non-equilibrium properties
Training	<ul style="list-style-type: none"> <li>Lattice structure and cohesive energy</li> </ul>  <ul style="list-style-type: none"> <li>Equation of state</li> </ul>	<ul style="list-style-type: none"> <li>Bond dissociation energy landscape (along armchair and zigzag direction)</li> <li>Uniaxial stress-strain curves under elastic instability (armchair and zigzag)</li> </ul>	<ul style="list-style-type: none"> <li>Structures and cohesive energies of Se<sub>2</sub>, Se<sub>3</sub>, Se<sub>6</sub>, and Se<sub>8</sub> clusters</li> </ul> 	<ul style="list-style-type: none"> <li>Dissociation energy landscape of Se<sub>3</sub>, Se<sub>6</sub>, and Se<sub>8</sub></li> </ul>	
	Screening	<ul style="list-style-type: none"> <li>Elastic constants (C<sub>11</sub>, C<sub>12</sub>)</li> </ul>  <ul style="list-style-type: none"> <li>Surface energies (armchair and zigzag)</li> <li>Stability at 300K</li> </ul>	<ul style="list-style-type: none"> <li>Vacancy formation energies</li> <li>Uniaxial stress-strain curves under soft mode (armchair and zigzag)</li> <li>2H-1T phase transition energy landscape</li> </ul>	<ul style="list-style-type: none"> <li>Stability of Se<sub>6</sub> at 500K</li> <li>Stability of Se<sub>8</sub> at 393K</li> </ul>	<ul style="list-style-type: none"> <li>Dissociation of Se<sub>6</sub> at 4085K</li> <li>Dissociation of Se<sub>8</sub> at 2200K</li> </ul>

Figure 3.2. **Target properties of monolayer MoSe<sub>2</sub> and Se systems.** The properties are segmented with regard to their regime (equilibrium versus non-equilibrium) as well as their purposes for the parametrization (training versus screening). Properties of MoSe<sub>2</sub> are used for all interatomic potentials, while properties of Se are only used for parameterizing single-element interactions of the Tersoff and REBO-TMDC potentials. Atomic illustrations show the structure of MoSe<sub>2</sub> and Se clusters.

MoSe<sub>2</sub> crystal to measure its ideal strength, and introduced random perturbation (1% of the equilibrium Mo-Se bond length,  $\sim 0.025 \text{ \AA}$ ) prior to relaxation at each strain level to quantify the soft mode. As shown in Fig 3.3, soft mode (referred as perturbed) results in deterioration of failure strain and stress in both the armchair (AC, 17% decrease for strain and 3% decrease for stress) and zigzag directions (ZZ, 22% decrease for strain and 2% decrease for stress) in comparison to those under elastic instability (referred as homogeneous). We used the stress-strain curves under homogeneous deformation to train the interatomic potentials due to its lower variance, and screened the optimized potentials with stress-strain curves under perturbation. For MD simulations, we found that the perturbed uniaxial tension did not reveal the artificial phase transformations for the Buckingham and SW potential, which were identified instead by uniaxial tension tests at 1 K. Therefore, uniaxial tension tests at 1 K were conducted on the

selected interatomic potentials as a further examination for artifacts that are unable to be revealed by the perturbed uniaxial tension. In the absence of phase transformations, uniaxial tension at 1 K match closely with the perturbed uniaxial tension in MD simulations.

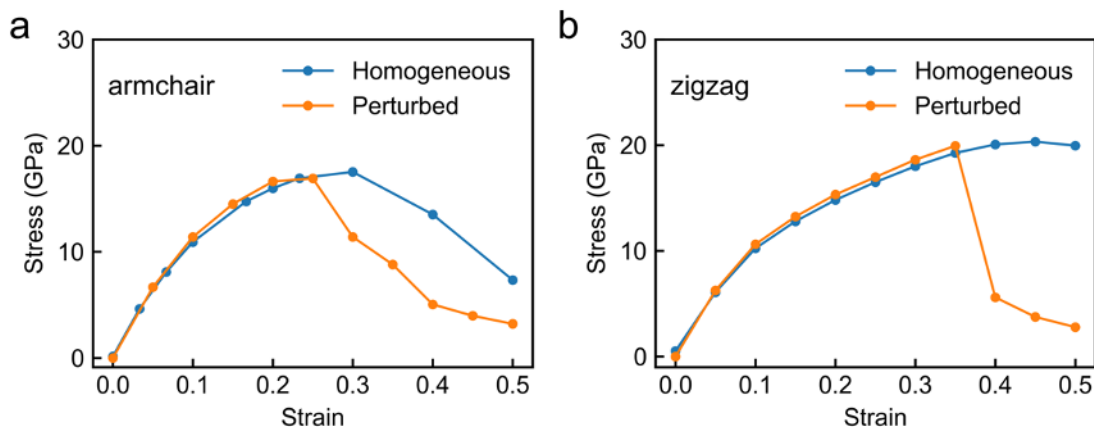


Figure 3.3. *Ab initio* uniaxial stress-strain curves along the armchair (a) and zigzag (b) directions for monolayer MoSe<sub>2</sub>, obtained with homogeneous deformation (labeled homogeneous) and with perturbation (labeled perturbed) of ionic positions. Elastic instability governs failure under homogeneous deformation, whereas soft mode controls the failure of the perturbed system. The soft mode causes decrease of failure strain and stress along both the armchair and zigzag directions.

We started an optimizing process by selecting simple properties for training, such as bond dissociation energy landscapes, and more complex properties, e.g., vacancy formation energies, as screening properties [65, 66]. Another factor that affected this choice is the size and type of calculation needed to be carried out for a given property. For example, a fixed-point energy calculation would be favored over one that requires molecular dynamics equilibration, and a system of primitive unit cell will be prioritized unless a larger system with more atoms would provide more representative data. This criterion accelerates the optimization since the simpler properties often require single-point calculations that are faster to perform than those that require energy minimization or extra molecular dynamics steps. These extra steps occasionally suffered from convergence issues due to emergence of unphysical interatomic potential parameters at the first several steps of optimization. Moreover, properties of the same general attribute,

i.e., uniaxial stress-strain curves, were used in both stages with different levels of perturbation. Specifically, stress-strain curves under elastic instability were used as training properties and the curves under soft mode were used as screening properties. As such, we selected the following properties as training properties: lattice structure and cohesive energy at equilibrium, equation of state, bond dissociation energy landscapes along both the AC and ZZ directions, and uniaxial stress-strain curves under elastic instability along both the AC and ZZ directions. We note that such a choice is not fixed. Rather, its effect on the parametrization results can be determined from the correlation analysis, as discussed later.

Our training step involves solving a multi-objective optimization problem for which two major approaches prevail: scalarization and vector optimization methods [61]. Scalarization methods convert multi-objective optimization problems into single-objective optimization problems using methods such as weighted-sum, and are predominantly used for parameterizing interatomic potentials. On the other hand, vector optimization methods treat each objective independently and aim at exploring the Pareto optimal solutions? solutions that cannot be further improved without worsening at least one objective. These methods assign equal importance to each objective and allow users to emphasize or exclude certain objectives without biasing the optimization. This is helpful in preventing solutions from being swamped out, but may be a limitation if relative importance between objectives is known. We overcame this limitation in the screening step by assigning a lower objective-specific percentage error (discussed later) if one wants to focus on a specific property. Among various vector optimization methods, we adopted a multi-objective genetic algorithm named NSGA-III [43]. As a genetic algorithm, it conducts a global optimization through an iterative process that loosely mimics Darwin’s theory of natural selection, i.e., via mutation, crossover, and selection operations on a population of individuals. Moreover, the algorithm incorporates a nondominated sorting procedure and a niche-preservation operator to identify nondominated individuals that are well-spread in the criterion space. As a result, this specific algorithm shows superiority by sampling more widely-distributed points on the Pareto front. To the best of our knowledge, we report the first application of NSGA-III for parameterizing interatomic potentials. In most optimization problems with 3-10 objectives, it outperforms its predecessor, NSGA-II [81], which has been

the predominant algorithm applied in similar problems [62, 63]. Moreover, we found that it is more efficient in overcoming local minimum states during the optimization in comparison to a hierarchical genetic algorithm optimization framework [37].

As shown in Fig 3.1, the optimization starts from an initial population of individuals (i.e., sets of parameters for a given interatomic potential) that are randomly generated within a predefined range according to potential-specific requirements. In each generation, mutation and crossover operations are first conducted on the current population according to specified probabilities. The parameters after mutation and crossover are not allowed to exceed the predefined initialization range. The value to be minimized for each objective during the optimization, i.e., the fitness value, is defined as follows:

$$f_i(x) = \sum_{j=1}^K w^j (v_i^j(x) - \hat{v}_i^j)^2; i = 1, \dots, M_t \quad (3.1)$$

where  $x$  represents an individual whose dimension equals the number of parameters to be optimized for a given interatomic potential,  $v_i(x)$  denotes predictions from interatomic potentials with parameter set  $x$  for objective  $i$ ,  $\hat{v}_i$  represents *ab initio* results for objective  $i$ , superscript  $j$  represents the  $j^{th}$  point for objective  $i$ , and  $w^j$  is the corresponding weight for the  $j^{th}$  point. The weight is used to emphasize certain regions of the training data, e.g., elastic regime of the stress-strain curves. The values of the weights are provided in Table 3.1, and are found to have an insignificant effect on parametrization results. The point-wise errors are squared, scaled, and summed over all the  $K$  points for objective  $i$ . Thus, the fitness value is the squared error for objectives with  $K = 1$  (e.g., elastic constant  $C_{11}$  etc.), and is the sum of (weighted) squared errors for objectives with  $K > 1$  (e.g., stress-strain curves). For each parameter set  $x$ , there are  $M_t$  fitness values corresponding to the  $M_t$  training objectives (properties). Individuals of the current generation are ranked based on whether they are dominated by other individuals. An individual  $x$  is nondominated if and only if there does not exist another individual  $x^*$  in the current population such that  $f_i(x^*) \leq f_i(x)$  for any  $i$  with at least one  $f_i(x^*) < f_i(x)$ . All nondominated individuals (Pareto optimal solutions) are ranked lowest and are selected first, followed by individuals that are only dominated by those Pareto optimal solutions and so on. The selected individuals are passed to the next generation

where the same protocol repeats until the predefined total number of generations is reached. For each interatomic potential, multiple optimizations are carried out concurrently with different random seeds to explore a large parameter space and various optimization paths.

Table 3.1. Weights for bond dissociation energy landscapes and uniaxial tension

Point on the curve	Bond dissociation energy landscape armchair	Bond dissociation energy landscape zigzag	Uniaxial tension (homogeneous and perturbed) armchair and zigzag
2 <sup>nd</sup>	4096	4096	64
3 <sup>rd</sup>	1024	1024	16
4 <sup>th</sup>	256	256	4
5 <sup>th</sup>	64	64	1
6 <sup>th</sup>	16	16	1
7 <sup>th</sup>	1	4	1
8 <sup>th</sup>	1	4	1
Rest	1	1	1

Prior to the screening step, the optimized individuals from multiple optimizations are gathered, and the fitness values for the remaining properties (screening properties in Fig 3.2) are calculated following equation 3.1. Those values are combined with the fitness values of the training properties to form a matrix of dimension  $N \times M$ , where  $N$  is the total number of optimized individuals and  $M$  is the total number of properties. This matrix is then screened with the criterion defined as follows:

$$f_i(x) \leq \sum_{j=1}^K w^j (p_i \hat{v}_i^j)^2; i = 1, \dots, M_t \quad (3.2)$$

where  $f_i(x)$ ,  $w^j$ , and  $\hat{v}_i^j$  follow the same definitions as in equation 3.1, and  $p_i$  is an objective-specific percentage value. The criterion defines a maximum percentage error for objectives with one data point ( $K = 1$ ), and resembles the sum of squared percentage error (SSPE) for objectives with multiple data points. Indeed, this criterion and the SSPE measurement agree well in magnitude and variation according to a sampling test on a harmonic function. The parameters  $p_i$  reflect the relative importance

of each objective and provide a desirable level of flexibility for the parametrization without biasing the optimization, which is a major advantage over the prevalent weighted-sum method. The parameter sets that pass the screening step are deemed promising candidates.

Our approach is unique in several respects. In our implementation of screening sets, we used explicit criteria for selecting fittest interatomic potential parameters and evaluating the parametrization flexibility. This emerges when we evaluate the effect of one criterion on the validation properties or the entire set of properties. This approach is different to most, if not all, parametrization of empirical interatomic potentials in which the validation sets are used for examining the presumptive transferability instead of guiding the optimization. For instance, validation test for a recently developed CHARMM force field [82] is conducted on chemically similar species with respect to the optimization sets. Such a validation should and indeed does reveal good transferability as it follows the underlying assumptions of the CHARMM General Force Field [83]. By contrast, several interatomic potentials for MoSe<sub>2</sub>, as reported in the literature, have poor transferability (see the next section). In the present approach, the improvement on transferability can be done by re-defining allowable errors for the screening sets (and training sets) that have more impact on a desired validation property (e.g., phonon dispersion and thermal conductivity). Thanks to this protocol, we were able to ascertain transferability and infer directions for balancing parametrization tradeoffs of specific properties. Lastly, we introduced correlation and principal component statistical analyses to ascertain correlation relationship between properties and infer parametrization flexibilities of interatomic potentials, both of which remain unexplored in the literature. We note that the statistical information closes the parametrization loop by guiding the selection of training and screening properties for the next iteration, as further elaborated in subsequent sections.

### 3.3. Parametrization Results

Table 3.2 and Fig 3.4 summarize the predictions of the parameterized interatomic potentials in comparison to *ab initio* calculations as well as existing SW [64] and SNAP [75] potentials for monolayer MoSe<sub>2</sub>. In selecting the parameter sets for each interatomic potential with equation 3.2, we emphasize the accuracy of uniaxial stress-strain curves (under soft mode) while maintaining other properties to be

at least within 90% error. The parameterized potentials are listed in Table 3.3, 3.4, 3.5. Not surprisingly, since the SW potential parameterized by Kandemir et al. and the SNAP potential parameterized by Gu and Zhao are primarily trained for equilibrium properties including structures and thermal transport, they show limited accuracy for the non-equilibrium properties studied herein: vacancy formation energies (Table 3.2) deviate from *ab initio* results (the surface and vacancies structures cannot be equilibrated with the SNAP potential); bond dissociation energy landscapes along the armchair (Fig. 3.4(a)) and zigzag (Fig. 3.4(b)) directions deviate from *ab initio* curves at strain  $> 0.1$ ; uniaxial stress-strain curves along both the armchair (Fig. 3.4(e)) and zigzag (Fig. 3.4(f)) directions deviate significantly from *ab initio* results at strains larger than 0.05. In comparison, the parameterized interatomic potentials here reported yield predictions that are vastly more accurate for those properties due to the augmented *ab initio* training data in the non-equilibrium regime and an explicit screening step that further defines maximum allowable errors.

Fig. 3.4(d) shows the phase transition energy landscape identified by climbing image nudged elastic band simulations [49]. Under the screening criteria, which prioritize stress-strain responses, all the parameterized interatomic potentials incorrectly predict the 1T phase to be the minimum energy state. For the Tersoff potential, an individual with the correct relative energy between the 2H and 1T phase have less accuracy on other properties. The results suggest an important limitation of the Tersoff potential, which is the capturing of the phase transition energy landscape. This finding is confirmed by the correlation analysis discussed in the next section.

Notably, the Tersoff potential has the overall best performance among the selected interatomic potentials. It provides a smooth uniaxial tension curve closely matching the *ab initio* results, whereas the Buckingham and SW potentials predict an artificial 2H-1T phase transition during uniaxial tension at  $\sim 0.2$  strain, manifested as kinks in Fig. 3e and 3f. This data seems to advocate a positive correlation between the complexity of the interatomic potential and its overall accuracy for monolayer MoSe<sub>2</sub>. Such observation is further corroborated by the correlation analysis, as described in the next section. We note the importance of direct force fitting (i.e., stress-strain curves as training data) for the Tersoff potential to achieve good accuracy for uniaxial tension response. Similarly, forces and other higher order derivatives

Table 3.2. Comparison of the parameterized interatomic potentials with *ab initio* results. Two existing SW [64] and SNAP [75] potentials for monolayer MoSe<sub>2</sub> are also included. The comparison includes predictions of cohesive energy per atom,  $E_{coh}$ , equilibrium distance between Mo-Se and Se-Se atoms (Se atoms above and below the Mo layer), Elastic constants  $C_{11}$  and  $C_{12}$ , armchair and zigzag surface energies  $\Gamma_{AC}$  and  $\Gamma_{ZZ}$ , vacancy formation energies of Mo monovacancy  $E_{Mo}$ , non-adjacent Mo divacancies  $E_{Mo2F}$ , adjacent Mo divacancies  $E_{Mo2C}$ , Se monovacancy  $E_{Se}$ , Se divacancies (one above and one below the Mo layer)  $E_{Se2}$ , one Mo and three adjacent Se vacancies (in the same Se atomic layer)  $E_{MoSe3}$ , one Mo and six adjacent Se vacancies  $E_{MoSe6}$ , and root mean square displacements (RMSD) at 300K.

	<i>Ab initio</i>	Buckingham	SW	Tersoff	SW ([64])	SNAP ([75])
$E_{coh}(eV)$	-4.77	-3.33	-4.35	-5.10	-4.59	-2.11
$d_{Mo-Se}(\text{\AA})$	2.57	2.47	2.48	2.52	2.54	2.53
$d_{Se-Se}(\text{\AA})$	3.39	3.08	3.10	3.25	3.29	3.26
$C_{11}(GPa)$	129.34	145.66	124.59	129.29	149.96	138.52
$C_{12}(GPa)$	35.36	62.82	13.66	22.78	57.28	28.77
$\Gamma_{AC}(eV\text{\AA}^{-1})$	0.72	0.67	0.43	0.39	1.17	- <sup>a</sup>
$\Gamma_{ZZ}(eV\text{\AA}^{-1})$	0.77	0.74	0.64	0.42	1.35	-
$E_{Mo}(eV)$	6.51	2.85	7.25	5.59	0.60	-
$E_{Mo2F}(eV)$	11.69	5.70	14.53	10.61	1.20	-
$E_{Mo2C}(eV)$	10.44	5.39	14.10	10.55	0.17	-
$E_{Se}(eV)$	3.30	0.62	0.57	2.14	6.93	4.12
$E_{Se2}(eV)$	6.23	3.92	4.20	3.98	12.52	7.24
$E_{MoSe3}(eV)$	10.94	1.66	4.76	8.51	16.70	-
$E_{MoSe6}(eV)$	20.27	6.64	8.78	10.79	15.71	-
$RMSD\ at\ 300K(\text{\AA})$	-	0.25	20.25	0.24	0.15	0.25

<sup>a</sup>A dash denotes that the system with surface or vacancy undergoes significant structural changes and cannot be equilibrated with the SNAP potential.

Table 3.3. Parameters of the parameterized Buckingham potential

Parameter	Mo-Mo	Mo-Se	Se-Se
$A(\text{eV})$	7769.92513956653	9999.913147274501	9158.327129108897
$\rho(\text{\AA}^{-1})$	0.3360228666896364	0.29381112441007645	0.34885094326951654
$C(\text{eV}\text{\AA}^6)$	885.1380397237746	757.7432414900966	982.5327519248219
$\alpha$		0.0003869226688613496	
$r_{c1}(\text{\AA})$		7.898268379510417	
$r_{c2}(\text{\AA})$		7.614831519220617	

Table 3.4. Parameters of the parameterized SW potential

Parameter	Mo-Mo	Mo-Se	Se-Se
$A$	2.259232273571551	6.247957225470649	5.343292506286849
$B$	8.641668798543233	0.8733167409570036	27.359820357976744
$p$	5	5	5
$q$	0	0	0
$\lambda$	0	29.89203647110673	0
$\cos \theta_0$	0	-0.05780305292041443	0
$\gamma$	0	1.0717245267372222	0
$\epsilon(\text{eV})$	1	1	1
$a$	2.681498446550725	2.597953051732073	1.288404529185639
$\sigma(\text{\AA})$	1.7034707795667612	1.6736021541354618	1.2325538692543965

of energies were found critical for accurate predictions of phonon dispersion and thermal transport in

Table 3.5. Parameters of the parameterized Tersoff potential

Parameter	Mo-Se	Se-Se
$m$	1	1
$\gamma$	5.856469817727996	0.5390371171619912
$\lambda_3 (\text{\AA}^{-1})$	-0.02513872152647509	0
$c$	9.939998602046574	0.6332501766924936
$d$	1.5471400012091288	0.39414466839749035
$\cos \theta_0$	0.1405125795968635	-0.12220908199078442
$n$	1.1360891123038677	1
$\lambda_2 (\text{\AA}^{-1})$	0.042907028325992976	1
$B(\text{eV})$	0.9103950359257892	0.92204739497169
$R(\text{\AA})$	55.529371568547575	49.7256794118459
$D(\text{\AA})$	3.16	3.0335105029282676
$\lambda_1 (\text{\AA}^{-1})$	0	0.9884234177305641
$A(\text{eV})$	3.2079053037522387	3.505593811315402

crystalline Si and Ge [59]. Thus, inclusion of force fitting during parametrization should result in better transferability of the interatomic potentials.

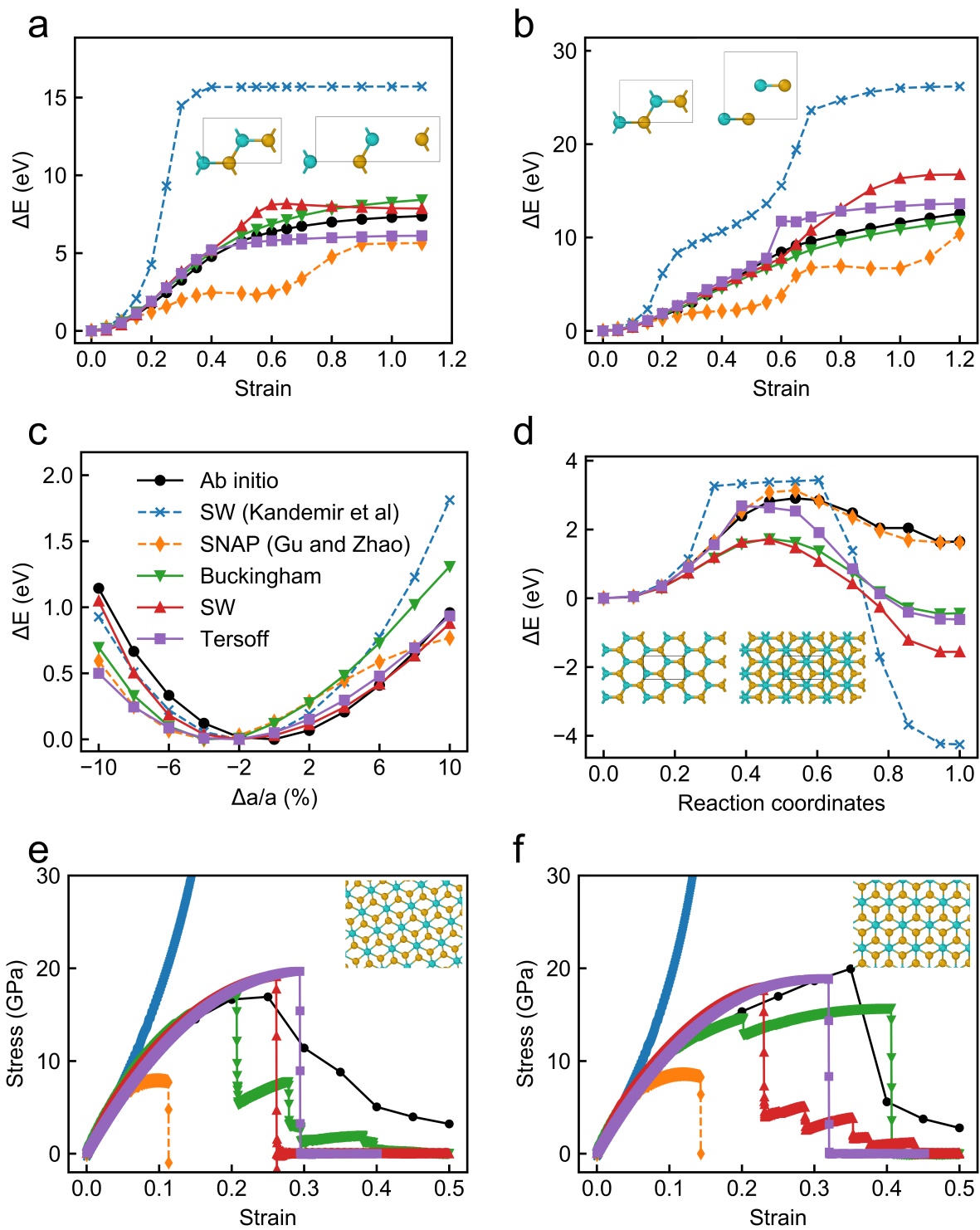


Figure 3.4. **Prediction results of the parameterized interatomic potentials in comparison to *ab initio* results as well as existing SW [64] and SNAP [75] potentials.** (a-b) Bond dissociation energy landscape along the armchair (a) and zigzag (b) directions. Two snapshots along the landscape are shown and correspond to strain of 0 and 0.6, respectively. (c) Equation of state. (d) 2H-1T phase transition energy landscape. The two snapshots from left to right correspond to reaction coordinates of 0 and 1, respectively (see Supplementary Video 1 for the movie of this simulation). (e-f) Uniaxial stress-strain curve at 1 K in comparison to *ab initio* curves under soft mode (see Supplementary Note 1) along the armchair (e) and zigzag (f) directions. The snapshots in (e) and (f) show the formation of the 1T phase during uniaxial tension for the Buckingham potential, which is also predicted by the SW potential during uniaxial tension along the zigzag direction. Legends of (a-b, d-f) are identical to that in (c), and are omitted for clarity. In the atom snapshots, Mo atoms are colored cyan, and Se atoms are colored orange.

### 3.4. Correlation and Principal Component Analyses

As part of the screening step, a matrix of dimension  $N \times M$  is constructed where each of the  $N$  rows contains the fitness values, equation 3.1, of all the  $M$  properties. Treating each row as a sample point in the  $M$ -dimensional design space enables a quantitative assessment of the relations between the  $M$  properties through statistical analysis. From the  $N \times M$  matrix, we construct an  $M \times M$  correlation matrix where each element  $R_{ij}$  is the Pearson correlation coefficient between property  $i$  and property  $j$ . A graphical representation of those coefficients for the Tersoff potential is shown in Fig 3.5. The correlation coefficients in Fig 3.5 correspond to individuals with percentage errors  $< 100\%$  for all properties. Such setting aims at exploring regions in the criterion space where promising candidates are selected.  $R_{ij}$  ranges from -1 to 1, denoting strongly negative and positive correlations, respectively. In the context of our problem, a positive  $R_{ij}$  between property  $i$  and  $j$  indicates simultaneous increase or decrease of their prediction errors and hence non-conflicting relations between the two properties. In comparison, a negative  $R_{ij}$  suggests a conflicting relationship between property  $i$  and  $j$ : the errors for property  $i$  cannot be minimized without compromising the accuracy of property  $j$ .

As shown in Fig 3.5, the Tersoff potential (the bottom triangle) possesses several pairs of properties that are strongly positively correlated. Conforming to chemical intuition, properties of similar nature have strong positive correlations, e.g., bond dissociation energies along the armchair and zigzag directions ( $R = 0.7$ ), armchair and zigzag surface energies ( $R = 0.9$ ), and vacancy formation energies of Mo and  $\text{Mo}_2\text{F}$  ( $R$

= 1). Similar relations were identified for the Buckingham and SW potential (see Fig. 3.6 and Fig. 3.7). The correlation matrix also reveals conflicting properties that cannot be directly deduced from chemical intuition. Specifically, the phase transition energy landscape is conflicting to almost all properties. This agrees with our observation of accuracy degradation of most properties when the phase transition energy landscape is prioritized. Thus, the correlation matrix offers a direct gauge of the accuracy (and hence the parameters) of the parameterized interatomic potential on all properties should the relative importance between properties be different.

To assess the parametrization flexibility of any interatomic potential, we propose evaluating a quantity  $F$  defined as

$$F = \frac{\sum_{j < i} R_{ij}}{M}; i, j = 1, \dots, M \quad (3.3)$$

For an ideal interatomic potential approaching an *ab initio*-level of accuracy, there should exist a region in the criterion space where the prediction errors of all properties have strong positive correlations and thus can be minimized simultaneously, which allows a large level of flexibility for parametrization. For the ideal interatomic potential,  $F_{ideal} = (M - 1)/2$ . We sampled five regions in the criterion space near 100% percentage errors ( $p_i = 80\%-120\%$ ) with enough individuals ( $> 30$ ) in each region.  $F_{Tersoff}$ ,  $F_{SW}$ , and  $F_{Buckingham}$  were found to be  $1.44 \pm 0.12$ ,  $0.71 \pm 0.25$ , and  $0.77 \pm 0.12$ , respectively. Notably, the Tersoff potential has the highest flexibility, consistent with our observation that the parameterized Tersoff potential predicts the most accurate uniaxial stress-strain curves.

To further explore the intrinsic relationships between properties, we conducted principal component analysis on the correlation matrix. It was originally proposed to identify redundant objectives during multi-objective optimizations [84], and is used herein to find redundant properties, i.e., properties that can be automatically captured if essential properties are captured with either the training or screening step. The analysis reveals that all the training data are non-redundant for all the interatomic potentials, thus indicating optimized training properties. Furthermore, it shows that the formation energies of certain vacancies are redundant with respect to others, in agreement with chemical intuition.

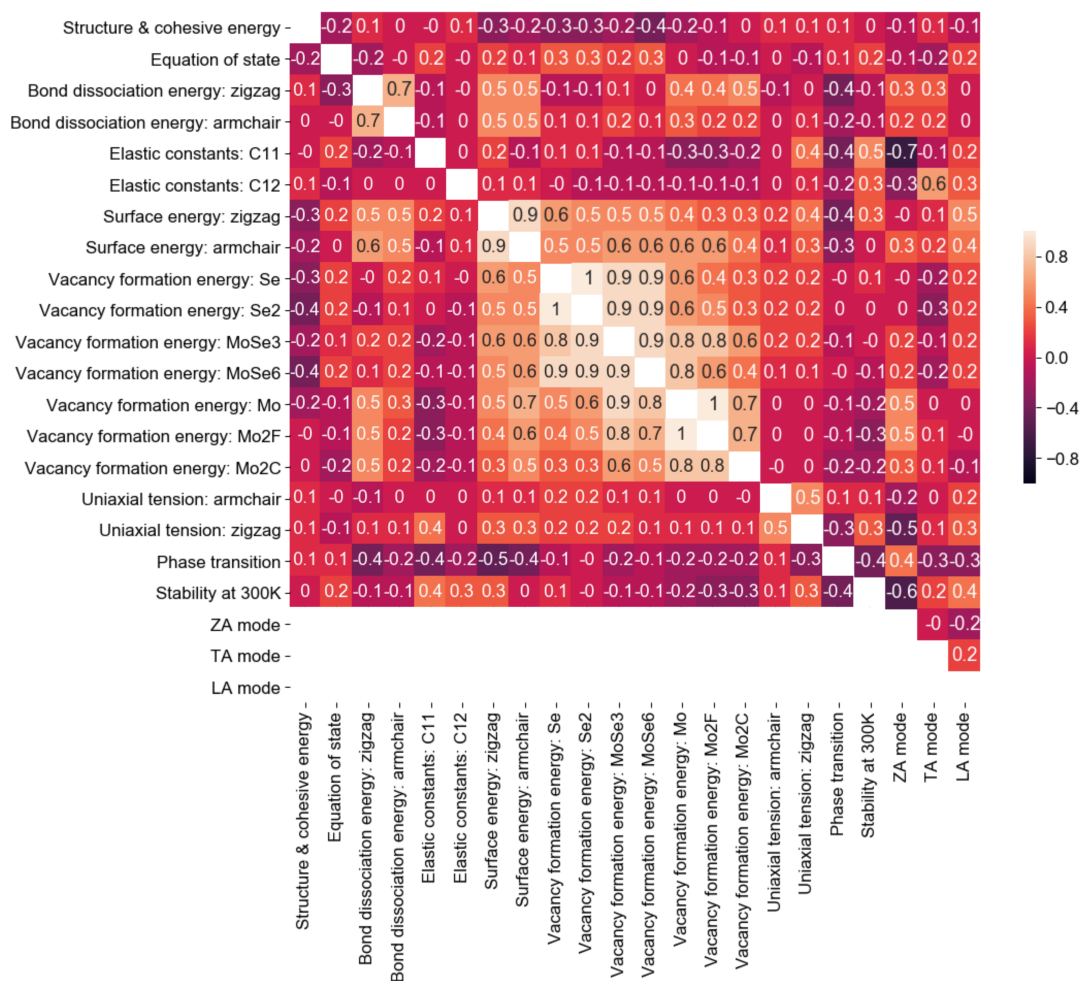


Figure 3.5. **Correlation matrix of the Tersoff potential.** The Pearson correlation coefficient for the corresponding pair of properties, ranging from -1 to 1, is shown in each cell. When calculating the correlation coefficients, individuals with percentage errors  $> 100\%$  for any property were excluded to explore the region in the criterion space where promising candidates are selected. Two correlation matrices are shown; the bottom corresponds to the as-optimized Tersoff potential and the top corresponds to the same population with additional screening on the three acoustic phonon modes, ZA, LA, and TA. Since each correlation matrix is symmetric, only half of the correlation matrix is shown and the diagonal components (always equal to 1) are removed for clarity. For visualization purpose, all correlation coefficients are rounded to a decimal. Thus, a value of "-0" means the true correlation coefficient is within  $[-0.05, 0)$ . The cells are colored according to their correlation coefficients. Uniaxial tension items herein refer to curves under soft mode.

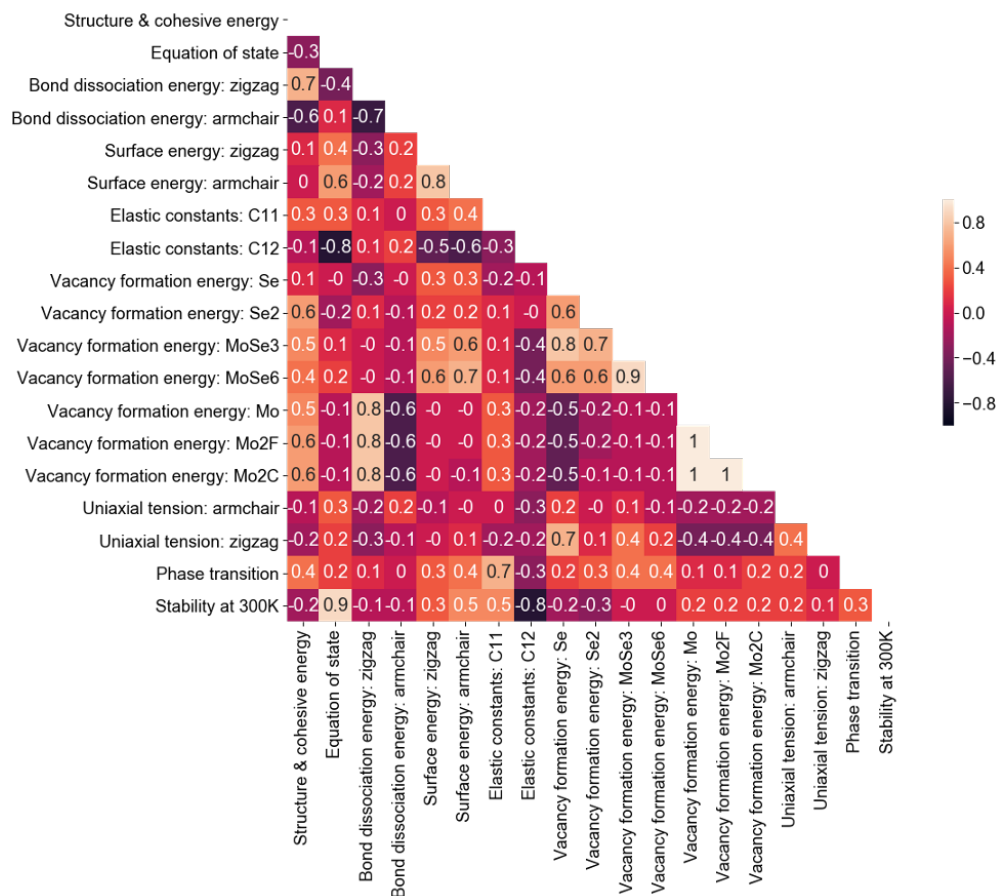


Figure 3.6. Correlation matrix for the Buckingham potential.

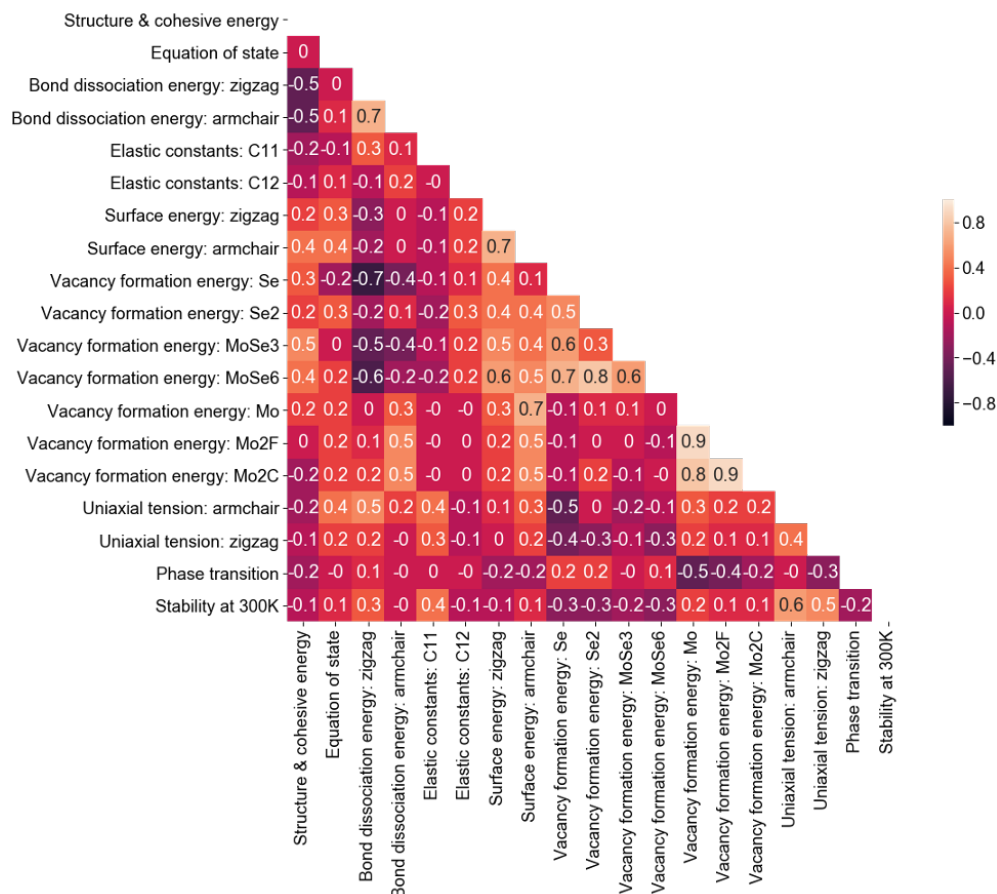


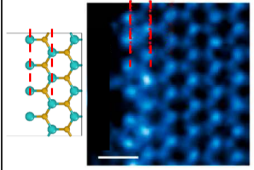
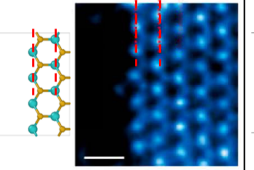
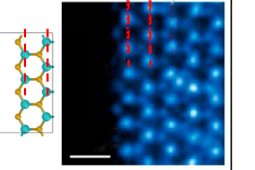
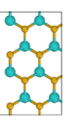
Figure 3.7. Correlation matrix for the SW potential.

### 3.5. Examination on Transferability

We evaluated the validity and transferability of the optimized Tersoff potential on the edge stability and thermal properties of monolayer  $\text{MoSe}_2$ , which are relevant for applications in nanoelectronics [64, 75] and catalysis [46], but are not parameterized within the scope of this study. This can also be referred as the "test" data set in other machine learning frameworks [79]. Fig. 3.8 shows *ab initio* molecular dynamics (AIMD) and Tersoff predictions on the stability of various edge configurations at 300 K and elevated temperatures. Those configurations correspond to the Mo-Klein, Mo-zigzag, Se-zigzag, and the armchair edge, which were identified by scanning transmission electron microscopy (Fig 3.8) in nanoporous  $\text{MoS}_2$  films grown with molecular beam epitaxy under high Mo flux [46]. The Tersoff potential shows a

decent level of transferability owing to its higher flexibility in its functional form: it reproduces AIMD predictions for all the edges at 300 K, for the Mo-Klein and Se-zigzag edges at elevated temperatures (650 K and 750 K, respectively), but tends to overstabilize the Mo-zigzag edges at 650 K. Fig. 3.9(a) shows the phonon dispersions predicted by the parameterized Tersoff potential in comparison to *ab initio* results. The Tersoff potential predicts no negative frequency and correct  $\Gamma$  point for acoustic bands albeit lower frequencies for the out-of-plane (ZA) mode and smaller phonon band gap. Such inconsistency results in lower in-plane thermal conductivity in comparison to first-principles calculations [85] and experimental measurements on a suspended monolayer MoSe<sub>2</sub> membrane [86] as shown in Fig. 3.9(b). However, we note that the excellent accuracy of the longitudinal (LA) and in-plane transversal acoustic band (TA) was captured by Tersoff potential due to the inclusion of force fitting in training, i.e., uniaxial stress strain curve along two directions.

We next discuss how the correlation and principal component analyses are employed to close the parametrization loop and improve the accuracy of phonon dispersion. We screened the optimized Tersoff population on the three acoustic phonon modes, and conducted a correlation analysis. The correlation matrix (Fig. 3.5, top triangle) shows that the ZA mode is more conflicting to other properties in comparison to the TA and LA mode, i.e., for C11, uniaxial stress-strain curves along the zigzag direction, and stability at 300 K. Such results suggest that adding the ZA mode into the training data will increase the accuracy of ZA mode at the expense of decreased accuracy on the aforementioned properties. However, the worsening effect may be mitigated by including the other two modes that possess relatively positive correlation relationships. We carried out two iterations, one with the addition of ZA mode and the other with the addition of all three modes to the training data set. The results support the above statement. Specifically, the iteration with all three modes, referred as Tersoff-ZTL, resulted in a more accurate ZA mode (Fig. 3.9(a)) and thermal conductivity (Fig. 3.9(b)) with minimum deterioration of other properties. We note that the bending rigidity of 2D materials is directly related to the ZA mode [87]. Thus, the Tersoff-ZTL should possess improved accuracy on bending rigidity.

Edge type	Mo-Klein		Mo-zigzag		Se-zigzag		Armchair
Atomic configuration							
Temperature	300 K	650 K	300 K	650 K	300 K	750 K	300K
AIMD	stable	unstable	stable	unstable	stable	stable	unstable
Tersoff	stable	unstable	stable	unstable	stable	stable	unstable
Tersoff-ZTL	stable	unstable	stable	unstable	stable	stable	stable

stable
  unstable

Figure 3.8. **Transferability test for the parametrized potentials (Tersoff and Tersoff-ZTL) on edge stability of monolayer MoSe<sub>2</sub>.** The edges were observed in nanoporous MoS<sub>2</sub> films grown with molecular beam epitaxy under high Mo flux [46]. Scanning transmission electron microscopy images of the corresponding edge structures for MoS<sub>2</sub> were retrieved from Zhao et al. [46] and are shown herein. Red dashed lines highlight the Mo atomic layers, and the scale bars represent 0.5 nm. The same edge configuration was equilibrated with *ab initio* MD (AIMD) (for 1 ps) and MD (500 ps) at the specified temperature. An "unstable" configuration is defined as a configuration that undergoes breakage and re-formation of chemical bonds during equilibration. We note a longer simulation time for MD to reveal the unstable edge configurations due to limitations of interatomic potentials to reflect electronic interactions embedded in the AIMD simulations. In the atomic snapshots, Mo atoms are colored cyan, and Se atoms are colored orange. The Tersoff-ZTL corresponds to the parameterized potential with the training data of 'Tersoff' plus the three acoustic phonon modes, i.e., ZA, LA, and TA. Reprinted (adapted) with permission from Zhao et al. [46] Copyright (2018) American Chemical Society.

### 3.6. Chapter Summary

We propose a robust approach of parameterizing interatomic potentials. It incorporates the multi-objective genetic algorithm NSGA-III, a machine-learning-inspired protocol, and a correlation and principal component analyses framework. Using monolayer MoSe<sub>2</sub> as a testbed, we demonstrate the effectiveness of the proposed approach in capturing properties of monolayer MoSe<sub>2</sub> in both the equilibrium and non-equilibrium regime. Compared with existing parametrization methods, our approach incorporates a more efficient optimization algorithm, provides more flexibility for balancing the tradeoff and priority of specific properties without biasing the optimization, and shows good transferability for various

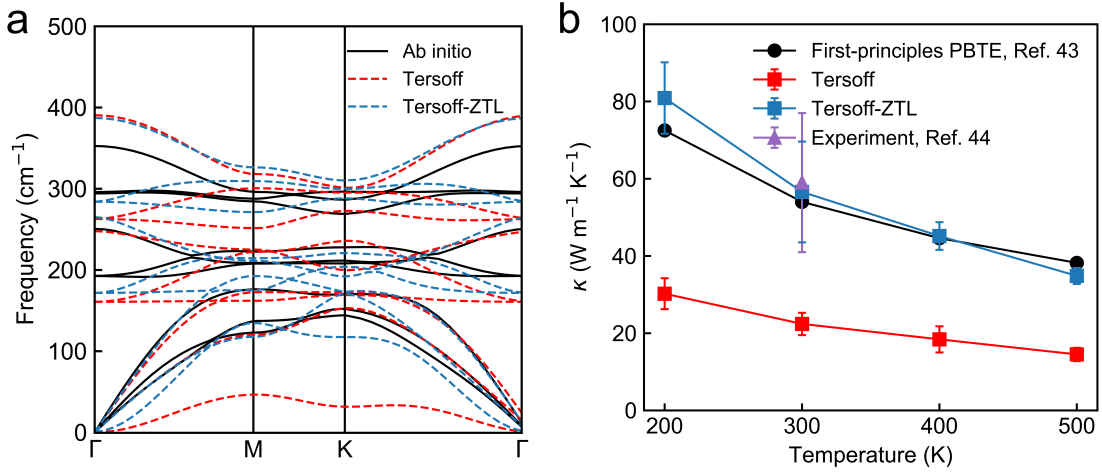


Figure 3.9. **Transferability test for the parameterized Tersoff potentials (Tersoff and Tersoff-ZTL) on thermal properties of monolayer MoSe<sub>2</sub>.** (a) Phonon dispersion predicted by the Tersoff potential in comparison to *ab initio* results. (b) Thermal conductivity predicted by the Tersoff potential in comparison to first principle calculations by solving the Peierls-Boltzmann transport equation (PBTE) [85] as well as experimental measurements on suspended monolayer MoSe<sub>2</sub> using optothermal Raman techniques [86]. The Tersoff-ZTL corresponds to the parameterized potential with the training data of "Tersoff" plus the three acoustic phonon modes, i.e., ZA, LA, and TA.

interatomic potentials with different levels of complexity. In all cases, the method is straightforward to implement, given the appropriate computer codes. Moreover, this approach enables the exploration of the intrinsic relationships between properties through correlation and principal component analyses, which is absent in other parametrization frameworks such as GARField [88] and Paramfit [89]. With the correlation matrix, one can a) evaluate the feasibility of improving the parametrization of a given potential; b) assess the parametrization flexibility of a given potential with the value of  $F$ . At this stage, the analyses are used to close the parametrization loop through selections made by the user. An automated workflow could be developed by adopting other machine learning algorithms such as logistic regression and decision tree on a cross-validating set, which would further minimize human intervention [79]. Such approach is left to future studies.

In the approach here presented, the choice of interatomic potentials and parametrization parameters constitute an iterative process. One should start by using computationally inexpensive properties (see

the Parametrization method section) for training, to cover a wider range of configurations and achieve better optimization efficiency. The correlation and principal component analyses are then employed to guide the selection of training and screening properties for the next iteration, e.g., exclude redundant properties from the training set or include properties into the training set after evaluating the effect on other properties. We note that simple expansion of the data base, without considering their correlation with other properties of interest, is not a suitable approach.

We identified intrinsic conflicting relationships between certain properties for the parameterized interatomic potentials and attributed such behaviors to the limitations of the functional forms. To examine if more sophisticated functional forms can alleviate this issue, we parameterized a reactive many-body potential for TMDCs (referred as REBO-TMDC) [53] using the same training data as Tersoff-ZTL. In comparison to Tersoff-ZTL, The REBO-TMDC shows improved accuracy on phase transition but decreased accuracy on several other properties. This suggests that the intrinsic conflicting roles of properties are always present and that more sophisticated interatomic potentials do not necessarily translate into better accuracy across all properties. Rather, as can be seen from the example of Tersoff and Tersoff-ZTL, attention needs to be paid as to how properties correlate for each functional form (potential).

We leave the parametrization of more complex functional forms, with a larger number of parameters, e.g., ReaxFF [90], for future work. Nevertheless, when equilibrium properties are the primary interest of parametrization, simpler interatomic potentials are worth exploring due to the ease of parametrization and better computational efficiency. Indeed, common interatomic potentials were found to be overdesigned for the purpose of exclusively modeling equilibrium properties including phonon dispersion and thermal transport in crystalline Si and Ge [59], thus suggesting sufficient flexibilities for parametrization. In either circumstance, our approach offers a framework for future studies aiming at expanding the capability of empirical interatomic potentials for quantifying unconventional chemical and physical phenomena in emerging new materials.

We highlight the better performance of the NSGA-III algorithm over several existing multi-objective global optimization algorithms. We also note that other multi-objective global optimization algorithms, e.g., MOES [91] and GARField [88], have been developed for parameterizing ReaxFF for molecular

crystals and SiC. Future work should perform comparison among existing approaches. Furthermore, for TMDCs, the transferability test can be expanded to other DFT calculations and *in situ* transmission electron microscopy observations including vacancy induced phase transition [77], formation of inversion domains [92], atomic morphologies of the crack tip [22], etc., which we leave for future exploration.

## CHAPTER 4

# Edge-Mediated Vacancy Annihilation of Monolayer Molybdenum Diselenide

## 4.1. Introduction

Structural defects, e.g., vacancies, dislocation, and grain boundaries, are ubiquitous in materials and play critical roles in controlling material properties [93]. This structure-property relationship becomes more dominant when the materials are atomically thin, i.e., in two-dimensional (2D) materials. For instance, sulfur vacancies in MoS<sub>2</sub> enable n-type doping [94] and can modify the electronic [94, 95], piezoelectric [96], and optoelectronic [95, 97] properties of the material. Similarly, in hexagonal boron nitride (h-BN), the NBVN (nitrogen vacancy adjacent to a nitrogen located in a boron site) sites enable room-temperature single-photon emission [98], whose spectral distribution can be further modulated by strain [99]. Those findings suggest possibilities to tune the properties of 2D materials at will through defect engineering, a promising route to facilitate their applications beyond their intrinsic capabilities [94].

For TMDCs, methods to modulate defects include chemical treatment [100], thermal annealing [92], electron beam irradiation [80, 92, 101–105], and plasma irradiation [106]. Specifically, electron beam irradiation with transmission electron microscopy (TEM) allows *in situ* observation of the creation and subsequent dynamics of defects, thus enabling direct comparison with atomistic simulations for the exploration of the underlying mechanisms. For instance, electron beam irradiation introduces chalcogen (sulfur and selenium) vacancies in monolayer MoS<sub>2</sub>, MoSe<sub>2</sub>, and WS<sub>2</sub> as a result of electron bombardment, and can trigger agglomeration of isolated vacancies into vacancy lines due to reduction in energy [92, 102, 105]. To date, most studies on defect manipulation with electron beam irradiation report generation and subsequent structural evolution of defects. Electron-beam-induced healing of pre-existing defects, on the

other hand, is much less explored. One study by Shen et al. reports healing of nanopores in monolayer MoS<sub>2</sub> as a result of the diffusion of surface adatoms to the vacancy sites [104]. With the capability of both creating and healing defects, electron beam irradiation may serve as a versatile technique for defect engineering in TMDCs and other 2D materials. Nevertheless, more experimental and theoretical investigations on electron beam-materials interactions, especially on the healing of defects, are necessary for fulfilling requirements present in engineering applications.

In this chapter, we investigate annihilation of vacancy clusters in monolayer MoSe<sub>2</sub> under electron beam irradiation. Through an *in situ* high-resolution TEM (HRTEM) study, we show that the annihilation of vacancy clusters is achieved by diffusion of vacancies from the clusters to the free edge near the vacancy clusters. Monte Carlo (MC) simulations, enabled by an interatomic potential parameterized for monolayer MoSe<sub>2</sub>, show that it is energetically favorable for the vacancies to locate at the free edge. We further compute the minimum energy pathway for the annihilation process of a representative vacancy cluster and conclude that electron beam irradiation, as well as prestress in the suspended monolayer MoSe<sub>2</sub>, are necessary to trigger the annihilation. Our study reveals a new mechanism of defect-healing in TMDCs and broadens the capability of electron beam for defect engineering of 2D materials.

#### 4.2. *In Situ* HRTEM Study of Vacancy Annihilation

Monolayer MoSe<sub>2</sub> flakes were synthesized by chemical vapor deposition (see Chapter 2). The flakes were transferred to Quantifoil holey carbon grids using polystyrene as the transfer polymer [29]. HRTEM characterization was conducted at 80 kV acceleration voltage, to reduce beam damage on the monolayer MoSe<sub>2</sub>, inside a FEI Titan 80-300 TEM with an image corrector for reducing both the chromatic and spherical aberrations. The as-synthesized MoSe<sub>2</sub> has a vacancy density that is comparable to CVD-grown MoS<sub>2</sub> flakes, as shown in Fig. 4.1 [107]. Free edges were created by fracture of flakes during the transfer process (Fig. 4.2). No obvious electron beam damage to the monolayer MoSe<sub>2</sub> was observed under an electron dose rate of  $1.4 \times 10^6 \text{ e}^- \cdot \text{nm}^{-2} \cdot \text{s}^{-1}$ . Vacancy clusters start to form under continuous electron irradiation at a dose rate of  $2.9 \times 10^6 \text{ e}^- \cdot \text{nm}^{-2} \cdot \text{s}^{-1}$ , as shown in Fig. 4.3. We note that the acceleration voltage (80 kV) is below the knock-on threshold voltage to displace Se atoms in MoSe<sub>2</sub> ( $\sim 190$  kV). The

creation of vacancy clusters can thus be attributed to: (1) ionization damage and (2) electronic excitation in the specimen which is shown to decrease the knock-on threshold voltage for S atoms in MoS<sub>2</sub> [103]. Although ionization damage reduces as the acceleration voltage increases, we found more severe beam damage to the monolayer MoSe<sub>2</sub> at 200 kV, suggesting the more dominant electron knock-on damage at such a condition.

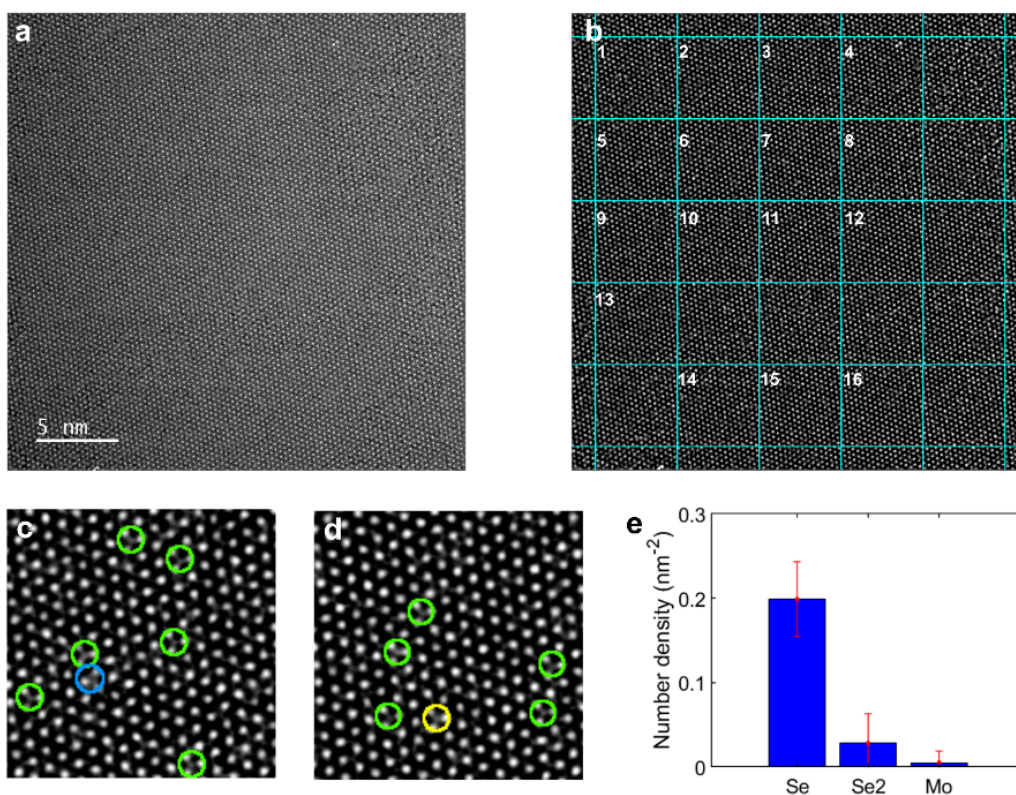


Figure 4.1. (a) High-resolution TEM image of a monolayer MoSe<sub>2</sub> flake. (b) The same image as shown in (a), after applying a Bandpass filter (lower band 0.09 nm, upper band 1.24 nm) and adjusting the brightness and contrast for more clear visualization of the defects. Grid of 5x5 nm was overlaid onto the image for the defect analysis. Regions clear from adsorbate were indexed in (b) and used for the quantification of vacancy density. (c-d) Defect analysis of two representative 5x5 nm region. Se monovacancies and Se<sub>2</sub> divacancies were identified and were highlighted by green and yellow circles, respectively. Mo vacancies were highlighted by blue circles. (e) Statistics of the number density of defects, acquired from 16 regions in (b). The average number densities are 0.199 nm<sup>-2</sup>, 0.028 nm<sup>-2</sup>, and 0.005 nm<sup>-2</sup> for Se monovacancy, Se<sub>2</sub> divacancy and Mo monovacancy, comparable to 0.12 nm<sup>-2</sup>, 0.02 nm<sup>-2</sup>, and 0.01 nm<sup>-2</sup> as measured in CVD-grown MoS<sub>2</sub> specimen

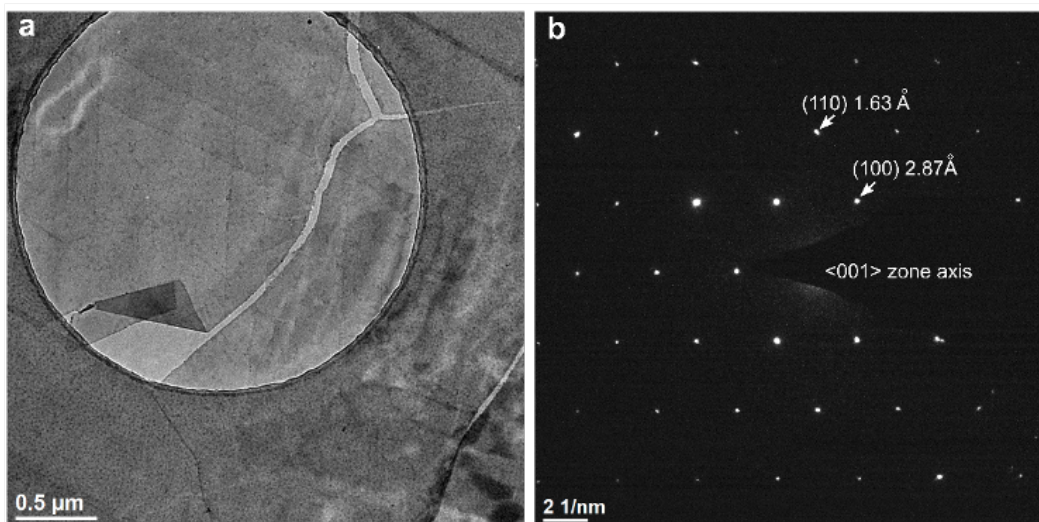


Figure 4.2. (a) A MoSe<sub>2</sub> flake that fractures after transfer. (b) Selected area diffraction of a region in (a).

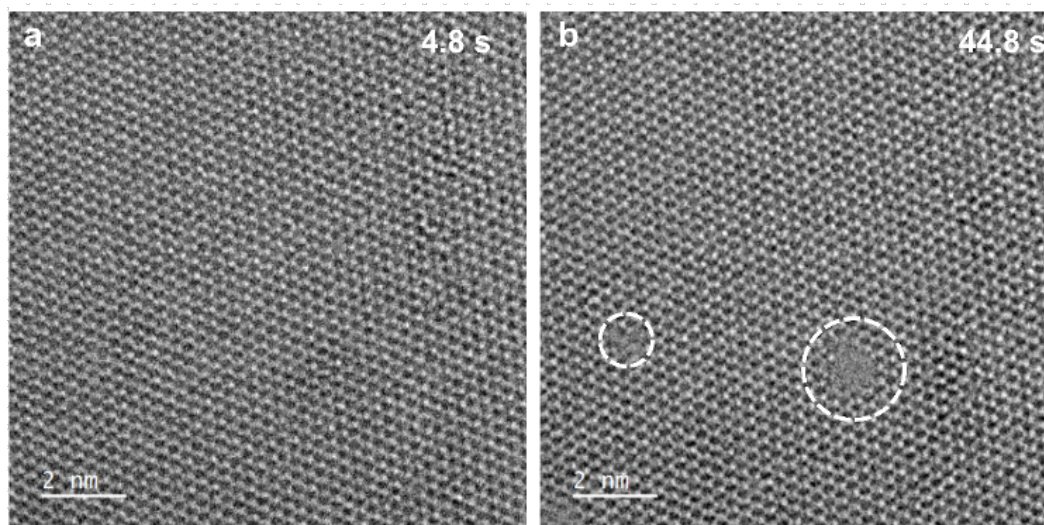


Figure 4.3. Evolution of the morphology of monolayer MoSe<sub>2</sub> under electron beam irradiation of (a) 4.8 s and (b) 44.8 s. The white dashed circles in (b) highlight the vacancy clusters that form due to electron beam irradiation. The electron dose rate is  $2.9 \times 10^6 \text{ e}^- \cdot \text{nm}^{-2} \cdot \text{s}^{-1}$ .

Under continuous electron beam irradiation, vacancy clusters start to form in the suspended MoSe<sub>2</sub> monolayer, as shown in Fig. 4.4. The vacancy clusters comprise aggregated Mo and Se<sub>2</sub> vacancies and adopt (truncated) triangular shapes similar to those in h-BN [108]. It can be determined from the HRTEM image (Fig. 4.4(c) and 4.4(f)) that the vacancy clusters possess a zigzag edge (i.e., surface), in agreement

with its lower energy in comparison to the armchair edge [109]. This conclusion is further corroborated by the FFT pattern (Fig. 4.4(a)). We compared the FFT pattern to the selected area diffraction pattern of the suspended monolayer MoSe<sub>2</sub> in Fig. 4.2 and confirmed that the six spots closer to the central spot correspond to those of the zigzag surface of monolayer MoSe<sub>2</sub>. As shown in Fig. 4.4(a), the reciprocal vectors of those spots are perpendicular to the edges of the vacancy clusters, which confirms that those edges have a zigzag termination. Similarly, the free edge adopts a serrated zigzag configuration. Under continuous electron beam irradiation at a dose rate of  $8.17 \cdot 10^6 \text{ e}^- \cdot \text{nm}^{-2} \cdot \text{s}^{-1}$ , vacancy clusters annihilate or decrease in size (Figure 4.4(b), 4.4(c)-(e), 4.4(f)-(h)). Another experiment conducted under the same conditions is shown in Fig. 4.5. In the two cases, we observed earlier annihilation of 1) vacancy clusters closer to the free edge (vacancy cluster (vc) 3 versus vc2 in Fig. 4.4(a), vc7 versus the rest in Fig. 4.5) and 2) smaller vacancy clusters (i.e., vc3 versus vc4 in Fig. 4.4(a)) in comparison to other vacancy clusters.

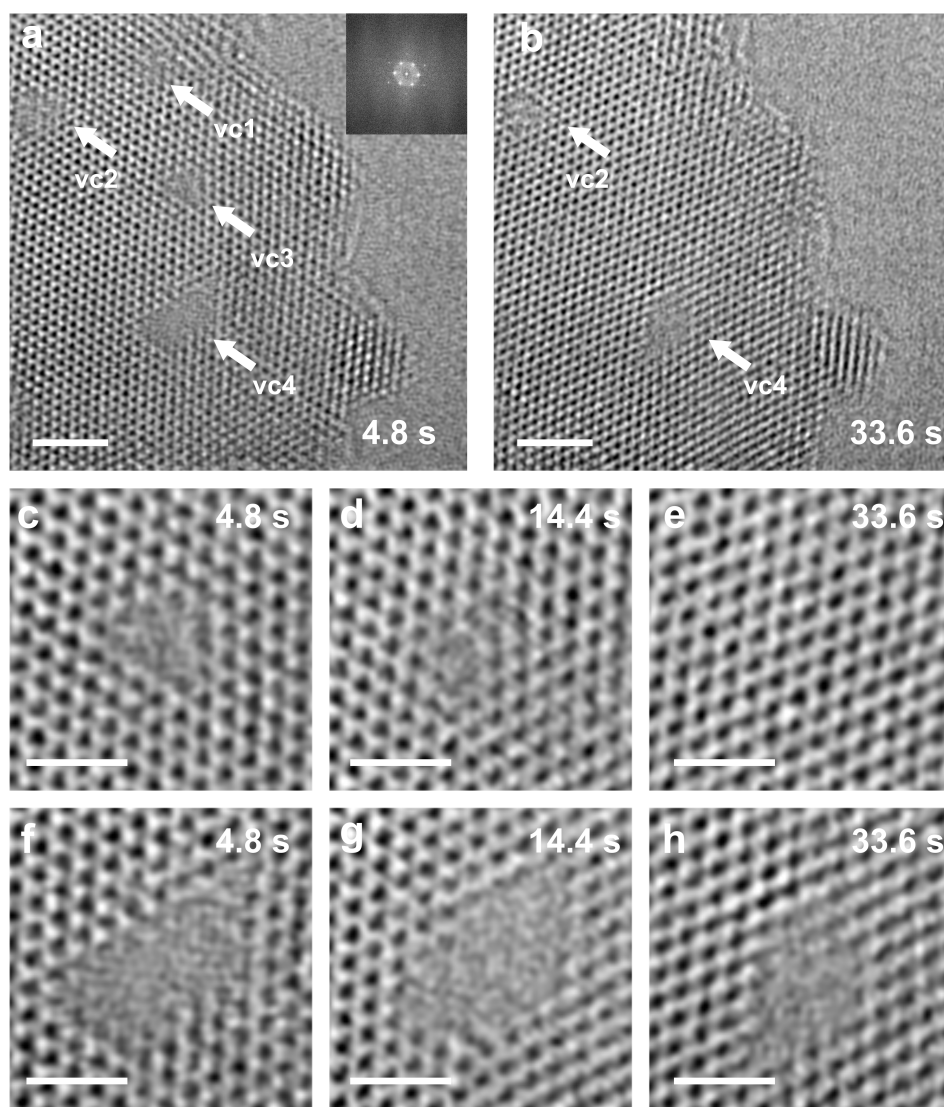


Figure 4.4. Vacancy annihilation under electron beam irradiation. (a-b) Structural evolution of the monolayer MoSe<sub>2</sub> specimen with vacancy clusters (referred as vacancy cluster 1(vc1) to vc4, respectively) near a free edge under continuous electron beam irradiation at (a) 4.8 s and (b) 33.6 s. vc1 and vc3 annihilate at 33.6 s. The inset image in (a) is the corresponding FFT pattern. The reciprocal vectors corresponding to the zigzag surface were plotted to illustrate that the edges of the vacancy clusters possess zigzag termination. (c-e) Structural evolution of vc3 in (a) at (c) 4.8 s, (d) 14.4 s, and (e) 33.6 s. (f-h) Structural evolution of vc4 in (a-b) at (f) 4.8 s, (g) 14.4 s, and (h) 33.6 s. The electron dose rate is  $8.17 \cdot 10^6 e^- \cdot \text{nm}^{-2} \cdot \text{s}^{-1}$ . All images were processed with a radial Wiener filter. Scale bars: 2 nm for (a) and (b) and 1 nm for (c-h).

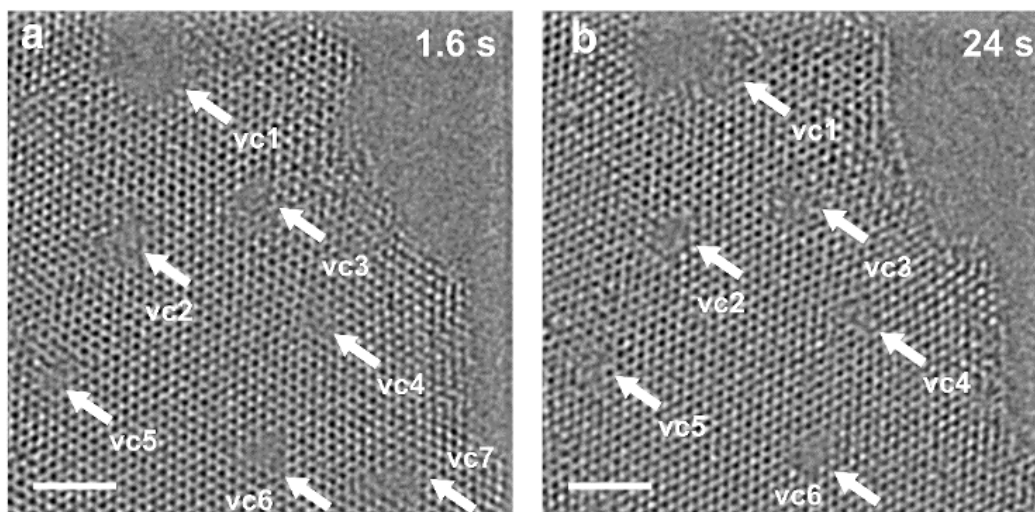


Figure 4.5. Vacancy annihilation under electron beam irradiation, conducted under the same experimental condition as that shown in Figure 4.4 for (a) 1.6 s and (b) 24 s of beam irradiation. Vacancy cluster vc 7 annihilates earlier than other vacancy clusters. Scale bar: 2 nm.

Notably, the annihilation process is accompanied by a decrease of atom columns between the vacancy clusters and the free edge, as shown in Fig. 4.6. While direct tracing of individual atoms was not conducted due to the inability to capture the fast atomic movements, such finding nevertheless implies the diffusion of atoms from the free edge to the vacancy cluster (and diffusion of Mo vacancies and Se<sub>2</sub> divacancies in the opposite direction). Mechanistically, the annihilation process is distinct from an earlier study on the repair of nanopores in MoS<sub>2</sub> under electron beam irradiation, which is mediated by the diffusion of surface adatoms [104]. Our observation suggests that surface annihilation of vacancies, as commonly observed in metallic systems [110], also exists in 2D materials such as TMDCs. Qualitatively, the annihilation of vacancy clusters can be interpreted as an Ostwald ripening process (i.e, an increase in the size scale of a second phase in the matrix) [111], if one considers the vacancy clusters as the second phase and the free edge as the boundary of a much larger vacancy cluster. Nevertheless, a more quantitative analysis requires consideration of anisotropic edge configurations as well as motion restrictions for each type of atom, as discussed next.

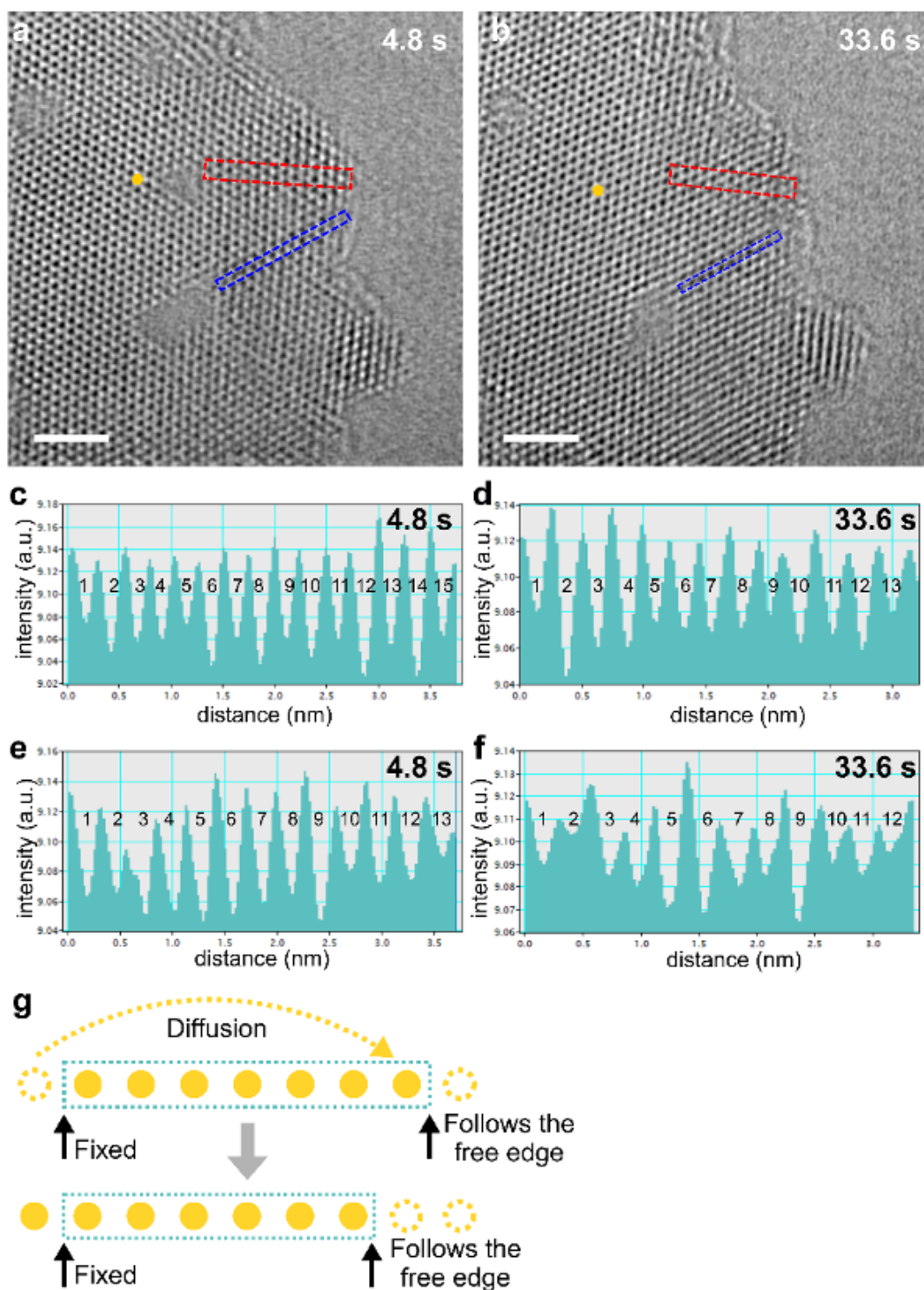


Figure 4.6. Atom column mapping from intensity profile. (a-b) Same images of vacancy annihilation as shown in the main manuscript ( Fig. 4.4(a) and (b), respectively). Two regions, highlighted by the red and blue dashed rectangle, were selected for the intensity profile analysis. The left boundaries of the two regions are fixed in position, while the right boundaries of the two regions correspond to the location of the free edge. Scale bars: 2 nm. (c) Intensity profile of the red dashed rectangular region for (a). (d) Intensity profile of the red dashed rectangular region for (b). The number of atom columns (dark blobs in (a) and (b), valleys in (c) and (d)) decreases from 15 to 13 (e) Intensity profile of the blue dashed rectangular region for (a). (f) Intensity profile of the blue dashed rectangular region for (b). The number of atom columns decreases from 13 to 12. (g) Illustration on how a reduction of atom columns within the as-defined regions reflect diffusion of atoms from the vacancy clusters to the free edge. We tracked the position of an atom column at the left side of the vacancy clusters (highlighted as yellow circles in (a) and (b)) and confirmed that rigid body motion of the entire structure or drift of the image, which may result in the same observation, did not occur. As such, the reduction of atom columns is solely due to diffusion of atoms.

### 4.3. Exploration of Thermodynamic Driving Force through Monte-Carlo Simulations

To explore the driving force for the edge-mediated vacancy annihilation, we simulated such a process with the Monte Carlo (MC) method. The initial structure for the simulation (Fig. 4.7(a)) was configured to reproduce the experimental observation (see discussion below for different initial edge configurations). Specifically, only Mo monovacancies and Se<sub>2</sub> divacancies (Se atom above and below the middle Mo layer) were included in the simulation; Se monovacancies and antisite defects, i.e., defects in which one atom occupies the site for the other type of atom(s), were not discernable from the HRTEM images and as a result were not introduced. We defined the MC move as swapping between vacancies and their neighboring atoms within a cutoff distance  $d_{max}$  (60 Å), and adopted the Metropolis MC rules for accepting and rejecting the move. The cutoff distance setting accelerates the evolution of the MC simulations and allows us to better mimic the collective motions of atoms as observed experimentally. It allows the MC simulations to sample random moves with higher possibilities of occurrence. However, this algorithm ignores the large reaction barriers imposed by the intermediate configurations, and as a result, does not reveal the driving force for the diffusion process. For the evaluation of energy, we used a Tersoff potential that we parameterized for monolayer MoSe<sub>2</sub> with an emphasis on non-equilibrium properties, e.g., vacancy formation energies, surface energies, and uniaxial tension, etc [47].

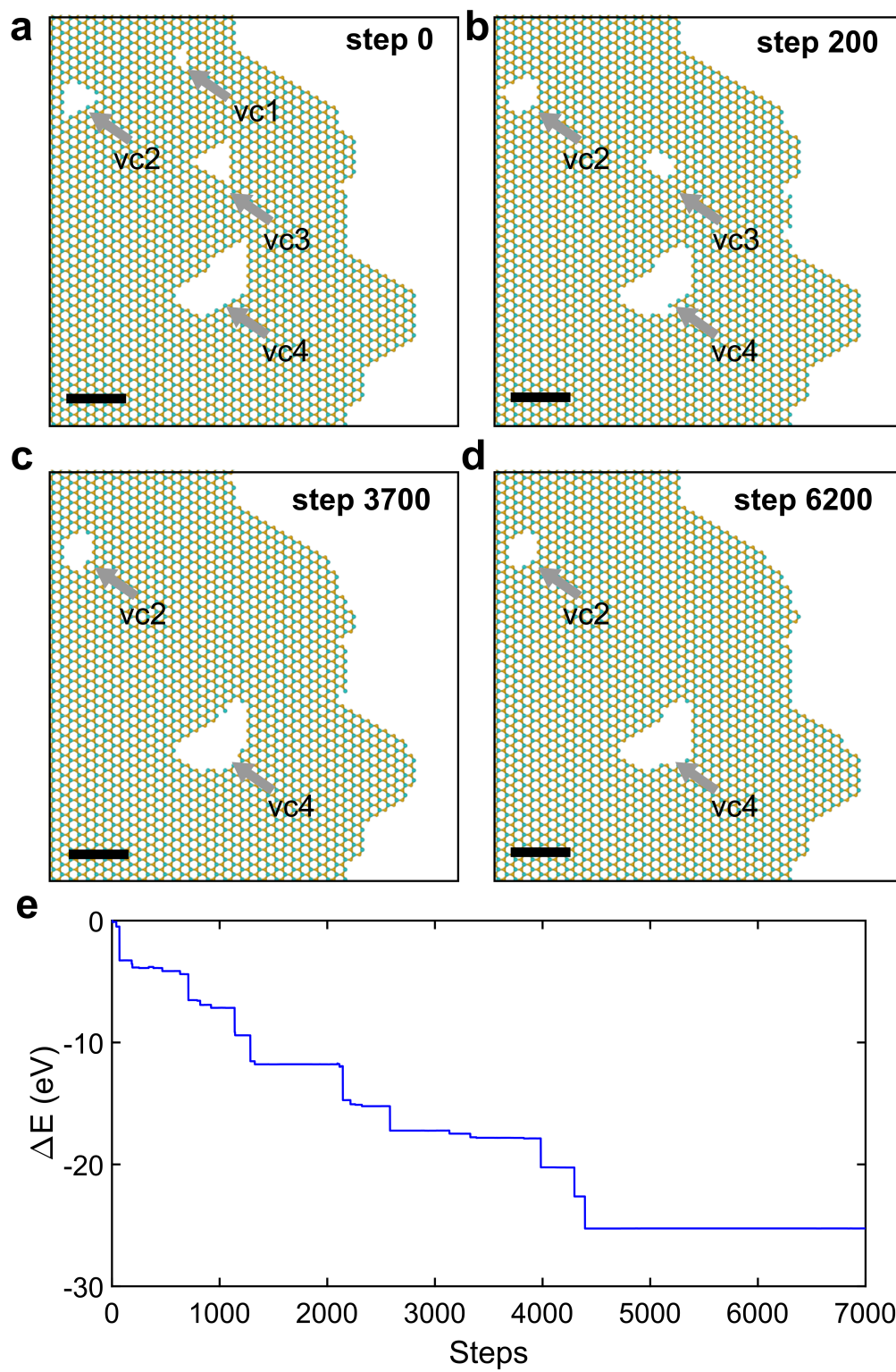


Figure 4.7. VA representative Monte Carlo (MC) simulation of the vacancy annihilation process at 300 K. (a-d) Simulation snapshots at (a) step 0, (b) step 200, (c) step 3700, and (d) step 6200, respectively. The initial structure (a) is constructed from Figure 1a by mapping the atom columns. Extra atoms are put in the simulation system (not shown in the figures) at the top, left, and bottom of the region of interest to exclude boundary effects. Mo atoms are colored cyan, and Se atoms are colored orange. Scale bar: 2 nm. (e) Change of the total energy as a function of MC steps.

Fig. 4.7 shows a representative MC simulation at 300 K that reproduces the experimental observation: vc1 and vc3 annihilate while the rest two decrease in size, and the free edge contracts. As the annihilation proceeds, the energy of the system decreases in a stepwise manner (Fig. 4.7(e)). Such data indicates that it is energetically favorable for the vacancies to locate at the free edge in comparison to the vacancy clusters. Moreover, interactions between vacancy clusters were observed in MC simulations. Such interactions are identified in h-BN [108] and also in our system between vc1 and vc2 (see Supplementary Movie 1).

The aforementioned findings can be explained by the change of coordination number of atoms. In Fig. 4.7, the coordination number of an atom is twice the number of visible bonds since each bond is an overlay of 2 bonds. A Mo ( $\text{Se}_2$ ) atom(s) has a coordination number of 6 in pristine  $\text{MoSe}_2$  and can be either 4 or 2 (Fig. 4.7(b)) when they are the terminating atom(s) at the edge. For vacancy sites in a cluster, the coordination numbers can be 4, 2, and 0, corresponding to  $60^\circ$  corners, other sites at the cluster edge, and inside the cluster, respectively, as shown in Fig. 4.8. An increase in coordination number decreases the energy and is therefore favorable. The annihilation process always initiates from the  $60^\circ$  corners of the vacancy cluster, advances to other sites at its edge, and terminates when no swap attempt can increase or maintain the coordination number. Larger vacancy clusters have more sites with low coordination numbers ( $< 4$ ) and as a result are less likely to completely annihilate. Vacancy clusters away from the free edge have more restricted access to atoms at the free edge and therefore are less likely to annihilate<sup>1</sup>. We note that temperature within commonly reachable range ( $< 1500$  K) has a minimum effect on the annihilation due to the large increase in energy when coordination number decreases.

---

<sup>1</sup>This is controlled by an arbitrary cutoff distance  $d_{\text{max}}$  but nevertheless reflects the real physics.

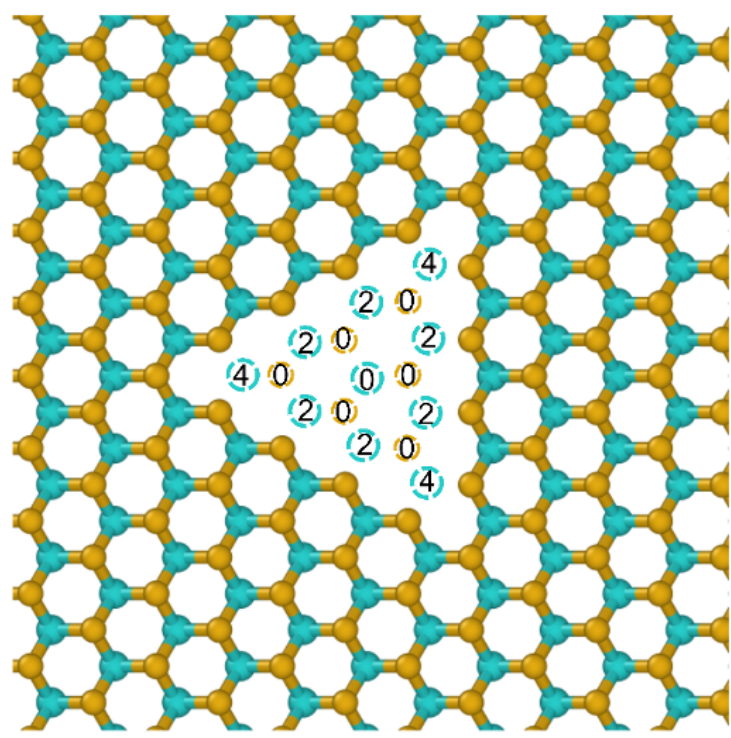


Figure 4.8. Coordination number of a vacancy cluster. The vacancy sites are marked by dashed circles. The numbers represent the coordination number if an atom(s) occupies that site. Cran atoms (circles) represent Mo atoms (vacancies), and orange atoms (circles) represent Se atoms ( $\text{Se}_2$  vacancies). Vacancy sites at the  $60^\circ$  corners have a coordination number of 4. The rest atoms at the cluster edge have a coordination number of 2. Sites inside the cluster have coordination number of 0. The coordination number for a site will increase as its nearby sites are filled.

The free edge in Fig. 4.7 possesses either a Mo- or Se-zigzag configuration with a coordination number of 4. Besides those two types, the Mo-Klein edge is also found to be stable in nanoporous  $\text{MoS}_2$  films grown with molecular beam epitaxy under high Mo flux [46], as shown in Fig. 4.9. It can be created by removing the outermost Se atoms in Se-zigzag edge, leaving exposed Mo atoms with a coordination number of 2. As shown in Table 4.1, converting 50%<sup>2</sup> of the Se-zigzag edge to the Mo-Klein edge increases the probability of annihilation for vc2 and vc3, highlighting its notable effect on the annihilation.

<sup>2</sup>We note that the ratio is 70% in  $\text{MoS}_2$  films grown with high Mo flux. (see Zhao et al., Nano Lett., 2018, 18, 482-490.). Since such a Mo-rich condition was not applied in our synthesis protocol, we decreased that ratio to 50%.

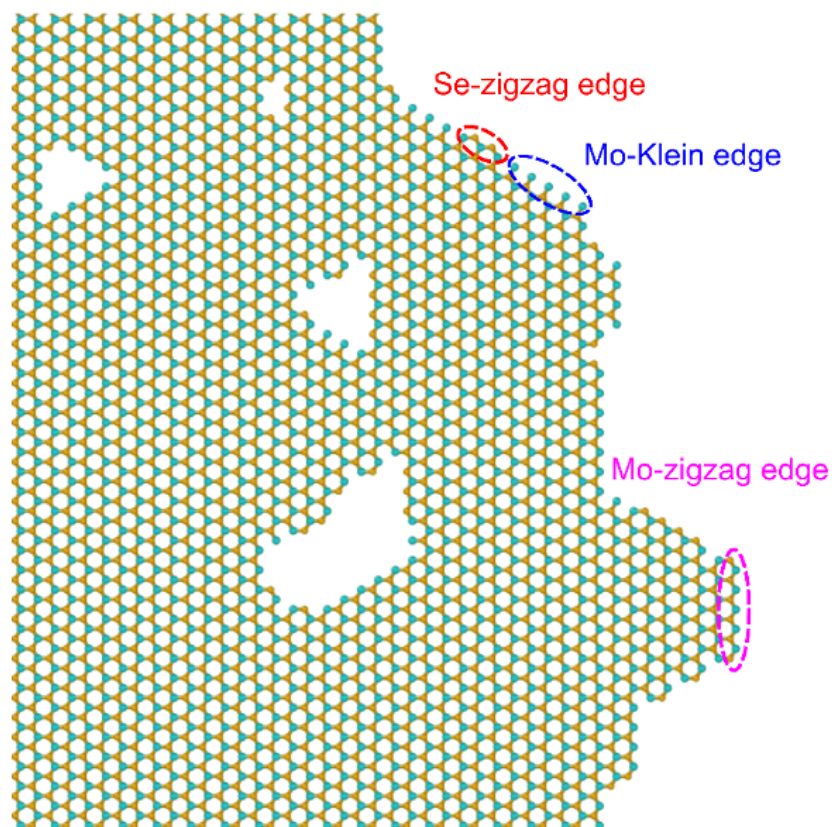


Figure 4.9. Initial configuration for the MC simulation with Mo-Klein edge introduced randomly into the system. The ratio between Mo-Klein and Se-zigzag edge is 1 to 1. The Se-zigzag, Mo-Klein, and Mo-zigzag edge are highlighted in the figure. Mo atoms are colored cyan, and Se atoms are colored orange.

We note a low acceptance rate of the MC simulations for diffusion events with an increase of energy, i.e.,  $\Delta E > 0$ . To verify that this is not due to the parametrization of the interatomic potential, we compared results of several simplified vacancy diffusion events, predicted by the interatomic potential, against first-principle simulations. As shown in Fig. 4.10 and 4.11, first-principle simulations for vacancy diffusion instances with  $\Delta E > 0$  also predict  $\Delta E$  values that are much higher than thermal energy ( $k_b T$ ), which agrees with results obtained from the parameterized interatomic potential. Hence, the low acceptance rate is embedded in the as-studied system and further justifies our selection of the cutoff distance, which accelerates the process.

Table 4.1. Probability of annihilation for the vacancy clusters under different initial edge configurations. The zigzag-only structure (Fig. 4.7(a)) contains Mo- and Se-zigzag edges, while the Zigzag and Mo-Klein configuration (Fig. 4.9) contains a third type: the Mo-Klein edge. Specifically, the ratio between Se-zigzag and Mo-Klein is set to be 1:1. The probability was calculated from 60 simulations with different random seeds.

Vacancy clusters	Zigzag only	Zigzag and Mo-Klein
vc1	1	1
vc2	0	0.07
vc3	0.03	0.97
vc4	0	0

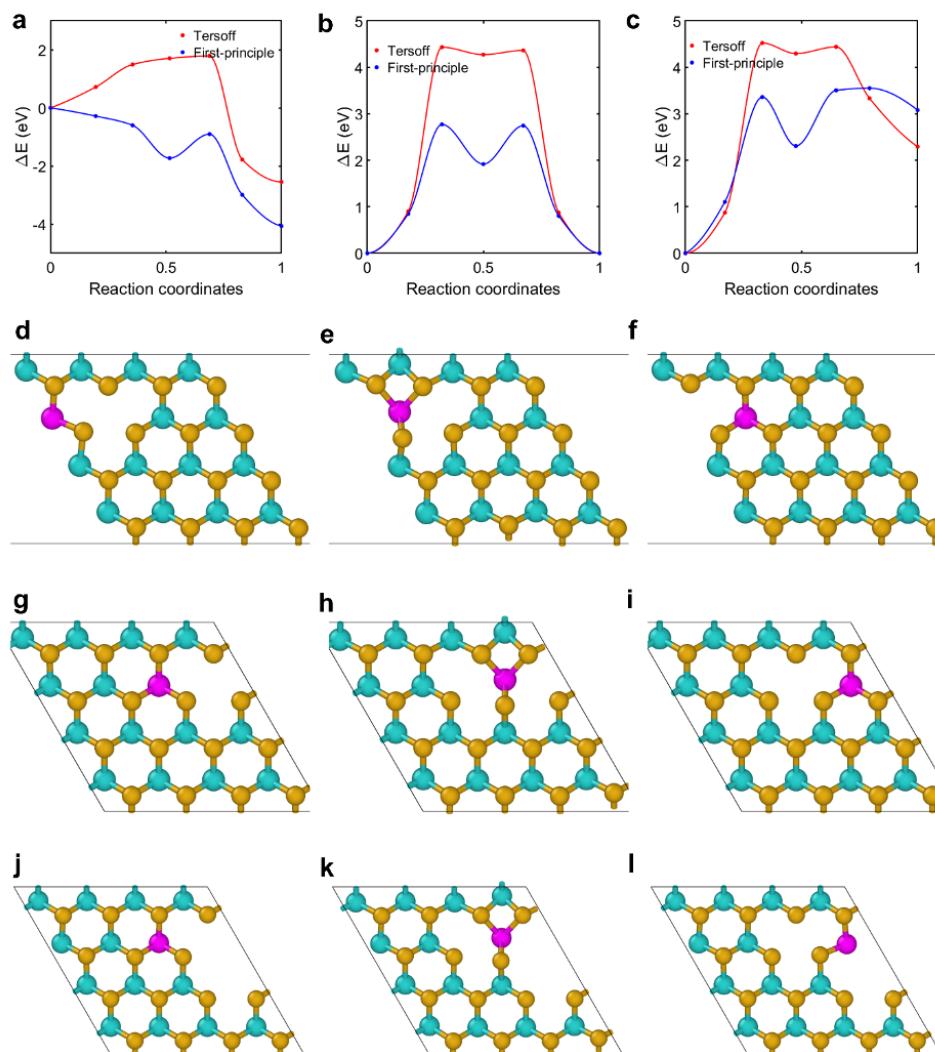


Figure 4.10. NEB simulation results of first-principle simulations versus the parameterized Tersoff potential for (a) diffusion of the Mo vacancy to the free edge of  $\text{MoSe}_2$ , (b) diffusion of the Mo vacancy inside pristine  $\text{MoSe}_2$ , and (c) diffusion of the Mo vacancy from a vacancy cluster inside  $\text{MoSe}_2$ . (d-f) Snapshots of the diffusion path for (a) at (d)  $\text{RC}=0$ , (e)  $\text{RC}=0.5$ , and (f)  $\text{RC}=1$ . (g-i) Snapshots of the diffusion path for (b) at (g)  $\text{RC}=0$ , (h)  $\text{RC}=0.5$ , and (i)  $\text{RC}=1$ . (j-l) Snapshots of the diffusion path for (c) at (j)  $\text{RC}=0$ , (k)  $\text{RC}=0.5$ , and (l)  $\text{RC}=1$ . In (d-l), Mo atoms are colored cyan, and Se atoms are colored orange. The Mo atom undergoing the diffusion is highlighted by purple.

#### 4.4. Kinetics Study via Nudged Elastic Band Simulations

The MC simulations are limited in revealing the kinetics of the annihilation process, e.g., diffusion barriers for the vacancy. Such information is embedded in the kinetic Monte Carlo (kMC) method [112, 113], which is not applied herein due to the complexities of our system in both composition and configuration. Indeed, the MC simulations resemble the experimental observations better and circumvent several technical challenges one would encounter using kMC simulations. To complement MC simulations, we explored the annihilation kinetics of a specific vacancy cluster, i.e., vc1 (Fig. 4.12), as means to extrapolate a general picture for our system. The complete annihilation process of vc1 is hypothesized to be achieved by the sequential annihilation of each individual vacancy site (i.e., two Mo vacancies and one Se<sub>2</sub> vacancy), initiating at either Mo vacancy at the corner of vc1. For each individual vacancy site, its annihilation is hypothesized to be composed of a sequence of vacancy-hopping events. For instance, the Mo vacancy (Fig. 4.12(a)), in each hopping event, diffuses to its nearest neighboring site until it reaches the edge and collectively moves the entire layer of Mo atoms inward. We computed the minimum energy path (MEP) of each vacancy-hopping event with the climbing image nudged elastic band (CI-NEB) method [48, 49] and combined them into one curve (Fig. 4.12(b)). The system for the CI-NEB simulation is identical to the MC simulations. We note that the local stress field may be affected by the free edge, as has been shown to contribute to vacancy dynamics in suspended monolayer MoS<sub>2</sub> [102]. Similarly, vacancy clusters may interact through their stress fields, as inferred from studies in graphene, which show that vacancies and divacancies stress fields are equivalent to an edge dislocation dipole [114]. To this end, energy minimization is conducted during each step of the CI-NEB simulation to account for the above elastic driving forces. The MEP varies according to local atomic configurations, and the completion of this process results in a slight decrease of energy due to local structural relaxation. Following the annihilation of the Mo vacancy, the Se<sub>2</sub> divacancy (Fig. 4.12(c)) and the Mo vacancy (Fig. 4.12(e)) annihilate in a similar manner, as shown by their MEP, Fig. 4.12(d) and Fig. 4.12(f), respectively. The biggest decrease in energy is observed in Fig. 4.12(f) when the net coordination number of the system increases by 4. This agrees with the MC simulations and confirms that the annihilation process is energetically favorable.

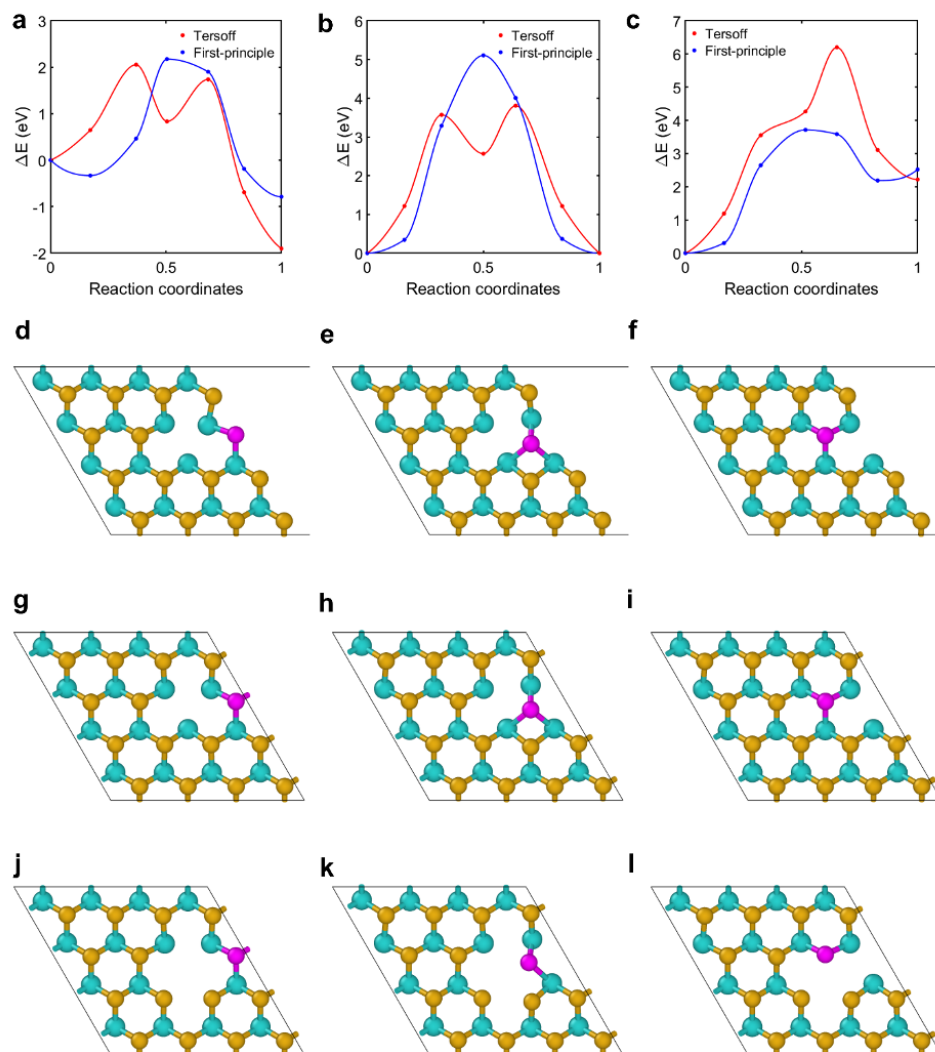


Figure 4.11. NEB simulation results of first-principle simulations versus the parameterized Tersoff potential for (a) diffusion of the Se<sub>2</sub> divacancy to the free edge of MoSe<sub>2</sub>, (b) diffusion of the Se<sub>2</sub> divacancy inside pristine MoSe<sub>2</sub>, and (c) diffusion of the Se<sub>2</sub> divacancy from a vacancy cluster inside MoSe<sub>2</sub>. (d-f) Snapshots of the diffusion path for (a) at (d) RC=0, (e) RC=0.5, and (f) RC=1. (g-i) Snapshots of the diffusion path for (b) at (g) RC=0, (h) RC=0.5, and (i) RC=1. (j-l) Snapshots of the diffusion path for (c) at (j) RC=0, (k) RC=0.5, and (l) RC=1. In (d-l), Mo atoms are colored cyan, and Se atoms are colored orange. The Se<sub>2</sub> atoms undergoing the diffusion is highlighted by purple.

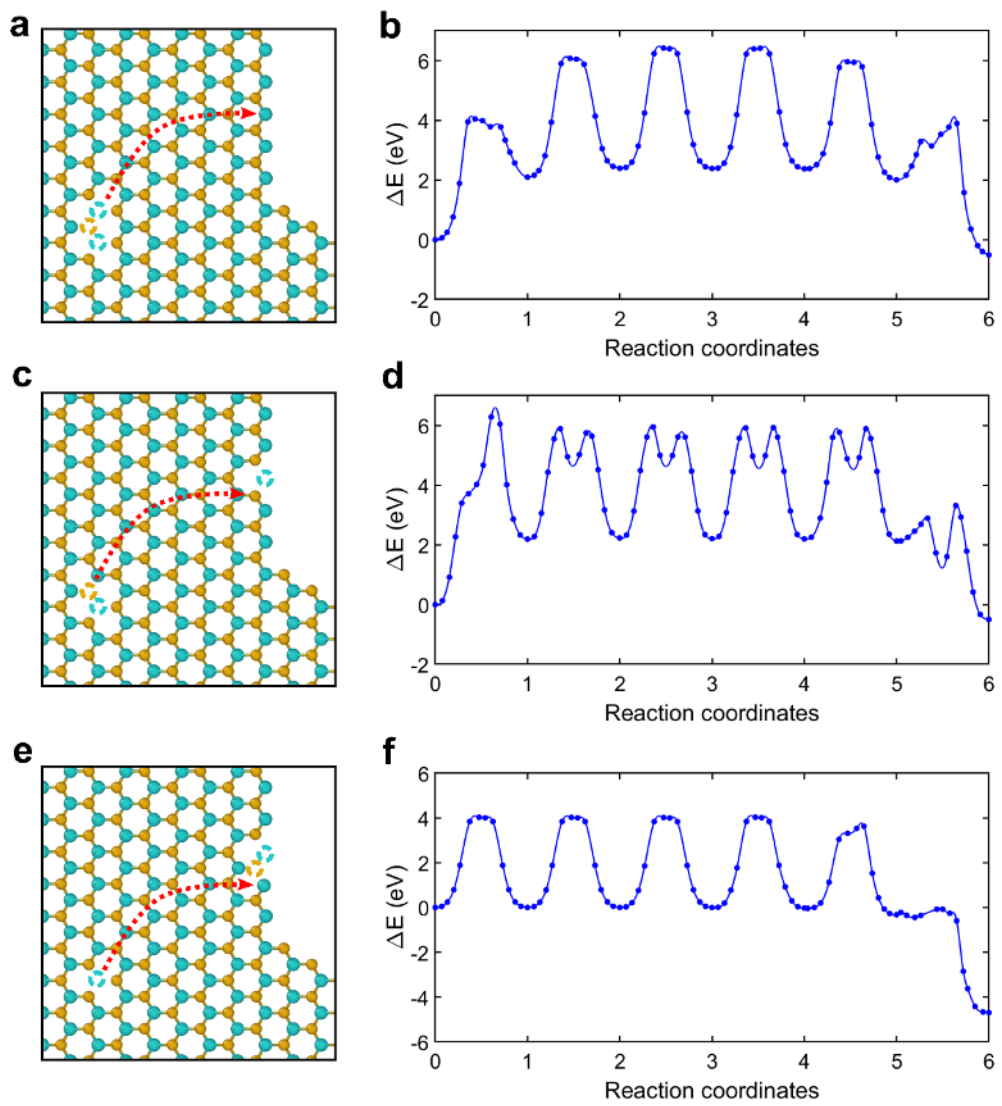


Figure 4.12. Proposed vacancy annihilation process for vc1. (a-b) Atomic snapshot (a) and minimum energy pathway (MEP) (b) of a Mo vacancy undergoing sequential hopping from the vacancy cluster to the free edge, which causes the vacancy site to annihilate. The snapshot (a) corresponds to reaction coordinates (RC) = 0 in (b). (c-d) Atomic snapshot (c) and minimum energy pathway (d) of the sequential hopping of the Se<sub>2</sub> vacancy. The snapshot (c) corresponds to RC = 6 in (b) and RC = 0 in (d). (e-f) Atomic (e) and minimum energy pathway (f) of the sequential hopping of the Mo vacancy. The snapshot (e) corresponds to RC = 6 in (d) and RC = 0 in (f). Complete annihilation of vc1 (RC = 6 in (f)) decreases the energy of the system by 5.7 eV. In (a), (c) and (e), the arrow indicates the hopping direction and destination of the vacancy, and the dashed circles represent vacancies. Mo atoms and vacancies are colored cyan, and Se atoms and vacancies are colored orange. For better visualization of the diffusion path of the individual vacancies, other vacancy clusters were not shown in (a), (c), and (e).

The activation barriers of vacancy-hopping are 0.77, 3.70, and 6.29 eV for a Se<sub>2</sub> divacancy, and 0.24, 1.89, 3.59, and 4.00 eV for a Mo vacancy, all of which are larger than thermal energy at room temperature ( $\sim 0.026$  eV). This suggests the necessity of other energy sources in assisting the barrier-hopping events. Electron beam irradiation is one of such source, as has been found to introduce vacancy migration in several 2D materials including graphene [115], h-BN [108], MoS<sub>2</sub> [101, 102, 116], and MoSe<sub>2</sub> [92]. The maximum energy that can be transferred to an atom from an electron in an elastic scattering is given as [117]:

$$E_{max} = \frac{2ME_0(E_0 + 2M_0C^2)}{2ME_0 + (M + m_0)^2c^2} \quad (4.1)$$

where  $M$  is the mass of the atom,  $E_0$  is the incident beam energy,  $m_0$  is the mass of an electron, and  $c$  is the speed of light. At 80 keV electron beam energy,  $E_{max}$  for Mo and Se atom is 1.97 and 2.40 eV, which suggests that elastic scattering due to electron beam irradiation is not sufficient for the vacancies to overcome the energy barriers in all the scenarios of Fig. 4.12. We identify pre-stress in the suspended membrane as another source of energy for barrier-hopping events of the vacancies. To quantify the magnitude of strain in the as-observed system, we adopted the structural template matching method, developed by Madsen et al [118], which uses the equilibrium lattice constant as the reference and is capable of revealing absolute strains. An average compressive strain of 9.3% and 10.3% (Fig. 4.13) was identified along the armchair and zigzag direction, respectively. The compressive strain should facilitate

the diffusion of vacancies to the free edge of the specimen, analogously to the Nabarro-Herring creep mechanism in metals [119]. It has also been shown that the prestress in suspended monolayer MoS<sub>2</sub> can lead to spontaneous crack propagation when the monolayer is punctured by the electron beam [22].

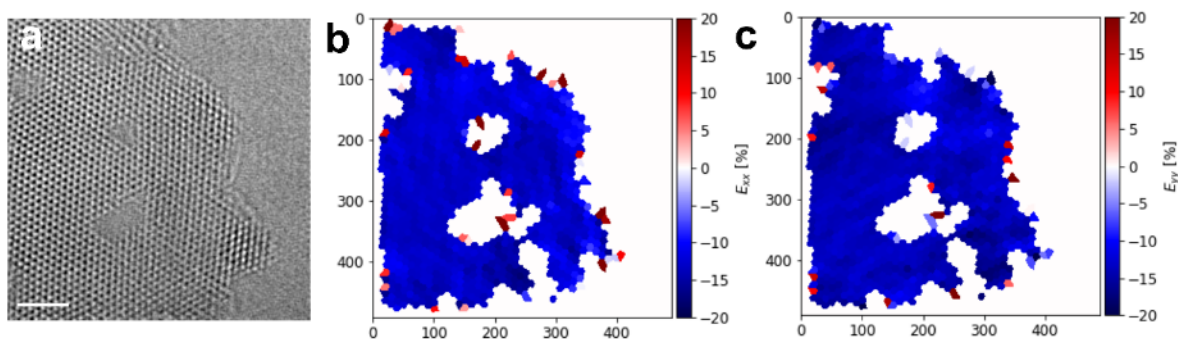


Figure 4.13. (a) HRTEM image used for the strain analysis, identical to Fig. 4.4(a). Scale bar: 2 nm. (b-c) The Green-Lagrangian strains,  $E_{xx}$  and  $E_{yy}$ , respectively. A lattice constant  $3.267 \text{ \AA}$ , obtained from selected area diffraction of multiple regions, was used as the reference. The average  $E_{xx}$  and  $E_{yy}$  of the region is  $-9.3\%$  and  $-10.3\%$ , respectively

For the as-studied atomic systems, we note size limitations of first-principle NEB simulations in capturing the effect of the free edge and other vacancy clusters on vacancy-hopping. To verify the accuracy of NEB simulations based on the interatomic potential, we constructed simplified atomic models to compare results obtained from the interatomic potential against those from first-principle NEB simulations. The simplified models include the following cases for a Mo monovacancy and Se<sub>2</sub> divacancies: diffusion (of the vacancy) to the free edge, diffusion from the vacancy cluster, and diffusion within pristine MoSe<sub>2</sub>. As shown in Fig. 4.10 and Fig. 4.11, deviations of energy barriers from the first-principle results, in the range of 0.12-2.49 eV, were identified for the parameterized interatomic potential. Given that the as-adopted interatomic potential is more accurate than existing ones for monolayer MoSe<sub>2</sub> on large-deformation pathways [47], we attribute such discrepancies to intrinsic limitations on the transferability of interatomic potentials. However, such deviations do not affect the conclusion that other sources of energy, besides the electron beam irradiation, are necessary for vacancy-hopping since the energy barriers

computed from first-principle simulations are still higher than the energy provided by the electron beam as computed from equation 4.1.

#### 4.5. Chapter Summary

We report HRTEM observation of edge-mediated annihilation of vacancy clusters in monolayer MoSe<sub>2</sub> under electron beam irradiation at room temperature. We conduct MC simulations and confirm that it is energetically favorable for the vacancies to locate at the free edge in comparison to the vacancy clusters as the former configuration provides a larger coordination number. The kinetics of the annihilation is explored on a proposed annihilation pathway for a vacancy cluster. The large activation barrier in comparison to thermal energy suggests the necessity of electron beam irradiation and prestress in the suspended monolayer in triggering the annihilation process.

It has been shown that the electronic properties of TMDCs can be tuned by modifying the edge configuration and vacancy concentrations. The Mo-zigzag and Mo-Klein edges in MoS<sub>2</sub> are metallic in comparison to the semiconducting MoS<sub>2</sub> basal plane [46], and sulfur vacancies in MoS<sub>2</sub> can introduce n-type doping [94, 95]. To this end, our findings reveal a new interaction mechanism between the electron beam and TMDCs, which may be used to fine-tune the properties of TMDCs and other 2D materials through defect-engineering. Moreover, in the context of fracture of 2D materials, our findings suggest possible interactions between vacancies and cracks that may alter crack propagation and fracture properties of 2D materials. In the absence of electron beam irradiation, such interactions may resemble the creep mechanism in metallic materials and may affect the fracture toughness of 2D materials.

We show that the vacancy annihilation process preferably initiates from atomic sites with lower coordination numbers. The atomic configurations with lower coordination numbers, e.g., vacancies, can be introduced by post-treatment such as electron beam irradiation and also during the growth of the material. For instance, Zhou et al. report edge reconstructions in CVD-grown monolayer MoS<sub>2</sub> flakes under a Mo-rich growth environment [120]. The reconstructed edges contain monosulfur vacancies and unsaturated Mo atoms. Those surface configurations may further facilitate the annihilation process, similar to the Mo-Klein edge herein studied. We did not observe such an edge reconstruction herein probably due to different

growth environments. We leave such investigation to future studies. We restrict the computational studies herein to  $\text{Se}_2$  divacancies because they are readily visible in the HRTEM images, which allows us to compare our simulation results directly to those images. While Se monovacancies appear to be more abundant in CVD-grown  $\text{MoSe}_2$  samples, they are not easily discernable in the aforementioned HRTEM images because the difference in brightness, which is used to discern Se monovacancies under TEM, is not trustworthy when the entire atomic structures undergo major structural evolution. Such a task (and the study of Se monovacancy diffusion) is more suitable to be conducted under STEM with the utilization of Z-contrast [121]. Given the numerous configurations and diffusion pathways for Se monovacancies in the system studied herein, direct experimental observation of Se monovacancy diffusion pathway, possibly with STEM, is necessary to reveal single vacancy diffusion mechanism. We leave such investigation to future studies.

## CHAPTER 5

## Quantification of Intrinsic Fracture Toughness of 2D Materials through Indirect Mechanical Testing

### 5.1. Introduction

Fracture mechanics analyzes and prevents catastrophic failure of materials with existing cracks and flaws. While this field has traditionally pivoted around studies of large-scale parts such as hull of ships and airplane fuselages [122], increasing attention has been drawn toward the exploration of micro- and nano-scale fracture problems, as spurred by rapid developments in realms such as microelectronics [123] and biomimetic materials design [124]. The application of two-dimensional (2D) materials in next-generation electronics [125–127] represents one of such stimulation. The past decade has seen significant progress in the growth, transfer, and assembly of 2D materials [128] such that the mechanical reliability of 2D materials in CMOS technology has become a practical engineering concern. Besides, the unique monolayer structures of 2D materials allow the observation of the propagation of atomically-sharp cracks [22, 129], which facilitates fundamental understanding of materials failure and enables comparison to theoretical predictions at such length scale, i.e., the Griffith criterion.

The aforementioned scientific and engineering merits call for techniques that can provide intrinsic fracture toughness of 2D materials with high accuracy. Molecular dynamics (MD) simulations based on interatomic potentials are powerful tools for such a purpose, but their predictive powers are not always reliable. In fact, interatomic potentials parameterized primarily for equilibrium properties often show poor transferability at large deformation regimes (where fracture occurs), and reparametrization with augmented training data or improved protocols are necessary [47]. Direct fracture tests using *in situ* experimental techniques can provide reliable results but suffer from extremely low throughput. A typical experiment involves 1) transfer of the 2D flakes from the growth substrate (or the solution phase)

onto a microelectromechanical system, 2) definition of a regular sample geometry with focused ion beam (FIB) milling, and 3) creation of a crack with either electron beam (for *in situ* TEM experiments) or FIB milling. The rate of a successful measurement after all those steps is very low. Nevertheless, some pioneering *in situ* scanning electron microscopy (SEM) fracture tests for monolayer graphene [130] and h-BN [131] have been conducted. In both studies, the measured fracture toughness exceeds theoretical values according to the Griffith’s criterion, which appears contradictory to their brittle nature in their pristine states. The higher fracture toughness was attributed to the existence of grain boundaries for graphene, and structure-induced crack deflection and branching for h-BN, both validated solely with computer simulations. Obtaining intrinsic fracture properties of 2D materials is the first step of evaluating their durability in applications. To date, such measurements are still lacking.

In this chapter, we report the first measurement of the intrinsic fracture toughness of 2D materials that approaches values predicted by the Griffith’s criterion. We conduct indirect *in situ* high-resolution TEM (HRTEM) fracture tests as well as MD fracture tests based on independently parametrized interatomic potentials, and calculate the critical energy release rate, i.e., the J-integral [132, 133], from the atomic strain/stress fields in the vicinity of crack tip. We demonstrate validity of our approach on monolayer MoS<sub>2</sub> and MoSe<sub>2</sub>, two types of 2D materials belonging to the transition metal dichalcogenides (TMDC) family. Our analyses constitute an integrated experimental/numerical framework for accurate quantification of the intrinsic fracture properties of 2D materials, which may expedite the exploration of such properties for emerging 2D materials.

## 5.2. *Ab Initio* Calculations for the Generation of Training, Screening, and Validation Data

The training data were generated based on an approach of the density functional method, SIESTA version 4.0.2 [31]. SIESTA was shown to be an efficient method to optimize the electronic structure and *ab initio* molecular dynamics simulations of molecules and solids. Depending on the type of data, either non-spin- or spin-polarized was used with the generalized gradient approximation (GGA), in the Perdew-Burke-Ernzerhof (PBE) form [32]. We chose the split polarized valence double-zeta (DZP) basis set due to the trade-off between accuracy and computation expenses [134]. Note that, SIESTA projects the

electron wavefunctions and density onto a real-space grid and utilizes the non-relativistic norm-conserving Troullier-Martins pseudopotentials [34]. Intermolecular van der Waals interactions are captured by the second generation of dispersion correction (DFT-D2) by [135]. We performed an energy convergence test and selected a value of 250 eV for mesh cutoff and 300 Ry ( $\sim 4081$  eV) for energy shift. In the monolayer setting, the interactions between monolayers (or molecules) were inhibited by a 20 Å vacuum layer. Theoretically, this should not cause any difference, but in the real-space projection, the vacuum layer size can burden and significantly decelerate the calculation time. A monolayer thickness of 7.726 Å was used to calculate per-area quantities for monolayer MoSe<sub>2</sub> (e.g., monolayer stresses) [47], and 7.726 Å for monolayer MoS<sub>2</sub>. In the energetic and geometric optimizations, we applied no atomic constraints and optimized the structures until the forces acting on the atoms became lower than 0.01 eV·Å<sup>-1</sup>. In contrast, in the solid deforming or bond dissociation calculations, these constraints were put on the box or on the atoms in the dissociated pair. To achieve accurate electronic structure calculations, we allowed a 15 Å cutoff for the set of k-points in the first Brillouin zone. However, Moreno and Soler [35] showed that the resultant k-grids would be chosen in an optimal way, based on a method utilizing an effective supercell close to spherical shape. This approach can thus minimize the number of k-points for a given precision. The self-consistent and the conjugate gradient minimization schemes were employed for the electronic-structure calculation and for the geometry optimization, respectively.

The cohesive energies, the surfaces (edges) and vacancy formation energies, and the stress components were calculated with the same method in a previous study [47]. Forces, however, were sampled at the atoms in selected pairs only. We chose the bonds that broke first when Se, S, and Mo molecules were annealed to a high temperature. This selection implies a proximity to a realistic PES where the atoms hop over the lowest energy barrier.

### 5.3. Molecular Dynamics (MD) Simulations

The Large-scale Atomic/Molecular Massively Parallel Simulator, or LAMMPS [136], was used for atomistic simulations in the three steps mentioned above. To compare MD simulations with *ab initio* calculations, we used the same atomic systems for most objectives except for the lattice structures and

cohesive energies, in which we enlarged the size of the system for better sampling. For energy landscapes (equation of states, bond dissociation, phase transition, and dissociation of Se clusters), single point calculations were performed on the equilibrated structures from *ab initio* calculations without energy minimization. For the remaining objectives, an energy minimization step was carried out on the input structures with the conjugate gradient algorithm (energy tolerance 0 eV, force tolerance  $10^{-10}$  eV·Å<sup>-1</sup>) before calculating the energies. For simulations with MD steps, a time step of 1 fs was used. In the fracture simulations, a monolayer MoSe<sub>2</sub> or MoS<sub>2</sub> flake of a chosen domain size was first optimized and equilibrated with an NPT ensemble for 0.1 ns, followed by a deforming step at a strain rate  $10^8$  s<sup>-1</sup>. However, when crack was about to propagate, we set the rate to be  $5 \times 10^6$  s<sup>-1</sup>. Atomic visualizations were created with OVITO [42].

#### 5.4. Potential Optimization Framework

We obtained the Tersoff potential parameters for this work using an optimizing scheme presented in [47]. Overall parametrization includes a few iterations, each of which comprises three steps: training, screening, and evaluation. The potential is first optimized against *ab initio* data with a multi-objective genetic algorithm (NSGA-III) for a selected group of properties in the training step. Next, the optimized parameters are screened, considering other properties that might benefit the targeted properties, i.e., fracture energy and bond-changing response in this study. In this version of optimizing framework, we introduce a local optimizing algorithm (Bound Optimization BY Quadratic Approximation, or BOBYQA [137]) during the screening step to stabilize the results. At the end of this step, we prescribe a combination of maximum percentage errors to identify promising candidates, in which a smaller percentage is given to the criterion that is directly related to the fracture behavior, e.g., bond dissociating energy and force, surface energy, and phase transformation landscape. In the evaluation step, we test the performance of a few selected sets of parameters on the fracture-related behaviors of structures within two- to ten-nanometer size and compare them to the experimental results (or large-scale first-principle results if available). If such validating sources are absent, a few properties that physically correlate to the desired properties the most will be evaluated instead. In addition, an optional test for transferability can also be

performed to evaluate the capability of the potential in other scenarios. After each iteration, we evaluate the relation of the involved properties using a normalized covariance matrix and principal component analysis. This serves to instruct the selection of training and screening properties for the next iteration and may include regrouping, adding, and eliminating of these properties to better optimize the targeted behaviors. In addition, this can be used as an estimation for the capability of a chosen potential in correctly capture the desired behaviors.

Following the previous study, we chose a population size of 168 for this work [43]. Ten replicas with different random generator seeds were created, each of which was run for 500 generations. This number of generations was shown to be adequate for the NSGA-III to converge [47]. For crossover, a simulated binary operator was used with a crossover probability of 1 and a crowding degree  $\eta$  of 30. For mutation, we used a polynomial operation with a mutation probability of 1 and a  $\eta$  value of 20. The statistics of each replica were output after a number of generations (20 in this study) to monitor the optimization progress. At the end, we combined the optimized parameters from all replicas for the local optimization process and the screening step. We used Python (3.7.7) and the Distributed Evolutionary Algorithms in Python (DEAP) package to run the genetic algorithm [44]. The local optimizer was, however, implemented based on the Python Parallel Global Multiobjective Optimizer [138] (PyGMO) package. SCOOP (0.7.1.1) [45] was used to distribute the workers for parallel programming.

### 5.5. Calculation of Atomic Strain and the J-integral from HRTEM Images

The atomic strain calculation is based on the structural-template-matching Python codes on Github developed by Jacob Madsen and Jacob Schitz [118]. The input HRTEM image is divided into multiple segments, each of which contains several atoms/lattice fringes that forms a "unit cell" for the HRTEM image. A template is then defined according to the configuration of the segments as well as the lattice constants of the material such that it corresponds to a segment under zero strain condition. For the HRTEM images herein, the segment and template are defined as a hexagon plus its geometric center (7 points in total). Both the segments and template need to have the correct magnitudes for the calculation of strain. The real magnitude of the segments is computed from the scale ( $\text{nm}\cdot\text{pixel}^{-1}$ ) that is embedded

in the HRTEM images, and the magnitude of the template is defined according to selected area diffraction of the suspended monolayer MoSe<sub>2</sub> flakes. The code identifies the affine transformation matrix from the template to each segment, from which the deformation gradient  $\mathbf{F}$  for each segment can be computed. Since we cannot extract atomic positions along the beam direction from the HRTEM images,  $\mathbf{F}$  has a shape of 2x2. From  $\mathbf{F}$ , the Green-Lagrangian (G-L) strain tensor  $\mathbf{E}$  is computed as follows:

$$\mathbf{E} = \frac{1}{2}(\mathbf{F}^T \mathbf{F} - \mathbf{I}) \quad (5.1)$$

where  $\mathbf{I}$  is the identity matrix. We used G-L strain tensor due to the large magnitude of strain ( 10% ) observed in the HRTEM images at the crack tip.

J-integral, as originally proposed by James Rice, is formulated as a line integral around the crack tip [133]. Herein, we adopted the area integral method developed by Li et al [132], which is shown to produce smaller error than the line integral method for the calculation of energy release rate from finite element simulations. The area integral form of the J-integral is as follows:

$$J = \iint_{A_C} [\sigma_{ij} \frac{\partial u_i}{\partial x_1} - W \delta_{1j}] \frac{\partial q}{\partial x_j} dA, i, j \in [1, 2] \quad (5.2)$$

where  $A_C$  is an area enclosed by  $C_0$  and  $C_1$ , two paths that surround the crack tip, as shown in Fig. 5.1,  $\sigma_{ij}$  is the component of the Cauchy stress tensor,  $u_i$  is the displacement along the  $i$ -direction,  $x$  represents the deformed configuration (i.e., spatial coordinates),  $W$  is the strain energy density,  $\delta_{1j}$  is the Kronecker-delta,  $q$  is a sufficiently smooth function in  $A_C$  that is one and zero on  $C_0$  and  $C_1$ , respectively. The discretized form of equation 5.2 is:

$$J = \sum_k \left[ \sigma_{ij}^k \frac{\partial u_i^k}{\partial x_1} - W^k \delta_{1j} \right] \frac{\partial q^k}{\partial x_i} da^k, i, j \in [1, 2] \quad (5.3)$$

where the summation loops through all the pixels in  $A_C$ .  $a^k$  is the area of each pixel. We first compute the 2<sup>nd</sup> Piola-Kirchhoff stress tensor  $\Sigma$  from  $\mathbf{E}$  using the following equation:

$$\Sigma_I = C_{IJ} e_J + \frac{1}{2!} C_{IJK} e_J e_K, I, J, K \in [1, 6] \quad (5.4)$$

where  $I, J$ , and  $K$  are Voigt indices such that  $1(I) = 11(ij), 2 = 22, 3 = 33, 4 = 23, 5 = 13$ , and  $6 = 12$ . Equation 5.4 approximates the constitutive equations for transition metal dichalcogenides up to the third order elastic constants. The elastic constants were computed by fitting equation 5.4 to *ab initio* uniaxial stress-strain curves along the armchair and zigzag direction. Fig. 5.2 compares *ab initio* 2<sup>nd</sup> Piola-Kirchhoff stress- G-L strain curves to the fitted curves using equation 5.4 for monolayer MoSe<sub>2</sub>. Elastic constants up to third order provide acceptable accuracy for the quantification of stress. The fitted elastic constants are summarized in Table 5.1.

Table 5.1. Fitted elastic constants from *ab initio* uniaxial tension simulations

MoS <sub>2</sub>		MoSe <sub>2</sub>	
2nd order elastic constants (GPa)	3rd order elastic constants (GPa)	2nd order elastic constants (GPa)	3rd order elastic constants (GPa)
$C_{11} = 122.3395$	$C_{111} = -610.1409$	$C_{11} = 112.6172$	$C_{111} = -465.7352$
$C_{12} = 47.4595$	$C_{112} = -3.5008$	$C_{12} = 49.2313$	$C_{112} = -11.336$
$C_{22} = C_{11}$	$C_{222} = -471.5260$	$C_{22} = C_{11}$	$C_{222} = -359.1101$
$C_{66} = 1/2 \times (C_{11} - C_{12})$	$C_{122} = C_{111} + C_{112} - C_{222}$	$C_{66} = 1/2 \times (C_{11} - C_{12})$	$C_{111} + C_{112} - C_{222}$
	$C_{166} = 1/4 \times (3 \times C_{222} - 2 \times C_{111} - C_{112})$		$C_{166} = 1/4 \times (3 \times C_{222} - 2 \times C_{111} - C_{112})$
	$C_{266} = 1/4 \times (2 \times C_{111} - C_{222} - C_{112})$		$C_{266} = 1/4 \times (2 \times C_{111} - C_{222} - C_{112})$

The Cauchy stress tensor is computed as follows:

$$\boldsymbol{\sigma} = \frac{1}{\det(\mathbf{F})} \mathbf{F} \boldsymbol{\Sigma} \mathbf{F}^T \quad (5.5)$$

where  $\det(\mathbf{F})$  represents the determinant of matrix  $\mathbf{F}$ .  $\frac{\partial u_i}{\partial x_i}$  is computed from  $\mathbf{F}$  :

$$\frac{\partial u_i}{\partial x_i} = \delta_{ij} - F_{ij}^{-1}, i, j \in [1, 2] \quad (5.6)$$

where  $\mathbf{F}_{ij}^{-1}$  represents the  $i, j$  th component of the inverse of the matrix  $\mathbf{F}$ .  $W$  is computed from the G-L strain tensor  $\mathbf{E}$  :

$$W = \frac{1}{2!} C_{IJe_Ie_J} + \frac{1}{3!} C_{IJK} e_I e_J e_K, I, J, K \in [1, 6] \quad (5.7)$$

The corresponding variables were first computed for each segment, and then converted to spatially-resolved grids (in pixels) with the grid data function of Scipy. A cubic interpolation method is used.  $\frac{\partial q^k}{\partial x_i}$  is defined as follows:

$$\frac{\partial q^k}{\partial x_i} = \frac{\partial q^k}{\partial p_j} \frac{dp_j}{dx_i} \quad (5.8)$$

where  $\mathbf{p}$  is the coordinate in pixel,  $\frac{dp_j}{dx_i}$  is the inverse of the scale and has a unit of pixel-nm<sup>-1</sup>. We define  $\mathbf{q}(\mathbf{p})$  as a monotonically decreasing function that is one at the inner boundary and vanishes contour-wise to zero at the outer boundary.  $\frac{\partial q^k}{\partial p_i}$  is computed by numerical differentiation, and its values at the boundary are smoothed to adjacent non-zero values. Fig. 5.1(b) shows an example  $\frac{\partial q}{\partial x_1}$  function.

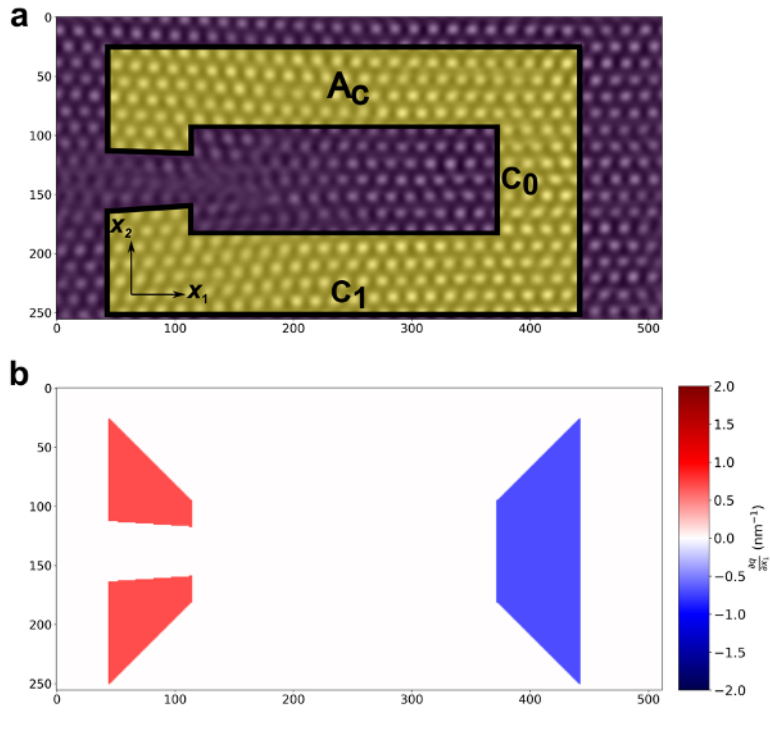


Figure 5.1. (a) Definition of the area for the computation of J-integral. (b)  $\frac{\partial q}{\partial x_1}$  for the corresponding area in (a).

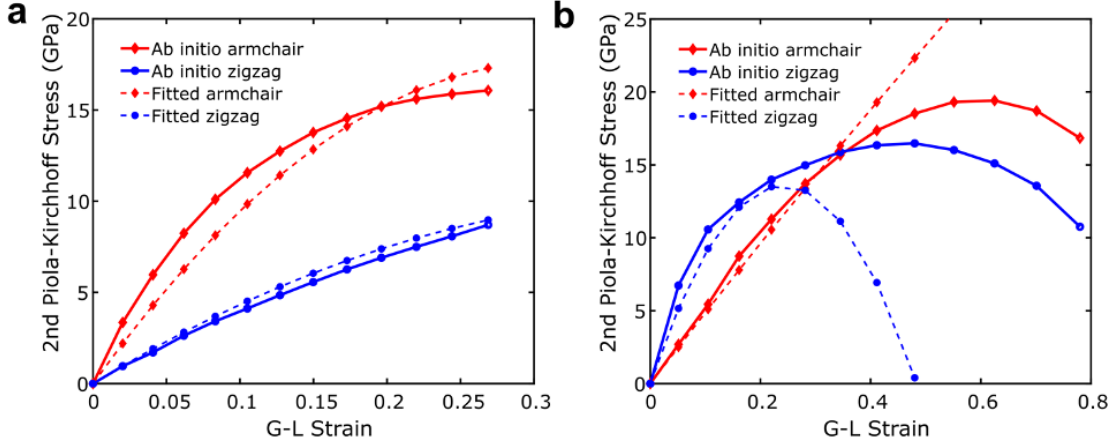


Figure 5.2. Comparison between *ab initio* and fitted Green-Lagrangian strain-2<sup>nd</sup> Piola-Kirchhoff stress for uniaxial tension along the armchair (a) and zigzag (b) direction.

### 5.6. Atomistic-to-continuum Mapping of the Displacement, Stress, and Strain Field

While the calculation of J-integral follows the same procedure in the experiment, the displacement, stress, and strain fields are mapped differently. Atomistic simulations possess some advantages over microscopic images, such as the exact position of atoms and their displacement relatively to the referenced coordinates are well defined. In addition, useful quantities like per-atom stresses and energy density can be easily output. However, thermal noises introduce oscillation into these fields and the simulation of the exact domain sizes and boundary conditions is discouraged by the computational expenses. On top of these issues, the discrete nature of the atoms requires a rigorous mapping scheme. Therefore, we used an atomistic-to-continuum mapping scheme by Jones and Zimmerman [139]. Each per-atom quantities will be evaluated based on a kernel function that satisfies following requirements:

$$\psi > 0; \int_{\Omega} \psi dV = 1 \quad (5.9)$$

For two-dimensional (2D) materials, we employ a cylindrical kernel instead of a spherical one. The z-thickness of the cylinder equals to the interlayer distance between monolayers ( 7.75 Å ). This quantity, however, only serves to ensure the consistency between stresses components in a monolayer and their 3D counterparts.

$$\psi = \frac{20}{6\pi R_c^2 t} \left[ 1 - 3 \left( \frac{r}{R_c} \right)^2 + 2 \left( \frac{r}{R_c} \right)^3 \right] \quad (5.10)$$

Where  $R_c$  is the averaging radius and  $t$  is the monolayer thickness. Note that, strains components will be calculated from the displacement field, and they should be estimated at the same spatial position with the stresses components in the J formulation. The grid points to map the displacement field (and the  $q$ -field) are therefore different from the ones used to map the stresses field. We borrowed a concept from finite element method (FEM) and placed the displacementfield grid points at the nodes of triangulation generated by the Python meshzoo package and the stress-field grid points located at the quadrature point associated with each element. The use of FE shape functions also facilitates the calculation of derivative terms [140]. A continuum quantity is then calculated from:

$$W(\mathbf{X}, t) = \Sigma_{\alpha} (\phi^{\alpha}(t) - \phi_X^{\alpha}) \psi(\mathbf{X} - \mathbf{X}^{\alpha}) \quad (5.11)$$

Where  $\alpha$  is the total number of atoms in the averaging horizon.  $\phi$  can represent displacements components, stresses components, energy density or  $q$ -value and  $W$  is the corresponding continuum quantity.

The field value at position different from the grid points is interpolated by shape functions  $\mathbf{N}$  and their gradients:

$$u(\mathbf{X}, t) = \sum_i N_i(\mathbf{X}, t) u_i; \nabla u(\mathbf{X}, t) = \sum_i \nabla N_i(\mathbf{X}, t) u_i \quad (5.12)$$

Where  $N_i$  's are the shape functions and  $u_i$  are the field value at vertex  $i$ . The stress term is extracted from interatomic interactions by [136] :

$$\begin{aligned}
\sigma_{ab} = & \frac{1}{2} \sum_{n=1}^{N_p} (r_{1_a} F_{1_b} + r_{2_a} F_{2_b}) + \frac{1}{2} \sum_{n=1}^{N_b} (r_{1_a} F_{1_b} + r_{2_a} F_{2_b}) + \frac{1}{3} \sum_{n=1}^{N_a} (r_{1_a} F_{1_b} + r_{2_a} F_{2_b} + \\
& r_{3_a} F_{3_b}) + \frac{1}{4} \sum_{n=1}^{N_d} (r_{1_a} F_{1_b} + r_{2_a} F_{2_b} + r_{3_a} F_{3_b} + r_{4_a} F_{4_b}) + \frac{1}{4} \sum_{n=1}^{N_i} (r_{1_a} F_{1_b} + r_{2_a} F_{2_b} + r_{3_a} F_{3_b} + \\
& r_{4_a} F_{4_b}) + \sum_{n=1}^{N_f} r_{i_a} F_{i_b}
\end{aligned} \quad (5.13)$$

To alleviate the noise from thermal oscillation, we perform the mapping on the time averaged snapshot of the simulations. Each snapshot is therefore a smear of 1000 frames. The benchmark examples of this mapping scheme were presented in Fig. 5.3.

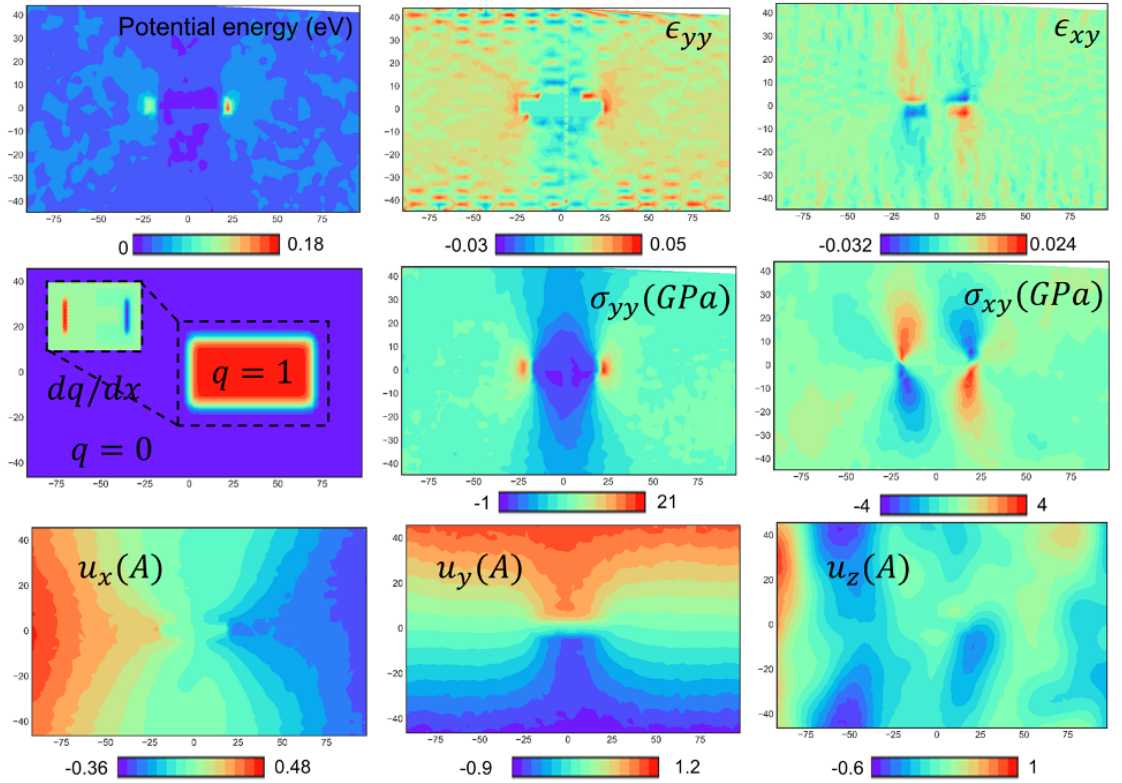


Figure 5.3. The continuum stress, strain, and displacement fields mapped from the discrete atoms.

## 5.7. Indirect *In Situ* High-resolution Transmission Electron Microscopy (HRTEM)

### Fracture Tests

The indirect fracture tests were conducted in HRTEM (FEI Titan 80-300 TEM with an image corrector to reduce both the chromatic and spherical aberrations) using electron beam irradiation for the initiation and stable propagation of cracks. Monolayer MoS<sub>2</sub> and MoSe<sub>2</sub> flakes (Fig. 5.4(a) and Fig. 5.4(b)) synthesized by chemical vapor deposition were transferred to holey Si<sub>3</sub>N<sub>4</sub> TEM grids to form suspended membranes. To generate a dominating crack, the suspended monolayer flakes were irradiated by focused electron beam under 200 kV acceleration voltage for  $\sim 1$ -2 mins. The electron beam was tuned into a narrow slit (width  $< 5$  nm) along the zigzag direction of the suspended monolayer (Fig. 5.4(c)). The initial crack propagated spontaneously due to relaxation of the pre-stress within the flake, and stopped at a critical length. Subsequent stable propagation of atomically-sharp cracks was achieved by continuous electron beam irradiation at the crack tip with a dose rate of  $\sim 2.5 \times 10^7 e^- \cdot \text{nm}^{-2} \cdot \text{s}^{-1}$ , resulting in a crack propagation velocity of  $\sim 2.5 \text{ nm} \cdot \text{s}^{-1}$ . Continuous tracking of the crack tip as it propagated allowed us to capture high-resolution images of several crack advancement events, which were used for the fracture toughness quantification. Electron-beam induced stable crack propagation was also reported in a previous HRTEM investigation of monolayer MoS<sub>2</sub> [22], and is analogous to the irradiation-assisted stress corrosion cracking in metal alloys [141]. Several existing studies report the formation of vacancies [101, 102] and extensive defects such as vacancy clusters [142] and vacancy lines [77, 102] in TMDCs upon prolonged electron beam irradiation. In the fracture tests conducted herein, the crack propagated before any extensive defects formed.

Fig. 5.4(d) shows a typical crack path in monolayer MoSe<sub>2</sub> during the stable crack propagation stage. The HRTEM image was taken at a defocus value between  $-10 - -5$  nm, under which the propagation of crack was more easily captured due to better. The crack followed a serrated path along the zigzag direction of the suspended monolayer MoSe<sub>2</sub> due to its lower surface energy in comparison to the armchair direction [47]. We also took HRTEM images at a defocus value of  $-5 - 0$  nm under which the Mo and S/Se atoms are visible (Fig. 5.4(f)). Such an imaging condition allows direct comparison of the atomic configuration at the crack tip between experiments and MD simulations, as discussed next.

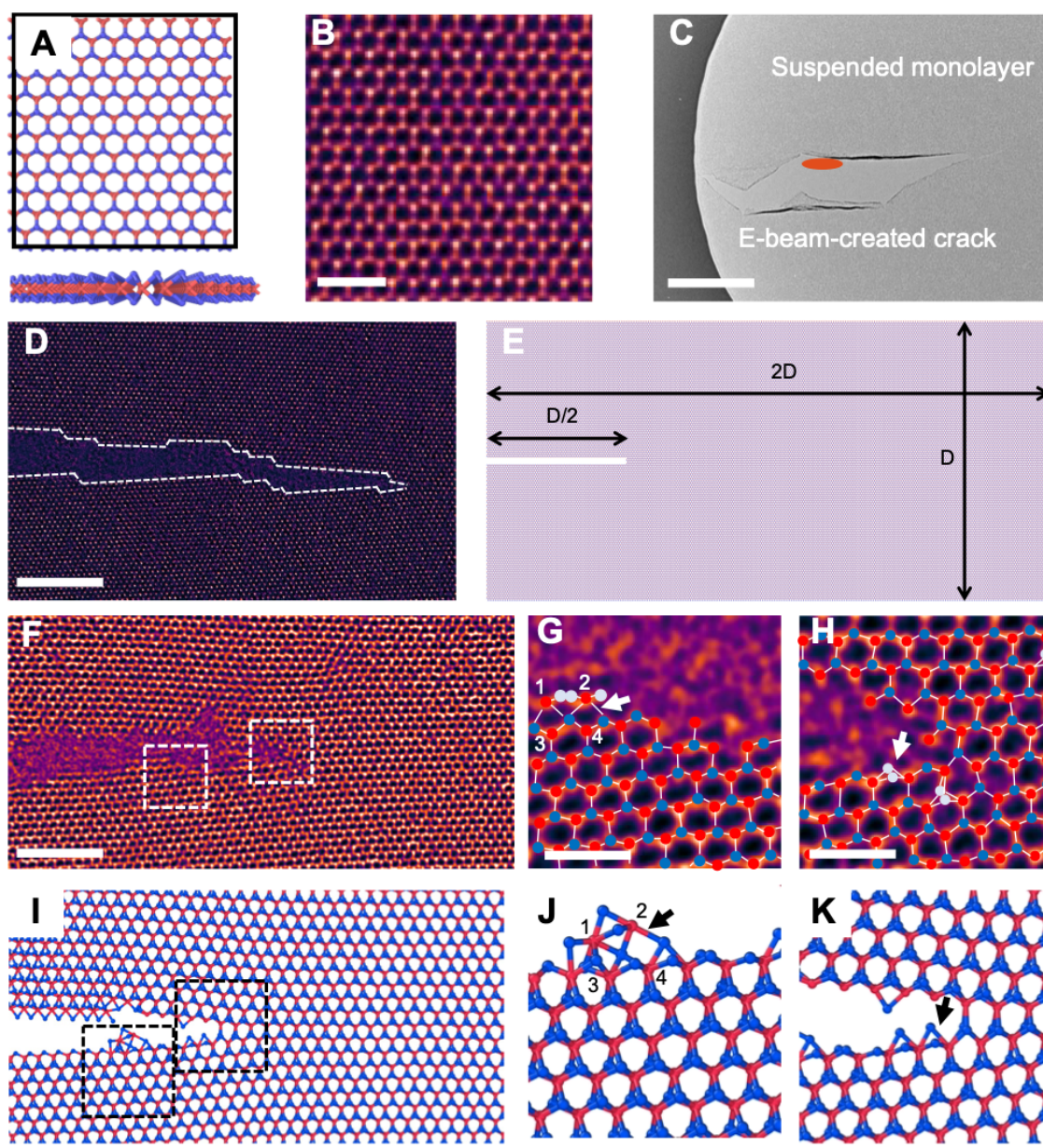


Figure 5.4. **Lattice structures, crack initiation, and atomic configurations at the crack tip.** (A) Atomic structures of monolayer MoS<sub>2</sub> and MoSe<sub>2</sub>. Red atoms are Mo, and blue atoms are S (in MoS<sub>2</sub>) or Se (in MoSe<sub>2</sub>). (B) High-resolution transmission electron microscope (HRTEM) images of pristine monolayer MoSe<sub>2</sub>. Scale bar: 1 nm. (C) A crack created in a suspended monolayer MoSe<sub>2</sub> flake by electron beam irradiation. The electron beam was tuned into a slit along the zigzag direction of the suspended monolayer, as indicated by the orange oval. Scale bar: 0.4  $\mu$ m. (D) Crack path in monolayer MoSe<sub>2</sub> under continuous electron beam irradiation. The crack followed a serrated path along the zigzag direction of the monolayer MoSe<sub>2</sub> specimen. Scale bar: 5 nm. (E) Configuration of the molecular dynamics (MD) fracture test for monolayer MoS<sub>2</sub> and MoSe<sub>2</sub>.  $D = 40$  nm. (F) HRTEM image of the crack tip in monolayer MoSe<sub>2</sub>. Scale bar: 3 nm. (G) Zoomed-in view of the left dashed rectangular region in (F). Mo atoms are colored in red, Se atoms are colored in white, and Se<sub>2</sub> columns are colored in blue. The arrow points at a reconstruction site in which the four numbered Mo atoms arrange into a rectangular lattice surrounding the center Se<sub>2</sub> column. Scale bar: 1 nm. (H) Zoomed-in view of the right dashed rectangular region in (F). The color coding is identical to (G). The arrow points at a perturbed Se<sub>2</sub> site, in which the top and bottom Se atoms with respect to the middle Mo atoms are both visible. Scale bar: 1 nm. (I) MD snapshot of the crack tip in monolayer MoSe<sub>2</sub>. (J) Zoomed-in view of the left dashed rectangular region in (I). The same lattice reconstruction in comparison to (G) was observed and highlighted. (K) Zoomed-in view of the right dashed rectangular region in (I). The same perturbed Se site in comparison to (H) was observed and highlighted. The color coding in (I-K) is identical to (A).

### 5.8. Molecular Dynamics (MD) Fracture Simulations

The MD fracture simulations for monolayer MoS<sub>2</sub> and MoSe<sub>2</sub> were conducted based on the Tersoff potential [56], which was shown to possess good accuracy and transferability for the thermal and mechanical properties of monolayer MoSe<sub>2</sub> [47]. Herein, we utilized the parametrization framework that we developed in an earlier work [47] to parametrize a Tersoff potential for monolayer MoS<sub>2</sub> and MoSe<sub>2</sub>. The parametrization process contains three steps: training, screening, and evaluation. The training step includes the application of a multi-objective genetic algorithm for the optimization of material properties, dissociation energy landscapes, and dissociation forces against *ab initio* calculations. The optimized interatomic potential parameter sets were screened for another set of properties for further enhancement of accuracy. Finally, the screened parameter sets were evaluated for properties beyond the training and screening data sets to ensure sufficient transferability. The framework was developed to obtain an overall good performance in both the equilibrium and non-equilibrium regime. In this study, however, we paid more attention to the behavior of atoms in the non-equilibrium regime than striking a balance among

all regimes. As such, we enriched the training data by i) adding reaction forces for certain dissociation energy landscapes, and ii) adding more points on the large deformation regime for both materials to prioritize the accuracy of the Tersoff potential for failure-related behaviors. The enrichment resulted in a more gradual bond dissociation process, which agreed with our experimental observations.

To simulate fracture in the suspended monolayer MoS<sub>2</sub> and MoSe<sub>2</sub>, 80x40 nm rectangular monolayers with an existing notch of 20 nm were loaded along the y-direction (Fig. 5.4(e)). The boundary conditions were free at the left and right edges and periodic at the top and bottom. Reflecting walls were placed at the distance of 20 Å away from the monolayer to prevent the curl-up of the free edges. In the experiment, the monolayers were not completely free but restrained by adhesion with the TEM grids. The loading process was applied to a point close to failure and then decelerated to avoid the interference of surface wave generated by the bond breakage when the potential energy is released.

### 5.9. Atomic Configuration at the Crack Tip

Fig. 5.4(f) and 5.4(i) show the atomic configuration of monolayer MoSe<sub>2</sub> at the crack tip, observed in the HRTEM and MD fracture tests, respectively. In Fig. 5.4(f), Mo atoms are not readily distinguishable from S/Se atoms given their similar contrast. Following the protocol developed by Wang et al [22], we determined Se atoms according to the higher density of Se and Se<sub>2</sub> vacancies in comparison to Mo vacancies in the monolayer MoSe<sub>2</sub> flake. Consistent with experimental observation, the crack in the MD simulations followed the zigzag direction and underwent mild deflection (Fig. 5.4(i)). Some unique atomic configurations were identified in both the HRTEM image and MD snapshot. In Fig. 5.4(g) and 5.4(j), the four Mo atoms at the crack edge rearranged into a rectangular shape, and the Se atoms at the center of the rectangle had a coordination number of 4 instead of 3. Such a configuration resembles the inversion domain formed in monolayer MoSe<sub>2</sub> as a result of thermal annealing and electron beam irradiation [92]. In Fig. 5.4(h) and 5.4(k), Se atoms above and below the middle Mo layer were both visible. For MD simulations, this is the outcome of the enrichment of the training data, which provides an intermediate energy state during bond dissociation. Similarities in the crack tip atomic configurations were also observed for monolayer MoS<sub>2</sub>, and confirmed validity of the parametrized interatomic potentials.

The qualitative agreements between HRTEM images and MD snapshots highlight good accuracy of the parametrized Tersoff potential.

### 5.10. Fracture Toughness Quantification

Unlike standard fracture tests [143, 144], the indirect *in situ* fracture tests cannot provide force-displacement curves that are used for the quantification of fracture toughness. We instead utilized the J-integral approach [133, 145]. J-integral is formulated as a path-independent integral that gives the strain energy release rate of the material. For brittle materials, the integral, calculated right before crack propagation, equals the fracture toughness evaluated from linear elastic fracture mechanics (LEFM). Fig. 5.5(a) shows such a moment captured in monolayer MoSe<sub>2</sub> after which the crack tip propagated by 5 nm in 2 seconds (Fig. 5.5(b)). Fig. 5.5(c) shows the onset of crack propagation in the MD fracture tests. The protocol for calculating the J-integral is slightly different for the HRTEM and MD snapshots. Briefly, we extracted the atomic strain (Green-Lagrangian strain  $E_{xx}$ ,  $E_{yy}$ , and  $E_{xy}$ ) from the HRTEM images based on the structural template matching method developed by Madsen et al.[118], and computed the corresponding Cauchy stress ( $\sigma_{xx}$ ,  $\sigma_{yy}$ , and  $\sigma_{xy}$ ) using elastic constants (up to third orders) derived from first-principle calculations. The extrapolated pixel-wise  $E_{yy}$ ,  $E_{xy}$ ,  $\sigma_{yy}$  and  $\sigma_{xy}$  values for Fig. 5.5(a) are shown in Fig. 5.5(d), 5.5(e), 5.5(k), and 5.5(l), respectively. For the MD simulations, we first mapped the displacement field from atomic positions (Fig. 5.5(f)) using a cylindrical kernel function (with an averaging radius of 3 Å) and calculated the strain field based on a numerical gradient approximation. The stress field is mapped independently based on the per-atom virial stress output [136] (Fig. 5.5(i) and 5.5(j)). We note that this stress only carries an approximated meaning in the case of many-body interatomic potentials like Tersoff. This stems from the equal distribution of many-body terms among the contributing atoms, leading to a non-conserving field [146]. To achieve a more accurate mapping, central constraints must be applied. However, the approximation was shown to achieve a stress value within 5% of the exact value [147].

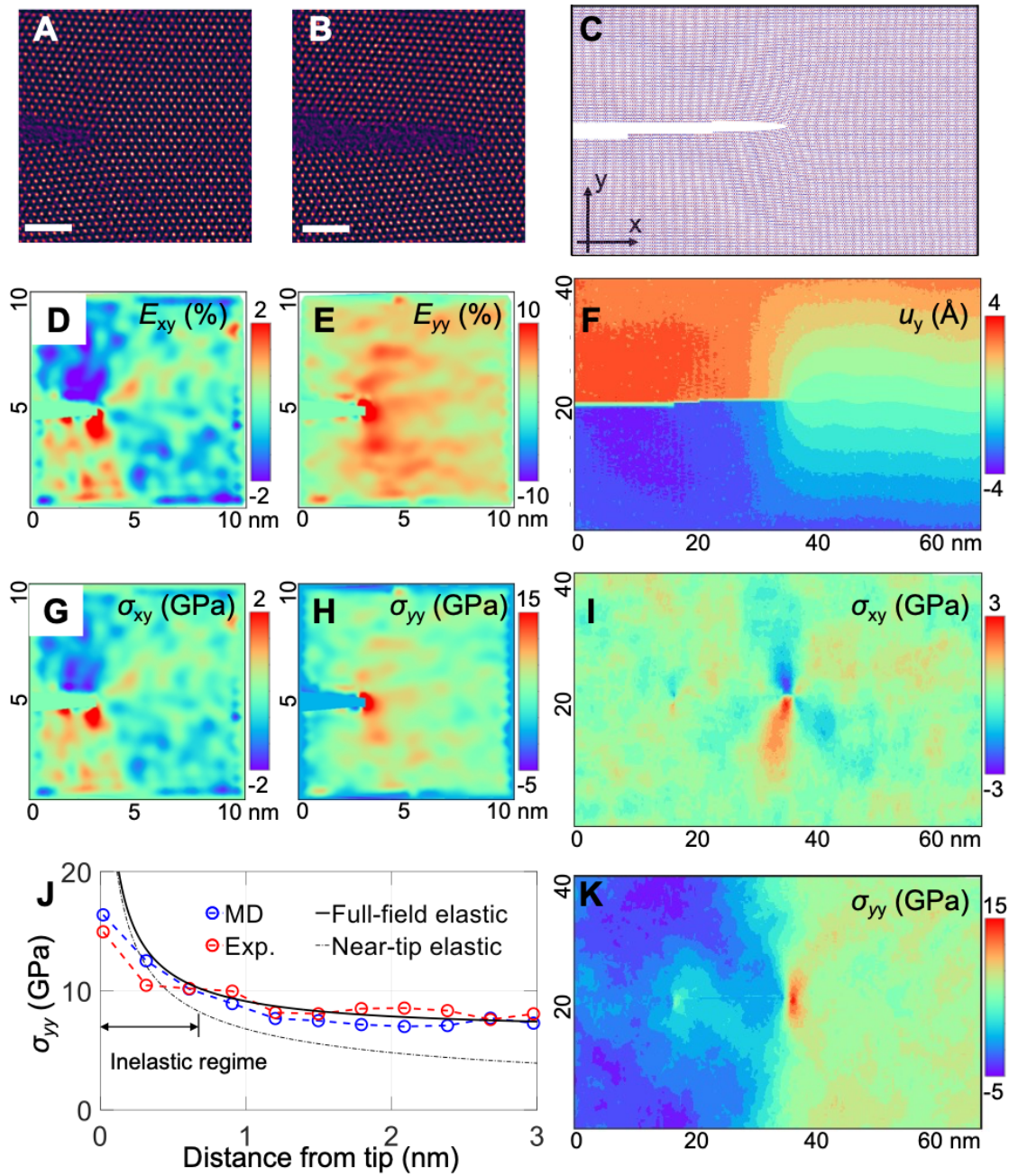


Figure 5.5. **Atomic strain and stress field near the crack tip.** (A-B) Crack tip configuration at the onset (A) and after (B) crack propagation. Scale bar: 2 nm. (C) Onset of crack propagation in MD fracture tests. (D-E) Green-Lagrangian strain field  $E_{xy}$  (D) and  $E_{yy}$  (E) for (A). (F) Displacement field  $\mu_y$  for (C). (G-H) Cauchy stress  $\sigma_{xy}$  and  $\sigma_{yy}$  for (A). (I) Cauchy stress  $\sigma_{xy}$  for (C). (J) Cauchy stress  $\sigma_{yy}$  in front of the crack tip of monolayer MoSe<sub>2</sub> for MD and experiments in comparison to predictions from the  $K_I$  field (near-tip elastic) and accurate solutions from linear elasticity (full-field elastic). Inelastic regime corresponds to the fracture process zone. (K) Cauchy stress  $\sigma_{yy}$  for (C).

The stress field  $\sigma_{xy}$  and  $\sigma_{yy}$  for monolayer MoSe<sub>2</sub> at the onset of crack propagation, obtained from MD simulations and fracture experiments, are shown in Fig. 5.5(g), 5.5(i) and Fig. 5.5(h), 5.5(k), respectively. Qualitative agreements of the stress fields were observed between MD simulations and fracture experiments, which confirmed that the electron beam irradiation induced a mode I load to the suspended sample. These fields show stress concentration and relaxation ahead and behind the crack tip with some oscillations, though the distinction between these two areas are less recognizable in the experimental image. Several factors are found to introduce noise in the experimental strain measurement, including thermal vibration of atoms, defocus, unwanted sample tilt, and instrumental noise [118]. Thermal vibration and instrumental noises can be reduced by image overlay and image filtering (3-4 images were overlaid and processed by a Wiener filter prior to strain measurement), whereas noise introduced by defocus and unwanted sample tilt was not directly removed/minimized and thus should be the dominant source of noise. Plotting  $\sigma_{yy}$  along the x-direction as a function of the distance from the crack tip (Fig. 5.5j) revealed that the stress followed linear elastic fracture mechanics (LEFM) formulation, with a far-field stress of  $\sim 7.5$  GPa at the time of propagation. The far-field stress cannot be captured by the K-field approximation (near-tip elastic in Fig. 5.5(j)), and the more accurate solution was needed (full-field elastic in Fig. 5.5(j)). There existed an inelastic region upon which  $\sigma_{yy}$  deviated from the linear assumption, whose length can be considered as the width of fracture process zone. The existence of this zone also suggested that the use of the J-integral would be inevitable, and this value should deviate from the one calculated from the LEFM assumption.

According to the Griffith's criterion, the fracture toughness of monolayer MoSe<sub>2</sub> is  $2\gamma = 3.1N \cdot m^{-1}$  where  $\gamma$  is the zigzag surface energy of MoSe<sub>2</sub>. Such a value assumes that the material is brittle and is linearly elastic, which is valid for monolayer MoSe<sub>2</sub> according to uniaxial tension tests [109]. The critical

energy release rate  $J_c$ , calculated from the HRTEM images (averaged over 3 cases) and MD simulations, is  $3.57 \pm 0.23$  and  $3.18 \pm 0.27 \text{ N} \cdot \text{m}^{-1}$ , respectively. For monolayer  $\text{MoS}_2$ , the fracture toughness from the Griffith's criterion, HRTEM images, and MD simulations are 3.43,  $3.92 \pm 0.07$ , and  $3.37 \pm 0.23 \text{ N} \cdot \text{m}^{-1}$ , respectively. To the best of our knowledge, we report the first fracture toughness measurement for monolayer  $\text{MoS}_2$  and  $\text{MoSe}_2$  with both computational and experimental techniques, which are in good agreement with theoretical predictions for pristine  $\text{MoS}_2$  and  $\text{MoSe}_2$ . The consistency was achieved by i) atomic strain quantification in the pristine materials enabled by HRTEM characterizations, and ii) well-parametrized interatomic potentials with enrichment in large-deformation regime on top of high precision in the equilibrium regime. Those results confirm that monolayer  $\text{MoS}_2$  and  $\text{MoSe}_2$  are intrinsically brittle materials.

Fig. 5.6 shows the fracture toughness of monolayer  $\text{MoS}_2$  and  $\text{MoSe}_2$  measured herein, as well as existing results for monolayer graphene [131] and h-BN [130]. The experimental measurements for monolayer graphene and h-BN, with an *in situ* SEM setup, are both higher than their corresponding theoretical values for pristine materials. While such enhancements were explained via reasonable hypotheses and validated by MD simulations, the resolution of SEM limits examination of other possibilities that may also increase the fracture toughness. For instance, a blunted crack tip, in the radius of few nanometers, can reduce the stress concentration [148] and lead to an apparent higher fracture toughness if such an effect is not accounted for in the calculation of fracture toughness. Polymer residues from the transfer process, even atomically thin, may enhance the fracture toughness of the 2D materials through an extrinsic crack-bridging mechanism [149, 150]. HRTEM characterizations allow confirmation of the pristine condition of the local crack tip region, and enable not only accurate measurement of the intrinsic fracture properties of the material but also quantitative validation for the parametrized interatomic potentials.

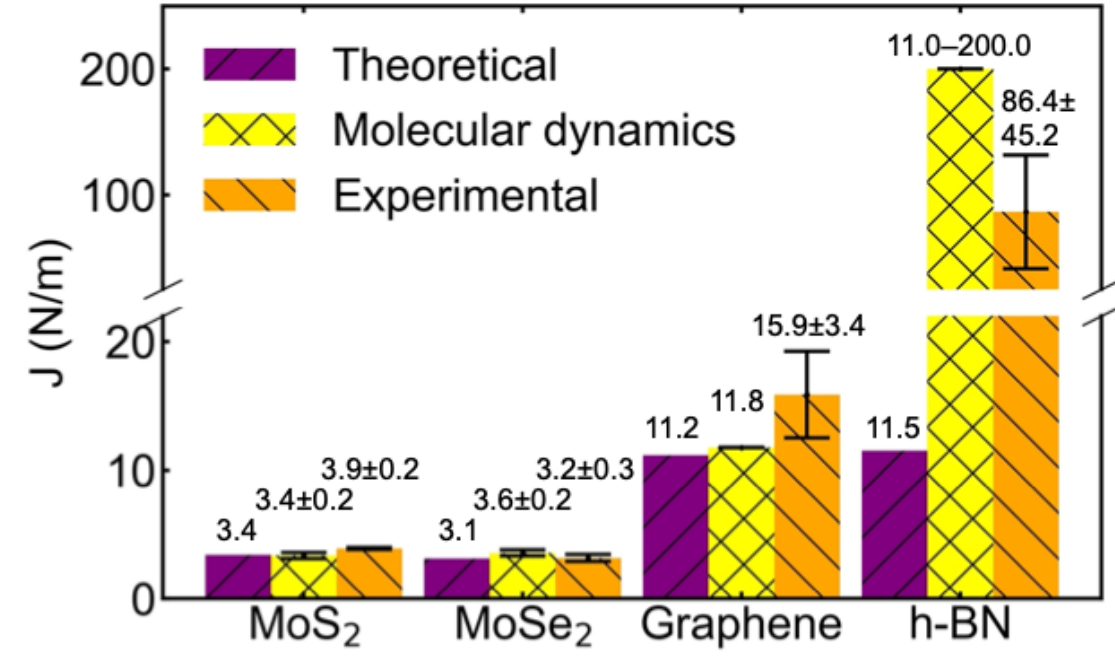


Figure 5.6. **Fracture toughness measurements of various two-dimensional materials.** Data source: MoS<sub>2</sub> and MoSe<sub>2</sub>: this study; Graphene, Zhang et al. [131]; h-BN: Yang et al. [130] In Yang et al., a range of fracture toughness for monolayer h-BN was predicted from MD simulations; the maximum value was plotted.

We envision the integrated experimental/computational framework to be applicable to most pristine 2D materials beyond the TMDC family. As shown in Fig. 5.7, the experimental setup requires the 2D samples to be transferred and suspended over holey TEM grids, which can be achieved through solution-based methods [151], dry-transfer techniques [152], and polymer-assisted wet transfer methods [29, 30, 142] depending on how the 2D materials are synthesized. A similar experiment was conducted in monolayer and bilayer ReS<sub>2</sub>. Both crack healing and crack propagation were observed under scanning TEM (STEM), and the stress field around the atomically sharp tip in monolayer ReS<sub>2</sub> was found to follow the LEFM solution [129]. The parametrization framework was shown to be applicable to the Buckingham, Stillinger-Weber, and Tersoff potential [47], which cover the first or second choice for a variety of 2D materials. Combining the experimental and computational explorations enable two more

ways to validate the interatomic potential: qualitative examination of the atomic configurations at the crack tip and quantitative assessment on the fracture toughness.

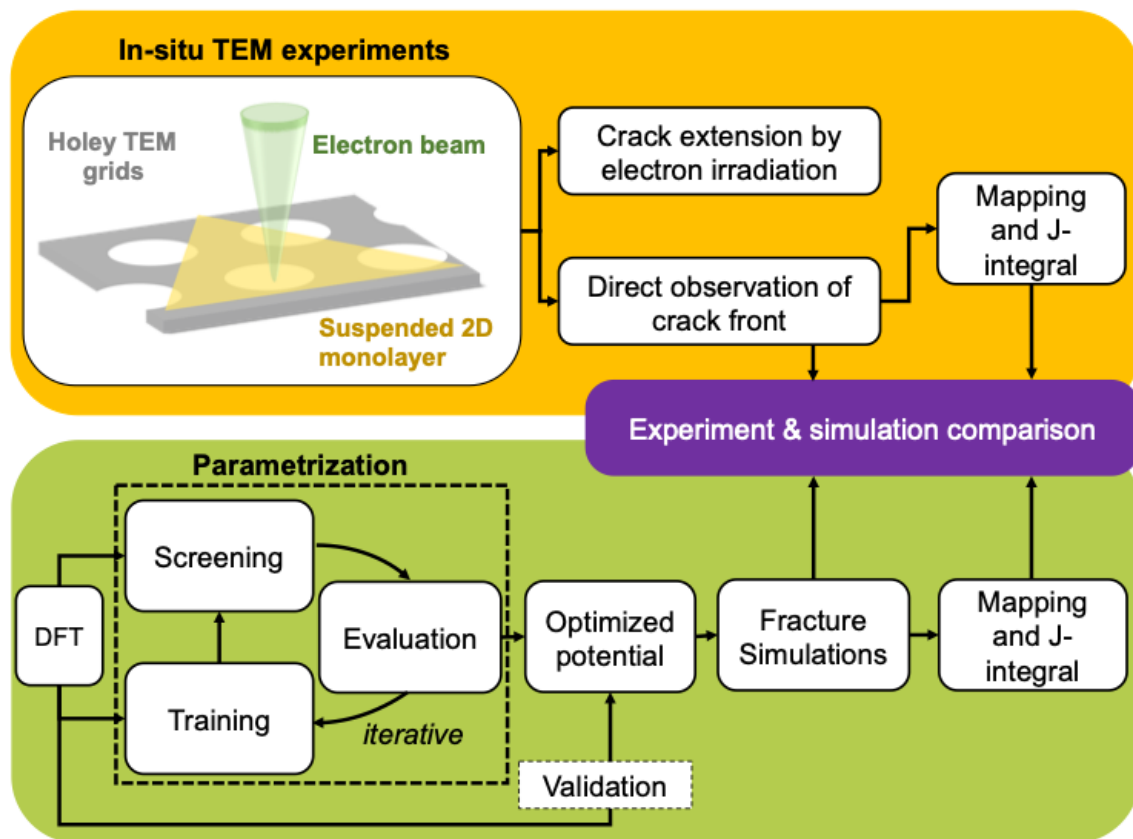


Figure 5.7. Integrated experimental/computational framework to explore the intrinsic fracture properties of 2D materials.

### 5.11. Chapter Summary

Using an integrated framework combining high-resolution transmission electron microscopy (HRTEM) and a general potential-parameterizing framework that can optimally capture the bond dissociation behavior, we report the first accurate measurement of the intrinsic fracture properties of pristine monolayer MoSe<sub>2</sub> and MoS<sub>2</sub> that agree with the Griffith criterion. The measurement is achieved via strain and stress mapping in the vicinity of the crack tip, and confirms the brittle nature of the two materials. Qualitative and quantitative agreements between HRTEM observations and MD simulations were achieved through

parametrization of the Tersoff potentials that prioritize accuracy at large deformation pathways. We anticipate the approach herein as a universal method for the fracture toughness quantification of other two-dimensional materials, especially the emerging ones.

## CHAPTER 6

***In Situ* Fracture Test of 2D MoSe<sub>2</sub>/Polymer****6.1. Introduction**

Since the discovery of graphene, numerous two-dimensional (2D) materials have been discovered and considered as promising candidates for various applications including energy-harvesting devices, batteries [153], sensors [154], and transistors [155] etc. Most of the unprecedented properties of 2D materials, e.g., electronic transport [156], modulus, and strength [157], arise from their atomically thin structure. However, such a constraint in size also makes them more prone to failure. Indeed, several 2D materials are shown to be intrinsically brittle [109, 131]. Alleviating the brittle nature of 2D materials is an indispensable step toward reliable long-term applications.

To alleviate the brittle nature of 2D materials, several toughening strategies have been proposed and investigated. Conceptually, they can be classified into extrinsic or intrinsic approaches. Intrinsic toughening utilizes atomic defects or structural transitions within the 2D materials as means of dissipating the strain energy. For instance, graphene oxide, an oxidized variant of graphene with interspersed oxygen-containing functional groups, possesses an epoxide-to-ether transition upon tensile loading that enhances the toughness by 100% in comparison to a hydroxylated graphene oxide [158]. In monolayer MoS<sub>2</sub> and MoSe<sub>2</sub>, S and Se vacancies can blunt the crack tip and agglomerate into vacancy lines that lead to 28% increase in energy release rate [22]. Monolayer h-BN contains an asymmetric zigzag crack edge that introduces crack bifurcation during mode I loading, resulting in a maximum of 16 fold increase of the energy release rate. On the other hand, extrinsic toughening utilizes an adsorbed or chemically bonded second material that bridges the propagating crack through strong interfacial interactions. Carbon nanotubes covalently bonded to graphene was found to increase the energy release rate by 360% [159]. An ultrathin (1.55-4.45 nm) polymer adlayer which interacts with GO through van Der Waals

interactions and hydrogen bonding, was shown to increase the energy release rate of graphene oxide by a maximum of 310% [149, 150]. While those studies have successfully shown the intrinsic and extrinsic toughening effects, they are either indirect fracture tests or lack of spatial resolutions in revealing the atomic configurations of the 2D materials at the crack tip. To better understand the behavior of 2D materials upon fracture, it is ideal and essential to conduct *in situ* fracture tests inside transmission electron microscopy (TEM) in which both high-resolution mechanical testing and characterizations can be achieved [25]. So far, there is a scarcity of such studies.

In this study, we report *in situ* TEM fracture tests conducted on monolayer MoSe<sub>2</sub> and reveal the extrinsic toughening effect from an ultrathin (2.12 nm) adsorbed polystyrene adlayer, which enhance the energy release rate of monolayer MoSe<sub>2</sub> by a maximum of 15 fold. Under continuous electron beam irradiation and cyclic loading condition, the monolayer MoSe<sub>2</sub> sample exhibit further micro-cracking, crack-blunting, and bridging effects that delayed the failure of the specimen. With a combined molecular dynamics/extended finite element simulations, we show that such toughening effect arises from the active crack-bridging effect of the adsorbed polystyrene adlayer. Those results elucidate the significant toughening effect of an ultrathin polymer adlayer on 2D materials. We envision that such toughening can facilitate the fabrication of devices based on 2D materials by preventing catastrophic failure of the 2D flakes.

## 6.2. *In Situ* Fracture Test

*In situ* fracture testing on monolayer MoSe<sub>2</sub> was conducted with Hysitron PI95 Picoindenter inside FEI Titan 80-300 (S)TEM and FEI Talos F200X (S)TEM. The Picoindenter was used with push-to-pull (PTP) devices (Fig. 6.1(a)) to convert the indentation motion of the indenter tip to tensile force applied to the sample. Monolayer MoSe<sub>2</sub> flakes were synthesized with chemical vapor deposition and transferred to the region of interest (ROI, denoted as specimen in Fig. 6.1(a)) of the PTP device with polystyrene as the carrier polymer. Inspired by Graf et al. [30], we developed a sample transfer technique that can precisely locate the flake to the ROI, as detailed in Chapter 2. After locating the monolayer MoSe<sub>2</sub> to the ROI, the polystyrene layer was washed off to form a suspended monolayer. This step had a low

yield and always left a thin layer of polystyrene regardless of the type of solvent that was used and the duration of the wash-off process. The existence of polymer residue was confirmed by the amorphous ring in the FFT pattern of the HRTEM image (Fig. 6.1(c)). The thickness of polystyrene on successfully transferred MoSe<sub>2</sub> flakes range from 1.36 nm to 4.48 nm with some extent of local fluctuations. While existing studies show that polystyrene residues on 2D materials can be reduced by thermal annealing at 400 °C for an extended period of time, we found that such treatment did not eliminate the polymer residue and often caused damage to the suspended monolayer MoSe<sub>2</sub>, resulting in an even lower yield.

The suspended monolayer sample was trimmed by focused ion beam to define a rectangular geometry (Fig. 6.1(b)). Next, the sample was loaded into the TEM followed by focused electron beam irradiation to create an initial crack and define a single-edge notched specimen (Fig. 6.1(c)). The initial crack was created to follow the zigzag direction of the suspended monolayer MoSe<sub>2</sub>. To achieve that, we took HRTEM images (Fig. 6.1(d)) of the suspended sample and extracted the FFT pattern. The six spots closest to the center spot corresponded to the zigzag surface, and direction in the real space that is perpendicular to the six reciprocal vectors is thus the zigzag direction. A displacement-controlled fracture test was conducted by indenting at the protrusion of the PTP device, which drove one edge of the suspended sample away from the other and then stretched the sample. The interfacial adhesion was sufficient to prevent sliding of the suspended monolayer. The measured force was the sum of both the PTP device (which has an intrinsic stiffness) and the sample. To extract force from the sample, the measured force was subtracted from force from the PTP device (calculated by indenting on the PTP device after the sample failed completely).

Fig. 6.1(e) shows the force-displacement curve of a fracture test (denoted as Test 1) on monolayer MoSe<sub>2</sub> with  $1.35 \pm 0.6$  nm of polystyrene adlayer. The stiffness of the specimen was 348.77 N/m, corresponding to an effective modulus of 89.7 GPa. Assuming a monolayer thickness of 0.77 nm, the effective modulus of MoSe<sub>2</sub>/Polystyrene, according to the rule of mixture prediction, is 63.07 GPa. As shown in Fig. 6.1(f-i), the crack propagated for  $\sim 60$  nm in a stable fashion before catastrophic failure occurred. Such a stable crack propagation stage suggested the existence of an R-curve, which is indicative of some extent of ductility in the sample. This is in sharp contrast to previous results obtained from *in situ* SEM

tensile tests [109] and *in situ* HRTEM tests, both of which showed that pristine monolayer MoSe<sub>2</sub> is a brittle material whose fracture toughness approaches Griffith's criterion. We computed the fracture toughness  $K_{IC}$  and the critical energy release rate  $G_{IC}$  as follows:

$$K_{IC} = \frac{P}{B\sqrt{W}} f\left(\frac{a}{W}\right) \cos^2 \beta \quad (6.1)$$

$$G_{IC} = \frac{K_{IC}^2}{E_{eff}^2} \quad (6.2)$$

where  $P$  is the load,  $B$  is the thickness of the specimen,  $W$  is the width of the specimen,  $a$  is the initial crack length,  $\beta$  is the angle of the crack with respect to the horizontal direction, and  $f$  is a geometrical factor that accounts for the finite specimen size. It was obtained from finite element method (FEM) simulations.  $E_{eff}$  is the effective modulus of the specimen. The measured  $K_{IC}$  ranged from 1.28 to 1.86 MPa·m<sup>1/2</sup>, corresponding to  $G_{IC}$  from 17.34 to 36.77 J·m<sup>-2</sup>, respectively. Those values exceed those of a pristine monolayer MoSe<sub>2</sub> (0.709 MPa·m<sup>1/2</sup> and 3.1 J·m<sup>-2</sup>), and seem to suggest significant toughening effect from the polystyrene adlayer.

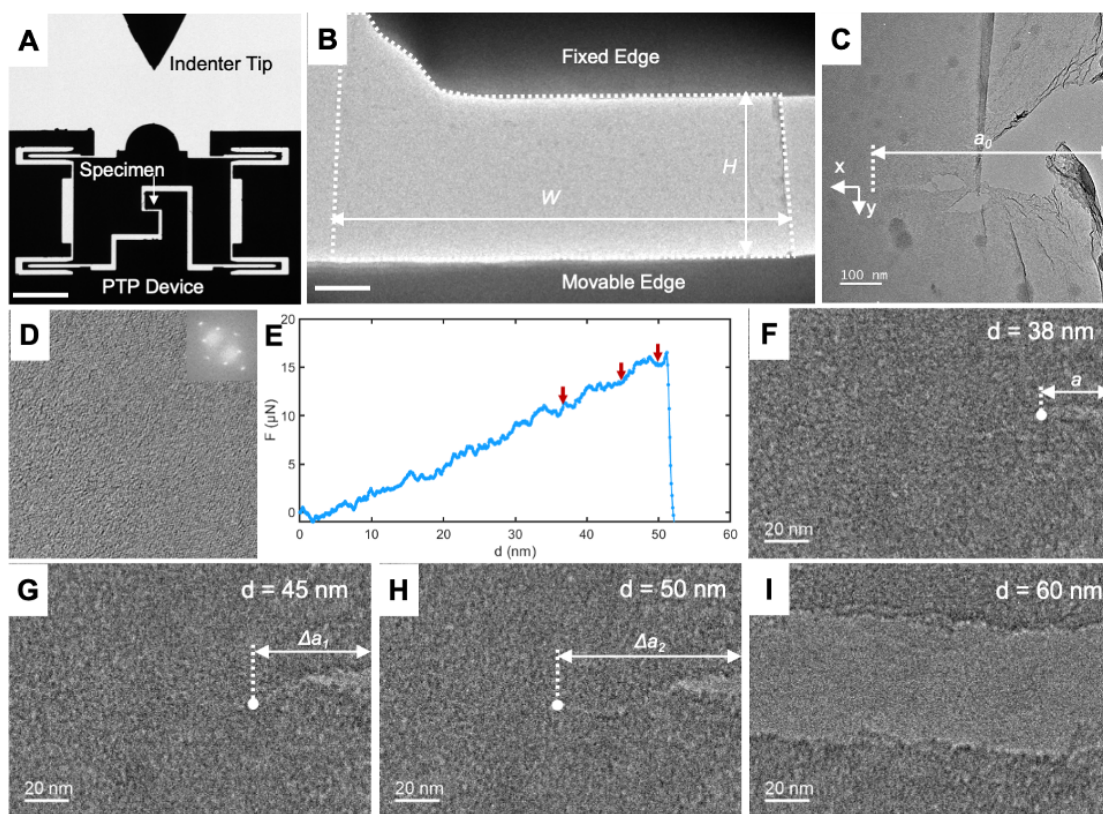


Figure 6.1. *In situ* TEM fracture test setup and results of test 1. (a) *In situ* fracture test setup. The indenter tip indents at the protrusion of the push-to-pull (PTP) device, converting the compressive force from the indenter tip to the tensile force applied to the sample. (b) Configuration of the suspended monolayer MoSe<sub>2</sub> specimen with 1.35 nm of adsorbed polystyrene adlayer. The sample was trimmed by focused ion beam to define a rectangular shape. (c) Initial crack created with focused electron beam. (d) HRTEM image of the specimen. Polystyrene was visible as the amorphous features in the image and its signal was captured as the rings in the FFT pattern (inset). (e) Force (F) - displacement (d) curve of the fracture test. The red arrows indicate the at which the TEM images were taken. (f-i) TEM images of the crack tip at  $d = 38$  nm, 45 nm, 50 nm, and 60 nm, respectively. Scale bar: (a): 60  $\mu\text{m}$ ; (b): 600 nm; (c): 100 nm; (d): 5 nm; (f-i): 20 nm.

Fig. 6.2(a) shows the geometry of another suspended monolayer MoSe<sub>2</sub> flake with  $1.23 \pm 0.5$  nm polystyrene adlayer (denoted as Test 2). Similar to the specimen of Test 1, polymer and the amorphous ring was still visible in the HRTEM image and the FFT pattern (Fig. 6.2(b)). Fig. 6.2(c) shows the corresponding force-displacement curve. The sudden drops in force (at 65, 105, 131, and 141 nm displacements) corresponded to crack-advancement events. Different from Test 1, the crack was arrested

after each advancement event, which allowed the specimen to bear further load. Figure 6.2(d-f) shows low-magnification TEM images of the crack at different stages of propagation. The crack deflected from the horizontal direction and inclined toward one edge of the specimen. The stiffness of the specimen was supposed to drop after each crack-advancement event. However, we note that the stiffness increased after the second crack-advancement event. We hypothesized that it was due to slight change in contact after the protrusion of the PTP device snapped back to the indenter tip. We picked the first two crack-advancement events to quantify the fracture toughness using equation 6.1 and 6.2. The  $K_{IC}$  value was 0.85 and 1.70  $\text{MPa}\cdot\text{m}^{1/2}$ , corresponding to  $G_{IC}$  of 12.82 and 51.26  $\text{J}\cdot\text{m}^{-2}$ ), respectively.

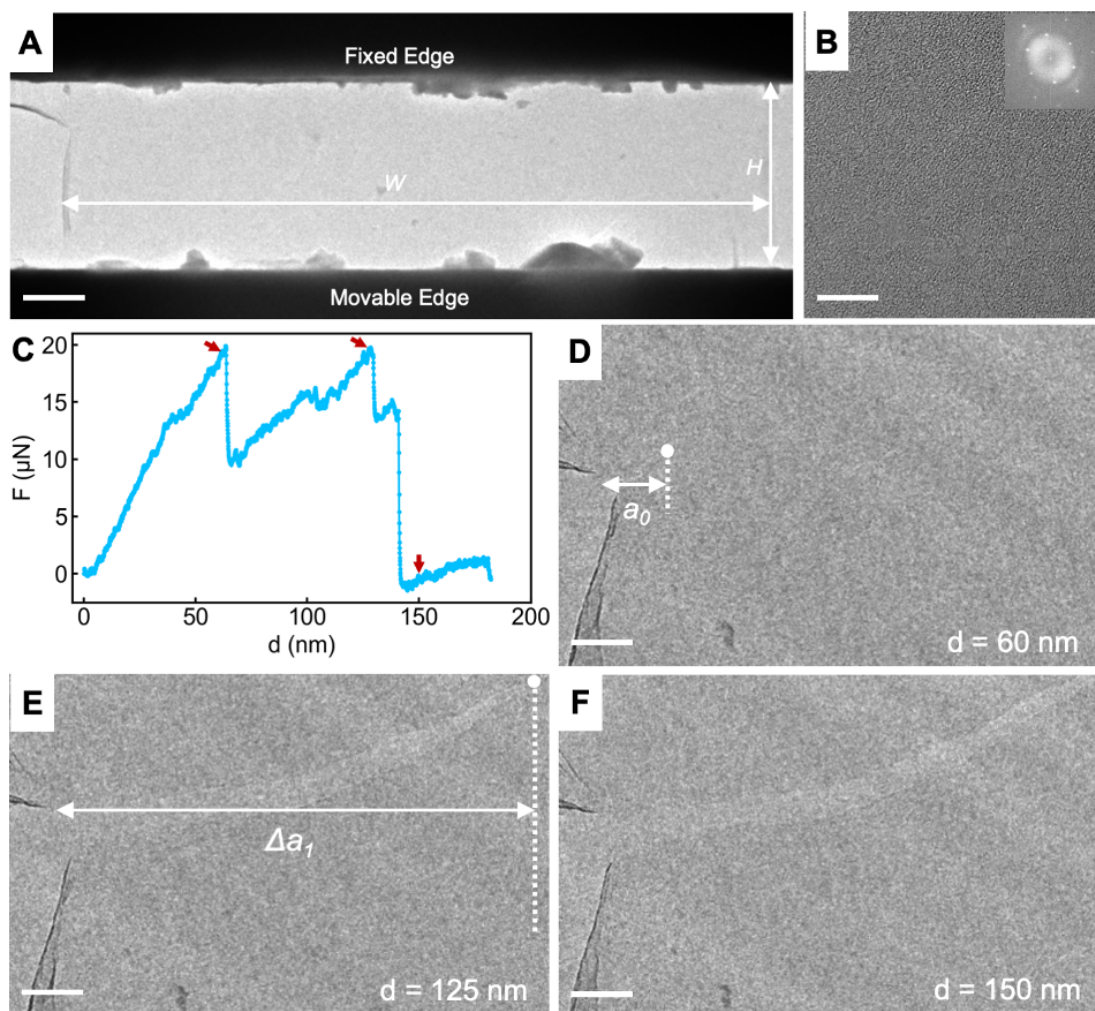


Figure 6.2. ***In situ* TEM fracture test setup and results of test 2.** (a) Configuration of the suspended monolayer MoSe<sub>2</sub> specimen with 1.35 nm of adsorbed polystyrene adlayer. The sample was trimmed by focused ion beam to define a rectangular shape. (b) HRTEM image of the specimen. Polystyrene was visible as the amorphous features in the image and its signal was captured as the rings in the FFT pattern (inset). (c) Force (F) - displacement (d) curve of the fracture test. The red arrows indicate the at which the TEM images were taken. (d-f) TEM images of the crack tip at  $d = 60$  nm, 125 nm, and 150 nm. Scale bar: (a): 600 nm; (b): 5 nm; (c): 100 nm; (d): 5 nm; (f-i): 150 nm.

Figure 6.3 summarizes the energy release rate of the two samples. The data was fitted with an arctan function, which clearly shows the contour of an R-curve. As the crack propagated, a fracture process zone (FPZ) was developed which led to increased energy release rate. The energy release rate saturated when the FPZ was fully developed, after which the crack was anticipated to propagate in a stable fashion. However, such an idealized situation was usually not satisfied in real experimental setups and was particularly hard to capture with single-edge notch tests. Pristine MoSe<sub>2</sub> should not possess such an R-curve due to its brittle nature. While atomic defects such as vacancies have been shown to alleviate the brittleness of monolayer MoS<sub>2</sub> and MoSe<sub>2</sub>, the fracture process zone should be much smaller than that measured herein. Indeed, the FPZ size ( $\sim 300$  nm, estimated to be the crack length at which J saturated) is close to that measured in in graphene oxide (GO)-poly(vinyl alcohol) (PVA) system (127.3 nm), in which the PVA adlayer interacted preferably with the oxidized domain of GO and enhanced the energy release rate of GO by 2-fold through crack-bridging. A similar crack-bridging was hypothesized to give rise to the increase in energy release rate in the as-measured MoSe<sub>2</sub>-polystyrene systems.

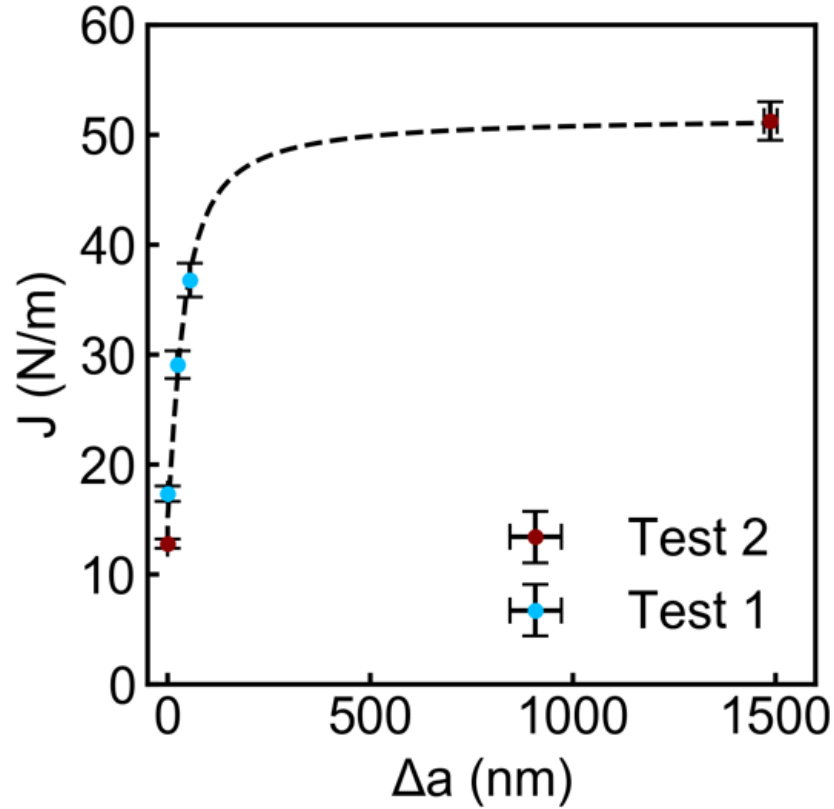


Figure 6.3. **Energy release rate computed from test 1 and test 2.** The data was fitted by an arctan function.

A third displacement-controlled *in situ* fracture test was conducted on monolayer MoSe<sub>2</sub> with 4.476 nm of polystyrene adlayer (Fig. 6.4(a)). In this experiment, we gradually increased the maximum displacement and under each maximum displacement conducted cyclic loading-unloading tests of 3-10 times. As such, the specimen underwent extensive electron beam irradiation, which was anticipated to introduce atomic defects into the monolayer MoSe<sub>2</sub> [22, 142]. Fig. 6.4(b-d) shows the crack tip configurations during the tests. Notably, several features associated to ductile fracture was observed. First, micro-cracks of 30-100 nm in length developed in front of the crack tip. The micro-cracks were stitched by the polystyrene adlayer. Second, the crack tip blunted significantly. Third, the microcracks and the main crack all deflected upward. Indeed, a second crack initiated near the upper edge of the

sample and eventually connected to the main crack under observation. With FEM simulations, a lower-bound of the fracture toughness corresponding to such a geometry was computed to be  $17.5 \text{ J}\cdot\text{m}^{-2}$ .

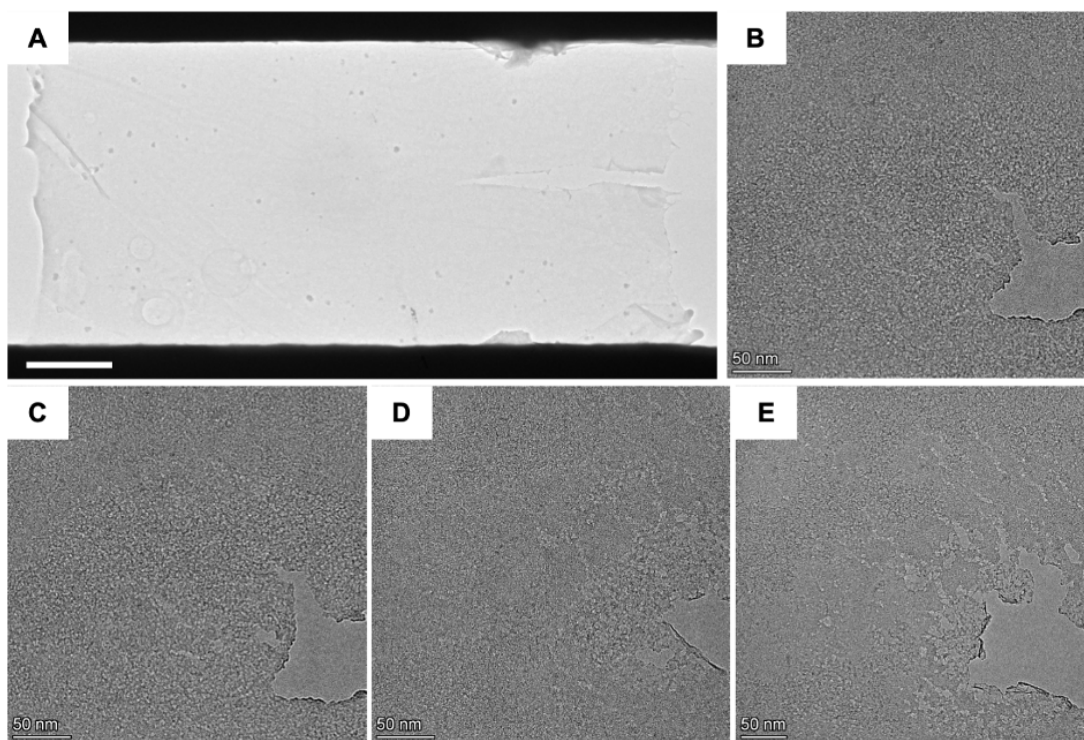


Figure 6.4. *In situ* TEM fracture test under cyclic loading conditions with different maximum displacements. (a) Configuration of the suspended monolayer  $\text{MoSe}_2$  specimen with 4.476 nm of adsorbed polystyrene adlayer. The sample was trimmed by focused ion beam to define a rectangular shape. (b-d) TEMs image of the crack tip after 10 nm, 40 nm, 50 nm, and 70 nm cyclic-loading conditions. The crack tip gradually blunted, with microcracks of 30-100 nm developed in front of the major crack.

### 6.3. Chapter Summary

A significant increase up to 15 times in the energy release rate was identified in monolayer  $\text{MoSe}_2$  with ultrathin polystyrene adlayer. An R-curve and the corresponding stable crack propagation stage was also captured with in situ TEM fracture test. The fracture process zone is estimated from the R-curve to be 300 nm and resembles that measured in graphene oxide (GO)-polyvinyl alcohol (PVA) system in which the PVA adlayer actively bridges the propagating crack in GO. Herein, we show that a similar

mechanism also exists in MoSe<sub>2</sub>/PS system. The findings can be utilized to maintain mechanical integrity of 2D materials during sample transfer and fabrication.

## CHAPTER 7

# Computational Exploration of Extrinsic Toughening of Graphene Oxide with Ultra-thin Polymer Adlayers

## 7.1. Introduction

Two-dimensional (2D) materials, with exceptional physical properties derived from sub-nanometer thick well-defined atomic structures, hold enormous potential for the development of next-generation devices, including flexible displays and bio-integrated systems such as flexible electronics [9, 71]. However, they tend to exhibit intrinsic brittle fractures [109, 131], which raises integrity concerns in large-scale applications where defects and stresses are inevitable. Thus, the exploration of toughening strategies for these 2D materials to overcome their intrinsic mechanical weaknesses has emerged as a critical research frontier in recent years [160]. While many chemical insights have been garnered over the past decade [161], a quantitative understanding of the toughening mechanism is still lacking.

Mechanistically, the strategies that have been proposed for toughening 2D materials can be broadly classified as either intrinsic or extrinsic. Intrinsic toughening includes introducing "traps" ahead of a crack tip to retard crack propagation, either through strain-induced functional groups transformations [158] or by topological defects that can dissipate the crack energies [21, 162]. Extrinsic toughening, on the other hand, requires the deposition of a second material to bridge, and thus impede, a propagating crack through strong interfacial adhesion. Among various 2D materials, graphene oxide (GO) is one in which both types of toughening can be deployed due to its rich and versatile surface chemistry. As a functionalized derivative of graphene, GO possesses a plethora of functional groups including hydroxyl, epoxy, and carboxyl [163, 164], whose chemical compositions can be tuned at will to afford materials with a broad range of mechanical properties [151, 158, 165–169]. For example, intrinsic toughening in epoxide-rich GO can be enabled through an epoxide-to-ether transition that dissipates energy during

tensile loading [158], resulting in a 100% enhancement in toughness in comparison to a hydroxylated GO. Pathways to extrinsic toughening of GO nanosheets have been demonstrated by the incorporation of polymers that can form an extensive network of hydrogen bonds (HBs) with its surface oxygen functional groups. Indeed, GO has been combined with a variety of hydrogen-bonding-capable synthetic and biopolymers such as PVA [170], PMMA [170], silk fibers [171], and chitosan [172], resulting in macroscopic GO-polymer nanocomposites that are stronger and tougher than GO paper alone. While these earlier experiments are highly inspirational, there is a lack of quantitative knowledge on how polymer properties such as chemical compositions and chain conformations may affect the ability of the polymer layer to hinder a propagating crack. Achieving a better understanding of such structure-property relationships would enable the materials engineering community to expand the scope of available GO-based materials beyond the intrinsic toughening of GO itself.

In this chapter, we report that the fracture toughness of monolayer GO can be increased by 40-180% through the incorporation of an ultra-thin (1.5-4 nm) layer of hydrogen-bonding-capable polymers with the chain randomly distributed on the surface. Up to 310% increase in fracture toughness can be achieved with poly(acrylic acid) if the polymer chains are fully extended and oriented orthogonally against the propagation direction of the crack. This discovery is made possible through a systematic molecular dynamics (MD) study that unravels how the propagation of cracks in a GO nanosheet is impeded by the polymer chains. MD simulations over a small library of hydrogen-bonding-capable polymers enable a comprehensive optimization of the chemical composition, chain conformation, and surface adsorption of the polymer adlayer to allow for the strongest interactions possible with the heterogeneous functional chemistry of the GO sheet, and thus the best fracture toughness. Surprisingly, it reveals that the cohesive bonding between the HB-capable polymer adlayer and the GO surface is also significantly affected by van der Waals (vdW) interactions. Together, these results allow us to establish key design criteria for deploying polymers that can better impede the crack propagation in monolayer GO, suggesting that the range of polymers implemented in GO-polymer nanocomposites can (and should) be extended beyond a selected few that are known to form HBs and  $\pi - \pi$  stacking interactions with the GO surface [161]. Such

simulation-driven analysis can eventually be generalized to understand toughening in any functionalized 2D material system that does not have HB capabilities.

## 7.2. General Considerations of the Molecular Dynamics Simulations

The CHARMM general force field (CGenFF) [83] was used to model the GO-polymer system. The atomic charges and force field parameters for bonded interactions of polymer molecules were obtained from the CGenFF program (interface version 1.0.0, force field version 3.0.1) [173] by uploading training structures of each polymer with 10 repeating units. The Lennard-Jones parameters for polymers were obtained from CGenFF C36 version [83, 174]. The force field parameters for GO were taken from Fonseca et al. [175] GO flakes were generated by a Monte Carlo Algorithm described in an earlier work [151] with seventy percent of the carbon atoms oxidized and a 4-to-1 epoxide-to-hydroxyl group ratio. Polymer chains were generated by a self-avoiding random walk method. The Large-scale Atomic/Molecular Massively Parallel Simulator (LAMMPS) software package [176] was used to run MD simulations. The timestep was set to be 1 fs, and the inner and outer cutoff distances for non-bonded interactions were set to be 10 and 12 Angstroms, respectively.

## 7.3. Crack-opening Simulation Setup

For these simulations, a pre-cracked GO flake with dimensions measuring 7.5 x 7.1 nm was created by cleaving the GO plane along the armchair or zigzag direction of GO and separating the cleaved surfaces by 2 Å. Six atactic polymer chains with their average mean-square end-to-end distance corresponding to their melt states were suspended over the GO flake. The contour length was kept to be 32.5 nm for all polymers (90 repeating units for PEG and 134 repeating units for all the other polymers). The GO flake is large enough to adsorb a polymer chain without affecting its end-to-end distance. Periodic boundary conditions were applied in all directions with a  $\sim 9$  nm vacuum above and below the GO-polymer system in the z-direction. To facilitate the polymer adsorption, the polymer chains were pushed against the GO with a potential wall at 650K for 0.1 ns, during which the polymer chains interacted via a soft repulsive potential to maintain their melt-state statistics. Upon contact with the surface, the potential wall was

removed, and the normal potential was re-established. This process simulated an idealized melt-spinning of polymer on GO where the polymer chains were not affected by solvation and the polymer contour length was maximized against phase separation or intramolecular interactions.

After energy minimization using the steepest descent algorithm, the system was kept at 650 K under an NVT ensemble for 4 to 8 ns (the time to achieve energy convergence varies between polymers) and then annealed to 300 K for 1 ns. During the equilibration, the motion of GO atoms was restricted with a soft spring in all directions to avoid rigid body motion. After equilibration, the simulation box was deformed in the direction perpendicular (in-plane) to the crack with a strain rate of  $10^9/s$ . We note that while this strain rate is unrealistic in comparison to what can be achieved in experiments, it can ensure convergence as shown by a previously reported sensitivity analysis [149] as well as in this work (Fig. 7.1). Only the coordinates of GO atoms were mapped into the new box to avoid artificial stretching of the polymer phase. The stress (with a unit of stress volume) in the polymer phase was calculated by summing the per-atom virial stresses of all polymer atoms. Then, it was divided by the x dimension of the box (see Fig. 7.6(a)) to calculate the crack-bridging force and then divided by the y dimension of the box to calculate 2D Traction ( $T_{2D}$ , with a unit of force/length). A moving average filter of 20 steps was applied to smooth  $T_{2D}$ . A total of six simulations (three with the pre-crack along the armchair direction and three along the zigzag direction) were performed for each polymer, in which the location of the crack was changed while keeping the same initial polymer configuration, thus providing different polymer configurations over the crack.

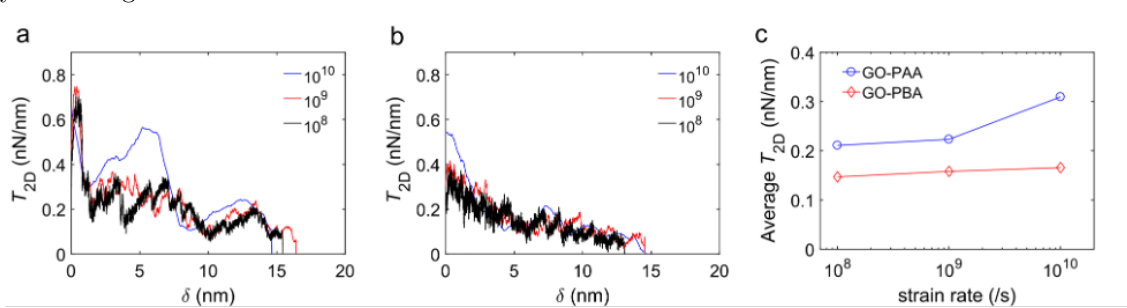


Figure 7.1. Rate-dependent behaviors of the crack-opening simulations for representative hydrogen-bonding and vdW-interaction GO-polymer systems. (a)  $T_{2D} - \delta$  curves for a GO-PAA system at three strain rates. (b)  $T_{2D} - \delta$  curves for a GO-PBA system at three strain rates. (c) Average  $T_{2D}$  values taken from the data in (a) and (b) as a function of the strain rate.

#### 7.4. Single-chain Pull-off Simulation Setup

For these simulations, one chain at its contour length was adsorbed onto an  $11 \times 3.2 \text{ nm}^2$  GO flake. The contour length was kept to be 9.7 nm for all polymers (27 repeating units for PEG and 40 for all other polymers). Periodic boundary conditions were applied in the  $y$ -direction (see Fig. 7.6(c)). The system was equilibrated in an NVT ensemble at 300K for 1 ns, during which the out-of-plane undulation of GO was restricted by applying spring supports in the  $y$ - and  $z$ - axes. The steered molecular dynamics (SMD) method was used to pull the backbone carbon atom at the terminal group with a spring with a spring constant of 100 kcal/mol·Angstrom at a constant velocity of 3.8 m/s, during which the pulling force ( $F$ ) and the displacement of the carbon atom ( $d$ ) were measured. The pulling velocity was consistent with the strain rate used in the crack opening simulations, and was slow enough for the HBs to reform after a stick-slip event. Throughout the simulation, the rigid body motion of GO was restricted by applying spring supports. A total of five simulations were performed for each polymer in which different initial velocities for atoms were generated. The HBs between the polymer and GO were counted with a criterion of donor-acceptor distance  $< 3.5 \text{ \AA}$  and H-acceptor-donor angle  $< 30^\circ$  [177]. The  $N_{HB}/N$  values were calculated by dividing the total number of simulation-observable HBs that the polymer chain made with the GO surface by the number of monomers on the surface of GO ( $N$ ) at the corresponding timestep. To compare the crack-bridging effects in HB-dominated PAA- and PVA-GO models, we adopted a methodology that was used to study the collective effect of HBs on rupture strength in HB assemblies [178]. We simulated two deformation modes of polymers on GO: out-of-plane peeling and in-plane shear (same as the single-chain pull-off), as shown in Fig. 7.6). In the peeling mode, HBs were cleaved sequentially (i.e., one by one) from the GO surface; however, multiple HBs can be cleaved simultaneously in the shear mode in one stick-slip motion. We found the average rupture force of one cleavage (peeling mode) and one stick-slip motion (shear mode), and calculated the ratio of the average force in the shear and peeling mode ( $N_{cr}$ ),

which revealed how many HBs were cleaved simultaneously in one stick-slip motion. Visualization and post-analysis of the system were accomplished with OVITO [42].

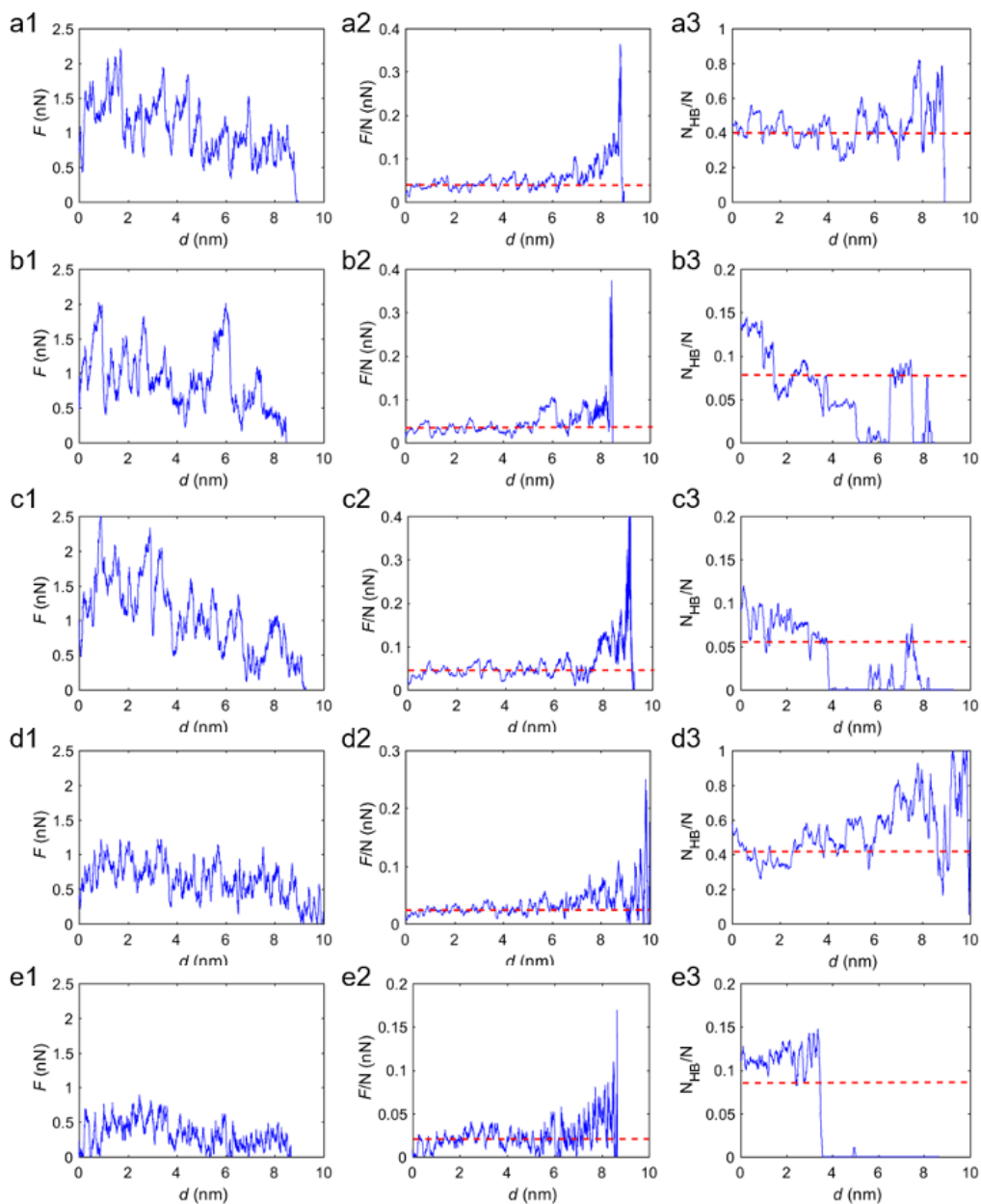


Figure 7.2. Single-chain pull-off simulations for various polymers. The letter a-e represent curves for PAA, PMA, PBA, PVA and PEG, respectively. The numeral 1-3 represent  $F$ ,  $F/N$  and  $N_{HB}/N$  for each polymer, respectively.

## 7.5. Selection of Model Systems

Recently, Soler-Crespo et al. [149] reported that an ultra-thin layer of poly(vinyl alcohol) (PVA) adsorbed on epoxide-rich GO (4:1 epoxide/hydroxyl ratio), fabricated using an experimental Langmuir-Blodgett deposition strategy, can significantly enhance the toughness of GO without sacrificing its native 2D modulus. For GO-PVA nanolaminates, AFM-based indentation tests reveal a three-fold enhancement of load-bearing capability and several-fold increase of energy dissipation in comparison to GO nanosheet. Such enhancements were proposed to arise from a crack-bridging mechanism where the propagation of nanoscale cracks can be obstructed by the stretching of PVA chains over fissures that are as large as 10-20 nm. The strong toughening effect by the polymer chains was made possible due to their multiple-hydrogen-bond interactions with the surface oxygen groups of the GO sheet. These interactions are maximized due to the synergistic matching of the oxidized domain size of the substrate and the length of the adsorbed polymer chain. A similar crack-bridging scheme has also been proposed for a covalently linked graphene-carbon nanotube system [159], raising the possibility that a general approach for bridging the propagation of cracks can be proposed for a broad range of materials that interact strongly with a 2D nanosheet. Thus, we hypothesize that a systematic tuning of the interactions between the polymer adlayer and the GO sheet can result in an expansion of the scope of available GO-polymer materials through extrinsic toughening. We set out to investigate this idea using an epoxide-rich GO nanosheet model that is similar to that used experimentally by Soler-Crespo et al. [149] to favor strong interactions with the hydrogen-bonding-capable polymer adlayer. This in turn will facilitate the comparison of the crack-bridging properties in GO-based nanocomposites by polymers with different chemical and structural features and allow for a clear elucidation of the extrinsic toughening effect from a molecular-level consideration.

For model polymers that can form hydrogen bonds with the epoxide-rich GO, we select five oxygen-containing polymers that have often been used in GO-polymer nanocomposites: poly(acrylic acid) [179], poly(methyl acrylate), poly(vinyl alcohol) [170], poly(butyl acrylate) [180], and poly(ethylene glycol) [181] (abbreviated as PAA, PMA, PVA, PBA, and PEG, respectively). This focused library (Fig. 7.3) allows for full coverage of the two key factors that affect HB formation between these oxygen-containing

polymers and the surface oxygen species of GO: the types of HB species and the "length" of the side group. The three main types of HB species (carboxyl, hydroxyl and ether functional groups) are studied by comparing PAA, PVA, and PEG. Notably, the critical effect of having both HB donor/acceptor in the same polymer are elucidated in the series of two homologous carboxylated polymers (PAA, PMA), with PAA being able to both donate and accept hydrogen atoms (HB donor/acceptor) while PMA only capable of accepting hydrogen atoms (HB acceptor). Comparing PMA to PBA reveals the effect of the side group length. Moreover, the contribution to the toughening from vdW interactions increases for PMA and PBA, which allows us to contrast the toughening effect from HBs with that from vdW interactions.

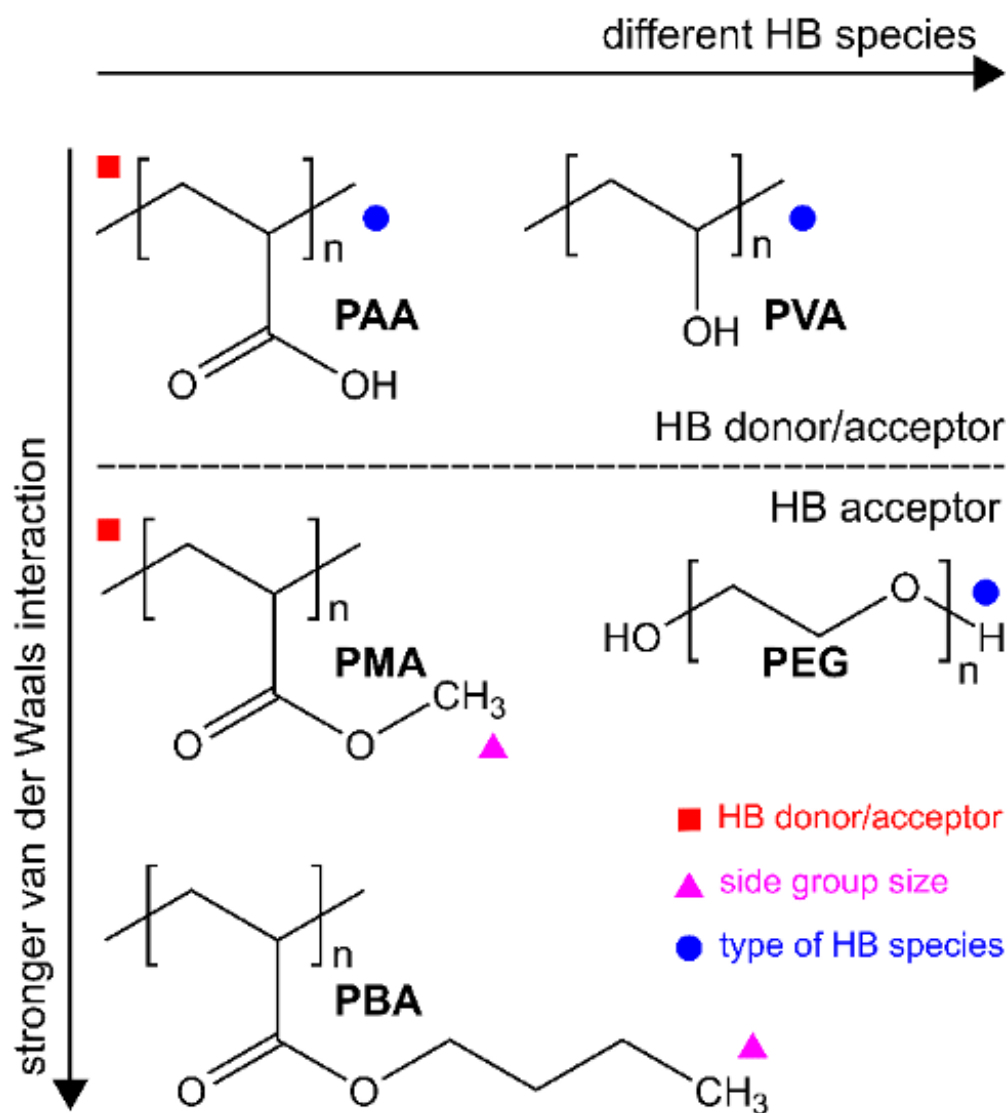


Figure 7.3. Model polymer systems including poly(acrylic acid) (PAA), poly(methyl acrylate) (PMA), poly(butyl acrylate) (PBA), poly(vinyl alcohol) (PVA), and poly(ethylene glycol) (PEG) classified according to the type of HB species and relative strength of vdW interactions. Polymer pairs whose performance are compared for specific design criteria, namely, HB donor/acceptor, side group length and type of HB species, are marked with the same symbols (red square, purple triangle, and blue circles), respectively.

To be consistent with the GO-PVA experimental system reported by Soler-Crespo et al., [149] we employ a 134-repeating unit (degree of polymerization (DP) = 134) PVA chain and a final polymer thickness of  $\sim 1.5$  nm in our model, equivalent to 6 polymer chains for a  $7.5 \times 7.1$  nm<sup>2</sup> GO sheet and

$\sim 48$  wt % PVA composition. The number of the polymer chains (6) and polymer length (DP = 134) are maintained for the GO-polymer models with the remaining vinyl-typed polymers (PAA, PMA, and PBA), which has 2 C in each repeating unit in the backbone. For PEG, which has 2 C and 1 O in each backbone repeating unit, a polymer chain of equivalent length (DP = 90) is chosen but the number of polymer chain/GO sheet is still maintained at 6.

### 7.6. Adsorption of Polymer Chains on GO

To explore the toughening effects of polymer adlayers as they would exist in a composite material, we configured our model system as a mixture of GO and polymer melts. Following the approach described in Auhl et al. [182], we generated polymer chains with melt-state conformations and maintained their melt-state statistics until they were adsorbed onto the GO surface. After contact, the whole system was kept above the glass-transition temperature of the polymers until the total energy converges to a minimum. The crack-bridging simulation was then performed after this annealing process. Drawing an analogy from the bridging of cracks in fiber composites, which is controlled by the fiber conformation (embedded length, orientation, etc.) [183], we hypothesize that the extrinsic toughening, or the crack-bridging effect, in our GO-polymer models would be similarly governed by the nanoscale conformation of polymer chains (end-to-end distance and orientation). However, as our vinyl polymer chains are "flexible" on a molecular scale, they can form a multitude of intra- and inter-chains interactions that greatly reduce their end-to-end distance in comparison to their contour lengths (i.e., the length of the polymer at maximum physically possible extension) [184]. This in turn will affect the crack-bridging properties of a polymer chain at the nanoscale as its fully extended conformation across a crack is expected to impede the propagation of that crack better than a coiled up one.

Fig. 7.4(a) shows the physical probability curves for finding an atom from the adsorbed polymer chains at a given height or distance (D) from the basal plane of the GO sheet. These number-density profiles all have a peak at  $\sim 0.45$  nm, representing atoms that are in direct contact with the GO sheet, or in other words, "closely adsorbed". As the side group of the polymer becomes larger, the proportion of these closely adsorbed atoms decreases, from 0.22 for PEG to 0.04 for PBA. At the same time, the

thickness of the polymer adlayer increases, from 1.55 nm for PEG to 4.45 nm for PBA. A second peak at  $\sim 1$  nm, arising from the non-bonded neighbors of the closely adsorbed atoms, is also visible in the number-density profiles but becomes less obvious with increased side group size, again consistent with the decreased proportion of close-adsorbed atoms. To characterize the extent that the backbone of a polymer chain associates with a surface, we employ the orientation-order parameter  $P_2(\phi)$  [185, 186], which is calculated as:

$$P_2(\phi) = \frac{1}{2} \langle 3 \cos^2 \phi - 1 \rangle \quad (7.1)$$

where  $\phi$  is the angle between the vector that is normal to the surface (i.e., the z-axis, Fig. 7.6(a)) and the backbone bonds of the adsorbed polymer chains. Good adsorption occurs when all the backbone bonds are parallel to the adsorbed surface, resulting in  $P_2(\phi) = -0.5$  ( $P_2(\phi) = 1$  when all the backbone bonds are perpendicular to the surface, and  $P_2(\phi) = 0$  when the backbone bonds adopt random orientations). Fig. 7.4(b) shows the plots of  $P_2(\phi)$  for the five polymers in this study at various distances  $D$  from the GO surface. Consistent with the ultrathin nature of the polymer adlayer, the  $P_2(\phi)$  plots for all five GO-polymer models exhibits a minimum negative value at  $\sim 0.45$  nm, the distance of the closely adsorbed backbone atoms.

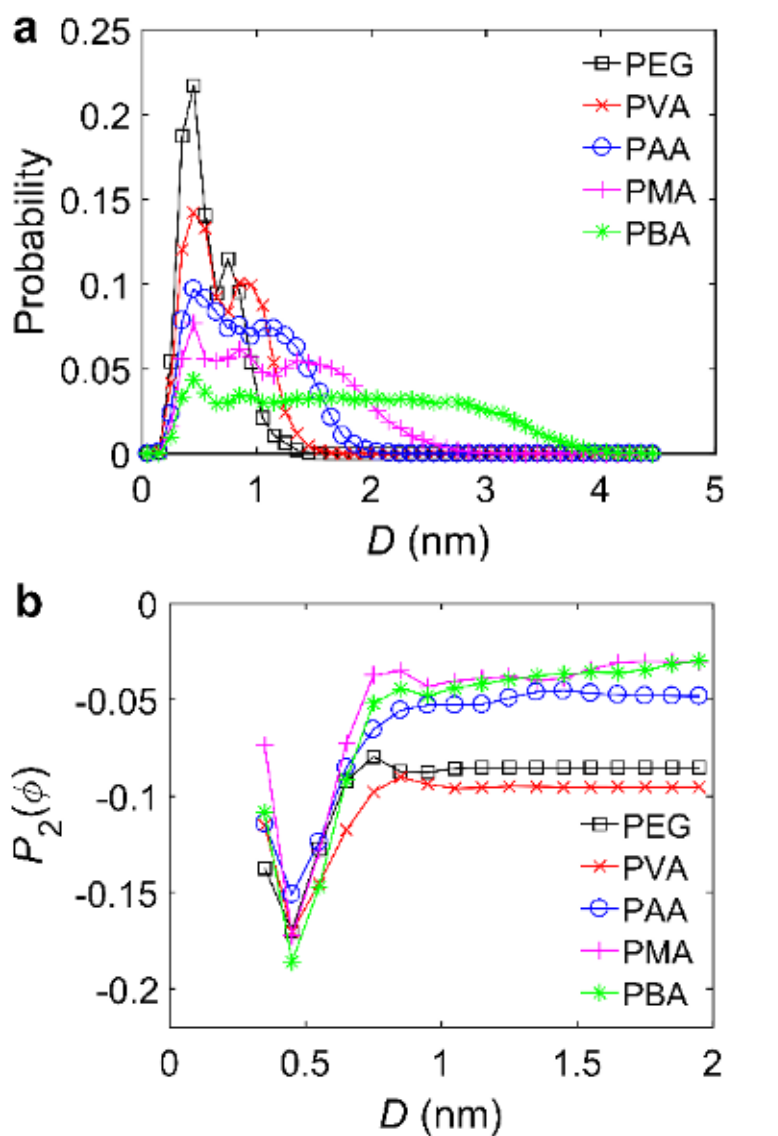


Figure 7.4. Adsorption of polymer chains on GO. (a) Probability for polymer atoms at a certain height or distance ( $D$ ) from the basal plane of GO. (b) The orientational parameter  $P_2(\phi)$  of the backbone bond at various distance ( $D$ ) from the basal plane of GO.

### 7.7. Crack-opening Simulation Results

To quantify the toughening effect of the various polymers investigated herein, we implement Rice's J-integral approach [133], which captures non-linear crack-tip-toughening processes that occur in materials

that do not behave in an elastic fashion, as have been observed for GO nanosheets [151, 158]. As well-known in the literature for fiber-reinforced composites [122, 183, 187], the presence of a small amount of reinforcing fibers in a material can greatly enhance its ability to resist the propagation of developing cracks. The presence of fiber effectively allows for the development of a process zone (i.e., the region of space surrounding the crack tip) whose size is not negligible compared to the crack length, thus invalidating the fundamental assumption of linear-elastic fracture mechanics. In the case of macroscopic fiber-reinforced composites, good bridging fibers can effectively resist the further opening of a large crack by dissipating a significant amount of energy through the decohesion of the fiber-matrix interface beyond the intrinsic fracture energy of the matrix itself [122]. We thus envision that a similar mechanism will arise in the GO-polymer systems examined in this work where the polymer chains can bridge a developing nanoscale crack by anchoring to the GO sheet through HBs.

Unlike many brittle materials whose fracture energy can be characterized solely by a single number  $G_0$ , the critical energy release rate, the resistance of polymer-toughened GO composites must be described by a resistance (R) curve (see Fig. 7.5), whose steady-state value can be estimated by calculating the 2D energy release per unit distance following the established J-integral approach for a fiber-reinforced system [122, 183, 187]:

$$G_c = J_c = G_0 + G_f = G_0 + \int_0^{\delta_c} T(\delta)d\delta \quad (7.2)$$

where  $G_c$  is the critical energy release rate (expressed in energy/distance unit) of the composite,  $G_f$  is the energy release rate due to bridging,  $T$  is the traction between the crack surface, and  $\delta_c$  is the size of the critical crack-opening after which  $T$  vanishes.  $G_c$  is calculated by super-imposing  $G_0$  (the critical energy release rate of GO, found to be 4 nJ/m for GO monolayers as the average of a hydroxyl-rich GO (3.4 nJ/m) and an epoxide-rich GO (4.6 nJ/m) [168, 188]) and the energy dissipation from the polymer  $G_f$ . As the value of  $G_0$  implicitly "contains" information for an already initiated and propagated crack [187], we can investigate the non-linear effects of polymer toughening in GO by examining only the process of crack-opening (i.e., behind the crack tip).

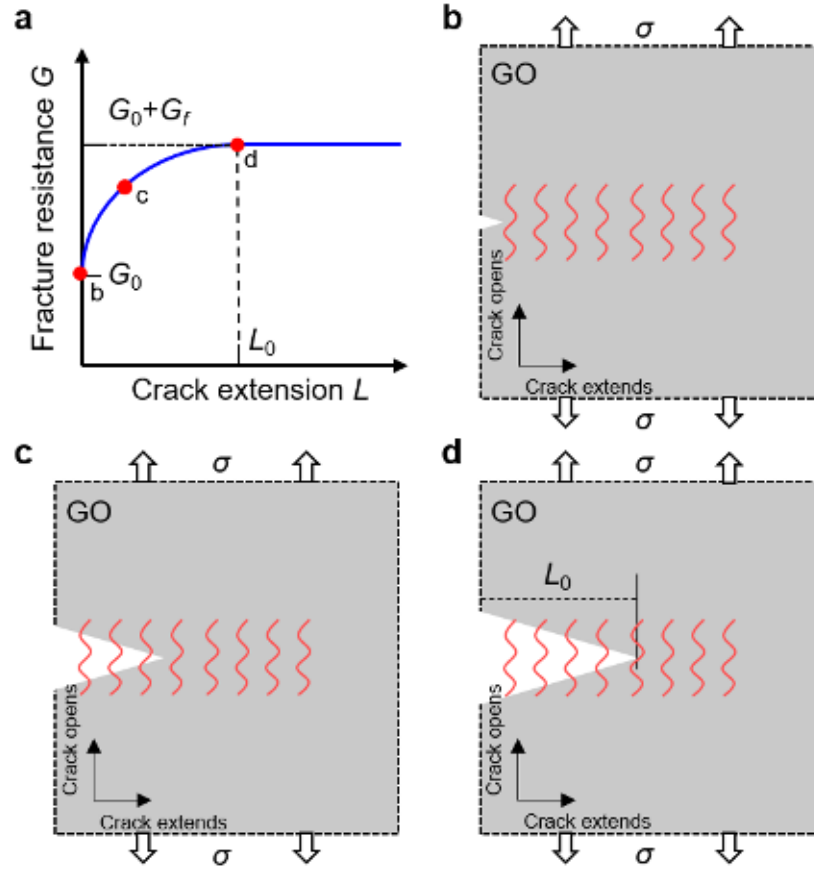


Figure 7.5. Critical energy release rate with polymer crack-bridging. (a) Fracture-resistance curve for the GO-polymer systems. (b)-(d) Snapshots of the crack-bridging with the corresponding fracture resistance marked in (a).

We note in passing that while equation 7.2 is derived for a continuum system with homogeneous distribution of masses, and we used atomistically discrete molecular models in our MD simulation, the physics that underline Rice’s J-integral formalism still hold. The molecular models are simply used as representative volume elements (RVEs) to estimate the behavior of the material in the energy-dominated regime, where the crack size is much larger than their dimensions. At such a scale difference, local mass fluctuations caused by non-uniform distributions of polymer chains are negligible and the entire system is considered ”homogenized”.

Fig. 7.6(a) shows the schematic of our crack-opening simulation, which involves multiple polymer chains that were randomly adsorbed on a pre-cracked GO sheet. We calculated the crack-bridging force provided by the polymer and then divided the force by the width of GO (the y dimension in Fig. 7.6(a)) to obtain the 2D traction ( $T_{2D}$ ) as a function of the crack opening ( $\delta$ ) (see Fig. 7.7(a)). As expected,  $T_{2D}$  decreases as the crack-bridging chains are being pulled off from the GO surface and their stick-slip motions can be observed as irregular "peak-valley" patterns along the diminishing traction profile. To quantify the crack-bridging effect, we calculated the 2D energy release rate  $G_f$  (Fig. 7.7(b)) for all polymers by integrating the areas under the  $T_{2D}$  profiles (Fig. 7.7(a)). From this data, the enhancement in GO-fracture toughness due to the polymer crack-bridging effect ( $(G_c - G_0)/G_0$  which is  $G_f/G_0$ ), is 40-180% (Fig. 7.7(c)), comparable to that observed experimentally (up to 200%) for an ultrathin GO-PVA nanocomposite [149].

As shown in Fig. 7.7(b), the crack-bridging performances of the four vinyl-functionalized polymers (PAA, PMA, PVA and PBA) randomly adsorbed on GO, as represented by the blue bars, are better than that for PEG, albeit with large standard deviations that can partially be attributed to the discrepancy between the large number of possible starting conformations by the six polymer chains in this system (an ideal conformation will be described in the next paragraph) and the limited number of possible replica simulations. Nevertheless, assuming that  $G_f$  follows a Gaussian distribution, we used the Student's t-distribution to compare the  $G_f$  values between pairs of polymers to elucidate the toughening effect by the different types of HB species and the length of the side group. At 95% level of confidence, such analysis reveals that the  $G_f$  of PAA is larger than those of PMA (p-value [189] = 0.042) and PVA (p-value = 0.048). However, the suggestion that the  $G_f$  of PAA is larger than that of PBA, which in turn is larger than the  $G_f$  of PMA, can only be made at  $\sim 80\%$  level of confidence.

To better quantify the crack-bridging effect of each of the five polymers in this study, we reduced the large number of possible starting conformations for the nanocomposite down to an ideal crack-bridging scenario where all of the polymer chains were adsorbed onto the GO surface at their contour length and were aligned orthogonal to the crack propagation direction, as shown in Fig. 7.6(b). These systems were then equilibrated following the same procedure used for the random conformation case.

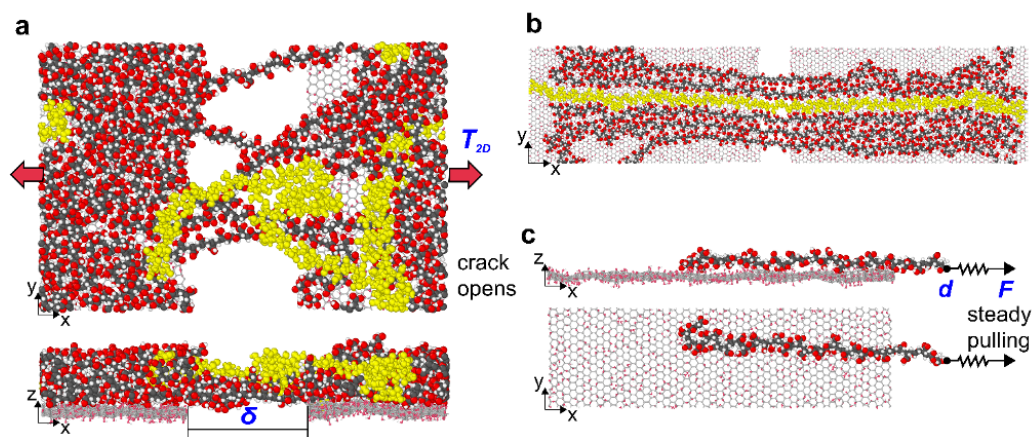


Figure 7.6. Schematic illustrations of the GO-PAA simulation system in this study. Carbon atoms are colored grey, oxygen atoms are colored red, and hydrogen atoms are colored white. To contrast with the polymer, the GO molecules have been reduced in their relative sizes. When the simulation comprises multiple polymer chains, as in panels (a) and (b), one representative polymer chain is highlighted in yellow to make visualization easier for the readers. (a) A crack-opening simulation where polymer chains are randomly adsorbed on a pre-cracked GO prior to its opening. Our model comprises six 134-repeating unit polymer chains adsorbed on a  $7.5 \times 7.1 \text{ nm}^2$  GO sheet and a final polymer thickness of  $\sim 1.5 \text{ nm}$  ( $\sim 60 \text{ wt } \% \text{ PAA}$ ). The number of the polymer chain (6) and polymer length ( $\text{DP} = 134$ ) were maintained for all the four GO-vinyl-functionalized polymer models (PAA, PMA, PBA, and PVA), which have 2 C in each repeating unit in the backbone. For PEG, which has 2 C and 1 O in each backbone repeating unit, the equivalent polymer was chosen as a chain with  $\text{DP} = 90$  but the number of polymer chain/GO sheet was still maintained at 6. The 2D traction ( $T_{2D}$ ) was recorded as a function of the crack-opening ( $\delta$ ). (b) An ideal crack-opening scenario with all six polymer chains close to their contour length and aligned orthogonally to the crack-propagation direction. (c) A single-chain pull-off simulation where a single polymer chain ( $\text{DP} = 40$  for vinyl polymer models, and  $\text{DP} = 27$  for PEG) is pulled off from the surface of GO with a spring force at a constant velocity. The pulling force ( $F$ ) and the displacement ( $d$ ) of the carbon atom being pulled along the x-direction were measured.

We further constrained the simulation to have all chains being simultaneously pulled off from the same side of the crack. The obtained  $G_f$  values for the five models in this idealized scenario, represented as green bars in Fig. 7.7(b), are consistently much higher than those for the randomly adsorbed case (blue bars in Fig. 7.7(b)). Notably, the  $G_f$  value for the PAA provided the best crack-bridging effect, with 310% enhancement (Fig. 7.7(c)) in fracture toughness. While not directly comparable, this value is very similar to that recently modeled for the covalently linked graphene-CNT system [159] (360% enhancement in energy release rate with completely aligned CNT arrays), suggesting that excellent extrinsic toughening

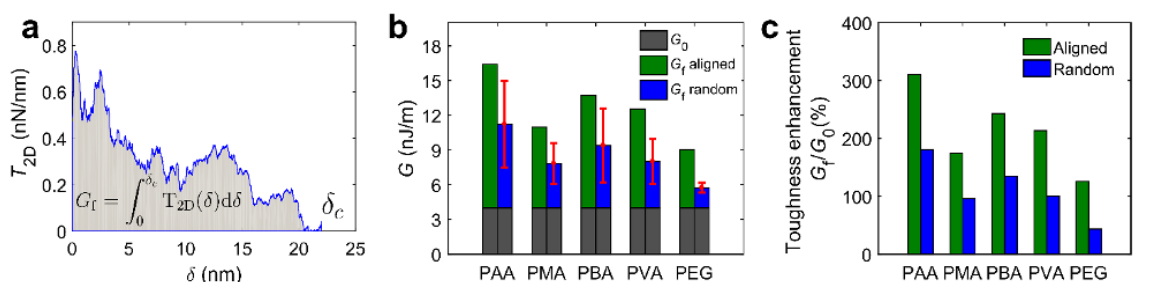


Figure 7.7. Results of the crack-opening simulations. (a) A typical 2D traction ( $T_{2D}$ ) - crack opening ( $\delta$ ) curve of a GO-PAA system. (b) 2D energy release rate  $G$  for the GO and GO-polymer systems.  $G_0$  represents the 2D energy release rate of GO itself.  $G_f$  values were calculated by numerically integrating the  $T_{2D}$  -  $\delta$  curve for all polymers. The blue bars are  $G_f$  values of the polymers with random chain arrangements (Fig. 7.6(a)). The sample standard deviations were calculated from six simulations, a small number that limited by our available computational resources. The green bars correspond to cases where all polymer chains are aligned orthogonal to the crack propagation direction and contribute to the crack-bridging (Fig. 7.6(b)). (c) Enhancement of the fracture toughness of GO from the adsorbed polymers with aligned and random chain conformations. The enhancement was calculated as  $G_f/G_0$ . The average  $G_f$  values were used for the random cases.

in GO-based nanocomposites can indeed be achieved with ultrathin soft polymer adlayers as long as strong chemical interactions can be engineered into the system. Notably, the optimal  $G_f$  values for these ideal crack-bridging simulations have a strong positive correlation with the average  $G_f$  of the aforementioned randomly adsorbed GO-polymer models (correlation coefficient of 0.9848), allowing us to increase the level of confidence in the latter set of data, and conclude that PAA > PBA > PVA > PMA > PEG in crack-bridging. As experiments that can verify such a relationship would require an enormous amount of effort in both fabrication and measurement of the types recently reported [149], our MD predictions can serve as a facile pre-screen prior to the more expensive and time-consuming experimental phase.

In addition to the fracture energy, nanoscale fracture behavior has also been proposed to be governed by a "characteristic size" of the flaw-tolerance phenomena [122, 190], which can potentially be modified by the polymer adlayer. In our estimation, the presence of the polymer adlayer should have a minimal effect on the intrinsic characteristic size of the GO sheet. When the defect size is smaller than the characteristic size, where the strength of the material controls the failure, the adsorbed un-stretched polymer chains, which have a much lower stiffness than GO; would have a negligible contribution to relieving the stress

concentration in GO and thus does not affect its characteristic size. On the other hand, for defects that are larger than the characteristic size, in the energy-dominated regime, the adlayer can provide an extrinsic toughening to GO, as shown herein. In essence, while the polymer adlayer does not prevent fracture initiation from defects, it does contribute to resisting its growth.

### 7.8. Single-chain Pull-off Simulation Results

To understand the aforementioned trend in crack-bridging simulations in terms of HB donor/acceptor effect, the length of the side groups, and the type of HB species, we carried out single-chain pull-off simulations (Fig. 7.6(c)) for each of the adsorbed polymer model, starting from the ideal crack-bridging configuration of the polymer chain being orthogonal to the propagation direction the crack. To reduce the computational cost and increase the statistical accuracy, we decreased the system size (the polymer length was shortened to  $\sim 1/3$  and the GO area was reduced by  $\sim 1/2$ ) and assumed a configuration where each of the polymer chain initially resided on one side of the crack. The polymer was then pulled off from this one side, essentially constraining the polymer motion to only "one GO surface". In this configuration, all polymer chains started with similar contour length and followed similar motion paths, so the difference in their cohesive behaviours can be solely attributed to the chemical properties of the polymer. Following an approach that was applied to simulate the motion of hydrogen-bonding-capable polypeptides on hydroxylated substrates [191], the polymer chain was pulled off the GO surface with a spring force ( $F$ ) at a constant velocity (Fig. 7.6(c)). During the pull-off simulations, we measured  $F$  as a function of the displacement ( $d$ ) of the polymer carbon atom to which the spring was connected. Since we pulled the chain off at a constant velocity, the spring force varied as a function of the instantaneous GO-polymer interactions, allowing for the "detection" of stick-slip motions that were proportional to the magnitude of the interaction energy with the GO surface.

As shown in Fig. 7.8(a), the  $F - d$  curve for the GO-PAA system clearly displays a jagged sawtooth pattern that is indicative of the expected stick-slip behaviour for a PAA chain that forms multiple HBs with the GO surface. As the pulling initiates, multiple HBs serve as anchoring points to the GO surface, causing the PAA chain backbone to stretch and giving rise to local increases of the pulling force (stick

stages). Rupturing these HBs releases the stored elastic energy and leads to a sudden drop in the pulling force (slip stage), where interfacial sliding occurs. After this slip, HBs quickly reform between the GO surface and the next repeating unit of the PAA chain, building up to the next rupture/slip event and ultimately resulting in several stick-slip transitions throughout the polymer pull-off process. As the values for  $F$  and  $d$  of the stick-slip events are larger than those for the rupture of a single hydrogen bond, each slip event must involve the rupture of HBs in a cluster fashion [178]. The average number of HBs that rupture in such a cluster can then be estimated from the release of elastic energy [178].

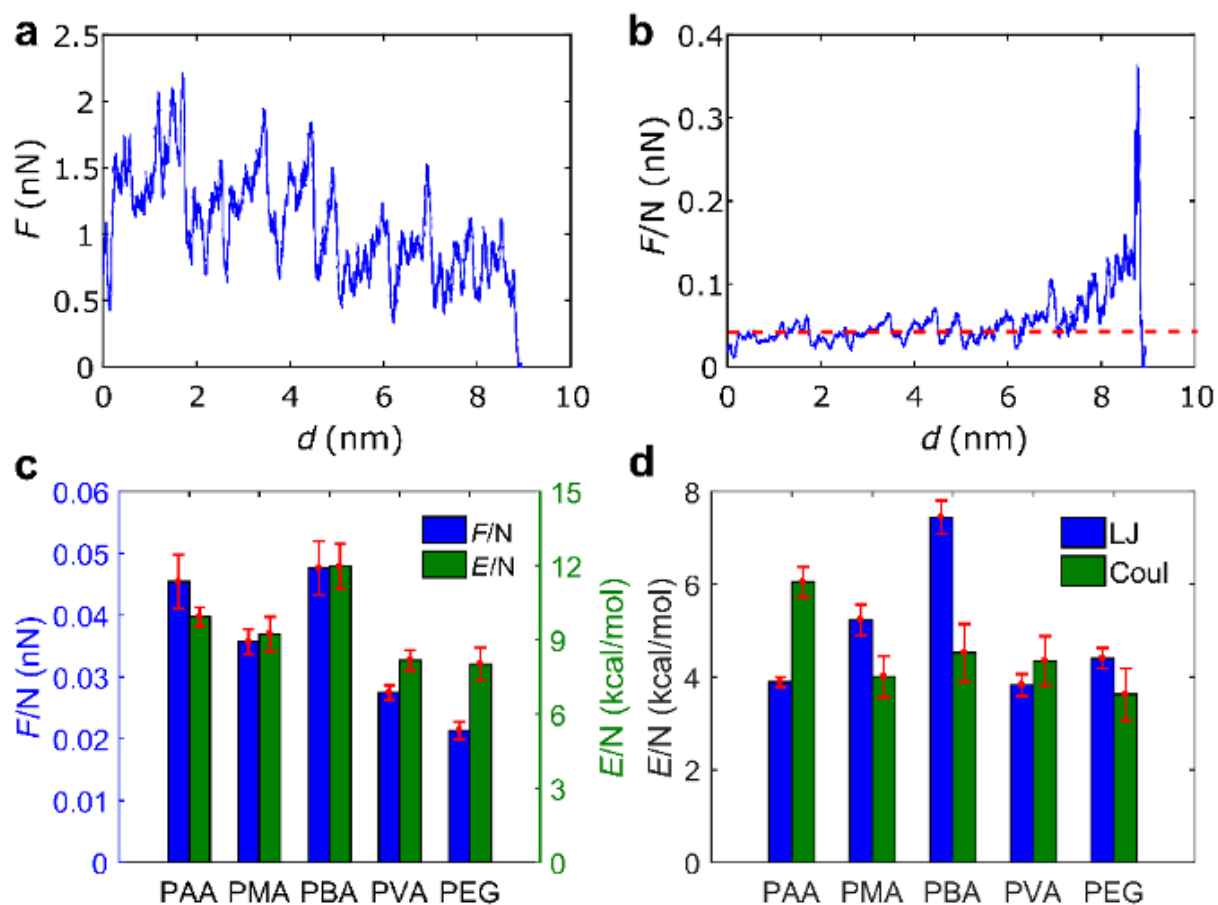


Figure 7.8. Results of the single-chain pull-off simulations for models comprising a 9.7-nm-long polymer chain (27 repeating units for PEG and 40 for all other polymers) adsorbed on an  $11 \times 3.2 \text{ nm}^2$  GO sheet. (a) A representative pulling force ( $F$ ) vs displacement ( $d$ ) curve for the GO-PAA system. (b) The force in Fig. 7.8(a) normalized by the number of repeating units ( $N$ ) that were instantaneously adsorbed on the GO surface. The red dashed line corresponds to the average of the  $F/N$  data from 0-5 nm. For (a)-(b), the data shown were processed through a forward-moving average filter over 20 points. (c) The average per-repeating-unit force ( $F/N$ ) and molar binding energy ( $E/N$ ) for all five polymer models. The average  $F/N$  value is defined as the average of the  $F/N$  data for each polymer in the 0-5 nm displacement range. The average  $E/N$  is defined as the molar per-repeating-unit change in the GO-polymer interfacial energies between the  $\frac{1}{2}$ -pull-off stage (i.e.,  $\frac{1}{2}$  of the initial polymer chain has been pulled off) and the minimum-energy state before any of the repeating unit is pulled-off. (d)  $E/N$  for all five polymer models, separated into Lennard-Jones (LJ) and Coulombic (Coul) energies. For (c) and (d), the error bars represent sample standard deviations that were calculated over five replicates of simulations.

Fig. 7.8(a) shows a gradual decrease in the pulling force as the polymer chain in our PAA-GO model is pulled off the GO surface, not surprisingly, due to the decrease in polymer-GO interactions. Normalizing this force by the number of repeating units ( $N$ ) that are instantaneously adsorbed on the surface of GO shows that the per-repeating-unit force ( $F/N$ ) remains at a steady-state value of  $0.045 \pm 0.004$  nN (red line in Fig. 7.8(b) and Fig. 7.2) up to a displacement of 5 nm ( $\frac{1}{2}$  of the initial polymer length), suggesting that it can be used to represent the average force that each repeating unit of the polymer chain "exerts" on the GO surface when the opening of the crack is  $\leq \frac{1}{2}$  the length of the polymer chain. As such, this average  $F/N$  value can be correlated to the strength of interactions between each repeating unit of the PAA chain with the GO surface, and thus its overall crack-bridging behaviour.

Indeed, the trend in  $F/N$  data (Fig. 7.8(c)) for all of our polymers tracks quite well with the trend in the molar per-repeating-unit binding energy  $E/N$ , suggesting that the pulling force exerted on the GO surface by each type of polymer can be understood in terms of the chemical interactions as parameterized by the MD force fields<sup>1</sup>. Additionally, as  $E/N$  can be decomposed into Lennard-Jones (LJ) and Coulombic (Coul) energies, the strength of the interactions between each polymer chain and the GO surface can be further quantified in terms of vdW and HB interactions [192], respectively (Fig. 7.8(d)).

### 7.9. Comparison Between the Multi-chain Crack-opening and Single-chain Pull-off Simulations

While the single-chain pull-off simulations can be considered simplified snapshots of our multi-chain crack-opening simulations, the  $PBA \geq PAA > PMA > PVA > PEG$  trend in  $F/N$  data (Fig. 7.8(c)) does not quantitatively agree with the  $PAA > PBA > PVA > PMA > PEG$  trend in  $G_f$  data (Fig. 7.7(b)). Together with the larger-than-Coulombic LJ contributions to  $E/N$  data found for PBA and PMA (Fig. 7.8(d)), this discrepancy highlights the significant capability of vdW interactions to provide good crack-toughening interfaces. Taken one step further, this observation suggests that the scope of polymer adlayers that can toughen GO-polymer nanocomposites can (and should) be extended to include polymers that

<sup>1</sup>We note that while the trends for  $E/N$  and  $F/N$  data track well with each other, they cannot be directly compared as  $E/N$  data were calculated based on only two data points: one at the beginning of the pull-off experiment and the other when the polymer chain was completely off the surface. In contrast, the  $F/N$  data was based on a moving average throughout the whole experiment.

have good vdW interactions with the GO surface in addition to the few that were historically chosen due to their perceived abilities to form strong HBs and  $\pi - \pi$  stacking interactions with GO [161]. While the of potential GO-polymer composites. For example, our work herein clearly shows that replacing the carboxyl groups in PAA with the carboxymethyl group in PMA can increase the LJ contribution to  $E/N$  to exceed the Coul component (Fig. 7.8(d)). Further increase of the size of the ester group to a larger carboxybutyl group, as in PBA, increases the LJ contribution to  $E/N$  to almost twice that of the Coul component, and this leads to the  $F/N$  value for PBA being comparable to PAA in the single-chain pull-off simulation. Supporting this notion is the recent report that polydimethylsiloxane (PDMS), which primarily interacts with GO through vdW interactions, significantly enhances the toughness and stiffness of graphene-based nanocomposites in comparison to GO foam (28 higher toughness and 65 higher stiffness with 1.5 wt % of PDMS) [193, 194].

Interestingly, while the  $G_f$  value of PVA is almost twice that of PEG in the multi-chain crack-opening simulation (Fig. 7.7(b)), its  $F/N$  value is quite similar to that of PEG in the single-chain pull-off simulation (Fig. 7.8(c)). Given the identical atomic composition between these two polymers (repeating units =  $C_2H_4O$ ) and the better "packing" of the PEG chains on the GO surface (Fig. 7.4(a)), this inconsistency can only be attributed to the additional crack-bridging effect from a network of hydrogen-bonded polymer chains produced by inter-chain HBs in the GO-PVA case, as has been proposed to explain experimental crack-toughening [161, 195]. This is akin to the case of fiber-reinforcement concrete where a network of "crack-bridging" struts can lead to vast improvements in the ability of the matrix to impede the crack propagation.

That PBA and PAA both have similar  $F/N$  values in the single-chain pull-off simulations (Fig. 7.8(c)) but large differences in  $G_f$  data in the multi-chain crack-opening simulations (Fig. 7.7(b)) further indicates a clear reduction in the ability of a randomly distributed multi-chain PBA film to bridge a developing crack in comparison to PAA. This is presumably due to a reduction of GO-polymer interactions: the large carboxybutyl side groups of the PBA chains do not allow them to pack in the adlayer in a manner that maintains the most optimal interactions between each polymer chain and the GO surface, as confirmed by the lower proportion of closely adsorbed atoms for PBA when multiple chains are present (Fig. 7.4(a)).

In such a situation, polymer-polymer inter-chain vdW interactions presumably increase at the expense of GO-polymer interactions. In the next section, we will make an attempt to quantify the relationship between chemical effects, such as the types of hydrogen bonds and their number, and the crack-toughening mechanism.

### 7.9.1. Evaluation of Chemical Effects in Single-chain Pull-off Simulations

The per-repeating-unit strength of the HB interaction that our five polymers make to the GO surface can also be obtained from the single-chain pull-off simulations as the dimensionless quantity  $N_{HB}/N$  (Fig. 7.9(a)). This value allows us to separate our five models into two classes: those that can only accept hydrogen atoms (PMA, PBA, and PEG) and those that can both accept and donate hydrogen atoms (PAA and PVA). Notably, comparing PAA and PMA, whose carboxyl side groups are roughly of the same size, offers clear insights into how these different HB capabilities are translated into very different Coul contributions. With its carboxyl groups capable of both donating and accepting HBs, PAA can form more HBs with our epoxide-rich GO surface (epoxide groups are HB acceptors) in comparison to PMA (Fig. 7.9(a)), resulting in a higher Coul contribution (Fig. 7.8(d), cf Coul energies). Although the methoxy groups of PMA do provide some vdW interactions, the accompanying energy gain (Fig. 7.8(d), cf LJ energies) does not adequately compensate for the loss of HB interactions, thus yielding lower overall  $E/N$  and  $F/N$  data (Fig. 7.8(c)). Such a comparison clearly indicates the advantage that polymers with both HB donors and acceptors have over those with only HB acceptors in providing stronger interface with the GO sheet and thus better mechanical performance for the corresponding GO-polymer composite. This conclusion is consistent with that reported in a previous experimental study [170], where GO-PVA nanocomposites show better mechanical properties than GO-poly(methyl methacrylate) nanocomposites because the latter polymer adlayer is only capable of accepting hydrogen atoms.

Interestingly, while PVA shows an  $N_{HB}/N$  value that is 570% higher than that for PEG, this difference only manifests in  $\sim 29\%$  increase in  $F/N$ . In contrast, PAA, which has the same  $N_{HB}/N$  value as PVA but with one more "CO" in its side group, shows almost 100% increase in  $F/N$  value than PEG. This

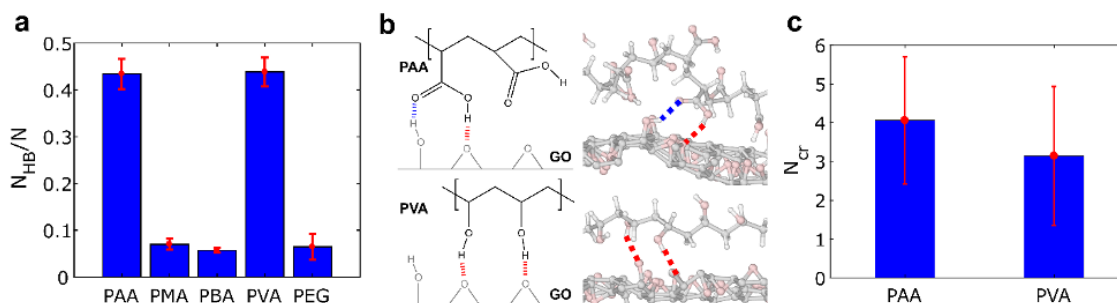


Figure 7.9. HB analysis in the single-chain pull-off simulations (a) The number of HBs observed between the polymer chain and GO normalized by  $N$  ( $N_{HB}/N$ ) for all five polymer models. HBs were counted with a criterion of donor-acceptor distance  $< 3.5\text{\AA}$  and H-acceptor-donor angle  $< 30^\circ$  [177], and were counted up to 5 nm displacement. The error bars represent sample standard deviations that were calculated over five replicates of simulations. (b) Illustration (left) and simulation snapshots (right) of cooperative HBs formed at the interface in the PAA and PVA system. For PAA, a cooperative HB pair can form within one repeating unit, where the carbonyl oxygen and hydroxyl group each forms a hydrogen bond, as shown by the blue and red dashed lines, respectively. For PVA, two repeating units are required to form a cooperative HB pair, where one hydrogen bond forms in each repeating unit. In the snapshots, carbon atoms are colored grey, oxygen atoms are colored pink, and hydrogen atoms are colored white. (c) Number of hydrogen bonds ( $N_{cr}$ ) that are cleaved in a single stick-slip motion for PAA and PVA.

difference can be explained by the better ability of PAA to form a cooperative HB pair with the epoxide-rich GO surface using just one repeating unit in the polymer chain (Fig. 7.9(b)). This is in contrast to PVA, which requires two adjacent repeating units to form such a pair (Fig. 7.9(b)). In other words, a single carboxyl group in a PAA repeating unit can form a cooperative HB pair (or participate in larger cooperative HB clusters) that would be broken in concert in a pull-off experiment [178], resulting in a stick-slip motion that has larger  $F$  and  $d$  values than those for the rupture of a single hydrogen bond. A similar stick-slip event in the GO-PVA model would require two hydroxyl groups from adjacent repeating units, leading to fewer possibilities for stick-slip transitions. Indeed, a rupture strength analysis [178] reveals that one stick-slip motion in PAA requires the cleavage of  $\sim 4$  hydrogen bonds (vs 3 for PVA; see Fig. 7.9(c)), resulting in a higher friction force observed for PAA. This finding is also consistent with the report that incorporating carboxyl-functionalized multi-walled carbon nanotubes (MWCNT) into polymer-MWCNT composites can lead to better mechanical properties than hydroxyl-functionalized MWCNT [196].

## 7.10. Chapter Summary

In summary, we have shown that the presence of an ultra-thin adlayer of oxygen-containing hydrogen-bonding-capable polymers on a monolayer epoxide-rich GO can greatly enhance the fracture toughness of this monolayer. With random chain arrangements, the largest enhancement (180%) is found for PAA, whose carboxylate side groups intrinsically place an HB-acceptor and HB-donor moiety close in space, facilitating the formation of cooperative HB clusters that synergistically enhance the interaction of the polymer with the GO surface. The breaking of cooperative HB clusters manifests into stick-slip motions of polymer chains with friction-force magnitudes that are several times larger than the breakage of a single HB. The enhancement further improves to 310% when the PAA chains are orthogonally aligned to the crack propagation direction of GO. For PMA and PBA whose carboxylate ester groups are only HB acceptors, the enhancements are slightly inferior to that of PAA but are still in an impressive 175-243% range with orthogonally aligned polymer chains. Our MD analysis clearly captures an increase in the overall LJ contribution from these polymers as a function of the length of their side groups. While this vdW contribution can potentially be restricted by the limited packing efficiency, which manifests as larger polymer thicknesses in PMA and PBA, it contributes significantly to the crack-bridging properties, resulting in non-negligible fracture toughness enhancements. Notably, a fully aligned polyethylene (PE, DP = 134) adlayer with the same steric properties as PEG but without the ability for HB formations, can result in an 83% enhancement of GO fracture toughness, highlighting the importance of vdW interactions <sup>2</sup>.

Our data strongly advocate three design criteria for rendering ultrathin GO-polymer nanocomposites that are resistant toward nanoscale cracks: 1) Maximizing the formation of cooperative HB clusters between the polymer adlayer and the GO surface; 2) Aligning the polymer chains orthogonally to the crack propagation direction; and 3) Increasing the vdW interactions for polymers that do not have both HB-donors and -acceptors. For GO, these criteria suggest that the range of polymers implemented for

---

<sup>2</sup>We note that we intentionally restricted the polymers in our simulations to be 'flexible' so as to maximize the interaction between them and GO. As a result, rigid  $\pi$ -conjugated polymer systems, such as halloysite-polyaniline, which was recently reported to enhance the tensile strength of GO paper by  $\sim 2$  times (see: C. Wu, T. Zhou, Y. Du, S. Dou, H. Zhang, L. Jiang and Q. Cheng, *Nano Energy*, 2019, 58, 517-527), was not investigated.

GO-polymer nanocomposites should be extended beyond a selected few that are known to form HBs and  $\pi$ - $\pi$  stacking interactions with the GO surface [161]. Most importantly, the last criterion opens up the possibility for toughening a broad range of 2D materials that do not have HB-forming capabilities.

We note in passing that while GO has reduced modulus and strength with respect to graphene [158] due to the presence of functional groups on its basal plane, these groups can actually render GO more damage-tolerant through an intrinsic toughening mechanism [158]. In addition, they provide possibilities for extrinsic toughening of the GO sheet through interactions with polymer adlayers as shown in this work. By applying a bottom-up materials-by-design strategy, one should be able to optimize the functional-group compositions of GO as well as their spatial distributions to maximize desirable mechanical properties for a particular GO-polymer system. Such investigation can provide important insights into the design of next-generation strong and tough composites.

Lastly, we note that as our current study was primarily aimed to unravel the chemical basis for nanoscale toughening by a polymer adlayer, we did not consider process-related conditions (degree of thermoset cure, polymer chain mobility and crystallinity etc.) and/or mixed-mode phenomenon (e.g., the deflection of the crack propagation due to the adsorbed polymers). While these have been known to affect the fracture toughness, their complexity necessitates the consideration of larger model systems and more specific force fields and would render the computation prohibitively expensive [159].

## CHAPTER 8

## Concluding Remarks and Outlook

The work conducted in this thesis comprises a systematic exploration on the fracture and toughening of two-dimensional (2D) materials, with combined *in situ* experimental/computational explorations. We propose a robust approach of parameterizing interatomic potentials for accurately capturing both the equilibrium and nonequilibrium properties of 2D materials. The framework enabled us to parametrize an interatomic potential for monolayer MoSe<sub>2</sub> for a reliable quantification of its failure and fracture properties *in silico*. We discovered edge-mediated annihilation of vacancy clusters in monolayer MoSe<sub>2</sub> and conducted detailed mechanistic study on the energetics and kinetics of such annihilation. We envisioned that such a behavior may be utilized for conducting defect-engineering in 2D materials. We proposed a combined *in situ* transmission electron microscopy/numerical exploration on the intrinsic fracture properties of 2D materials. We report the first experimental measurement on the fracture toughness of monolayer MoS<sub>2</sub> and MoSe<sub>2</sub> that agrees with both computational results and theoretical predictions from Griffith's criterion. We next show *in situ* TEM fracture tests conducted on monolayer MoSe<sub>2</sub> and reveals the extrinsic toughening effect from an ultrathin polystyrene adlayer, which enhance the energy release rate of monolayer MoSe<sub>2</sub> by a maximum of 15 folds. Lastly, we present a systematic, quantitative study on the nanoscale toughening of monolayer graphene oxide (GO) by an ultra-thin polymer adlayer, which impedes the propagation of cracks during intraplanar fracture.

A major question that awaits further investigation is how atomic defects such as vacancies, vacancy lines, and grain boundaries affect the fracture properties of 2D materials. Existing studies on such aspects are either pure computational predictions or qualitative experimental explorations. *In situ* fracture tests on pristine and defected (created by electron beam irradiation) 2D materials should provide insights on the quantitative effects of those vacancies on the fracture. Since the functional properties of 2D materials

are also found to be sensitive to the extent of defects in the sample, we envision that a synergistic enhancement may be achieved by careful introduction of defects in 2D materials.

It is intriguing to understand the failure mechanisms of 2D materials in-plane heterojunctions or out-of-plane heterostructures, which are shown to possess interesting properties due to the coupling between the two layers.. We anticipate unique failure modes for those samples, e.g., crack propagation through the junction or crack-shielding from the adsorbed second layer.

Both the experimental and computational explorations on the fracture of 2D materials were conducted at room temperature. It is anticipated that certain structural transitions or lattice reconstructions may only be active at elevated temperatures when the barrier-hopping events become easier. To capture such behavior accurately with molecular dynamics simulations, augmentation of the training/screening data is needed. Experimentally, the heating of the specimen can be incorporated into the *in situ* mechanical testing setup by utilizing customized micro-electromechanical systems (MEMS).

## References

- [1] J. Zhu, E. Ha, G. Zhao, Y. Zhou, D. Huang, G. Yue, L. Hu, N. Sun, Y. Wang, and L. Y. S. Lee, "Recent advance in mxenes: A promising 2d material for catalysis, sensor and chemical adsorption," *Coordination Chemistry Reviews*, vol. 352, pp. 306–327, 2017, ISSN: 0010-8545.
- [2] M. Khazaei, A. Mishra, N. S. Venkataramanan, A. K. Singh, and S. Yunoki, "Recent advances in mxenes: From fundamentals to applications," *Current Opinion in Solid State and Materials Science*, 2019, ISSN: 1359-0286.
- [3] J. Pang, R. G. Mendes, A. Bachmatiuk, L. Zhao, H. Q. Ta, T. Gemming, H. Liu, Z. Liu, and M. H. Rummeli, "Applications of 2d mxenes in energy conversion and storage systems," *Chemical Society Reviews*, vol. 48, no. 1, pp. 72–133, 2019.
- [4] T. Sun, G. Zhang, D. Xu, X. Lian, H. Li, W. Chen, and C. Su, "Defect chemistry in 2d materials for electrocatalysis," *Materials Today Energy*, vol. 12, pp. 215–238, 2019, ISSN: 2468-6069.
- [5] Y. Wu, H. Pang, Y. Liu, X. Wang, S. Yu, D. Fu, J. Chen, and X. Wang, "Environmental remediation of heavy metal ions by novel-nanomaterials: A review," *Environmental Pollution*, vol. 246, pp. 608–620, 2019, ISSN: 0269-7491.
- [6] M.-S. Cao, Y.-Z. Cai, P. He, J.-C. Shu, W.-Q. Cao, and J. Yuan, "2d mxenes: Electromagnetic property for microwave absorption and electromagnetic interference shielding," *Chemical Engineering Journal*, vol. 359, pp. 1265–1302, 2019, ISSN: 1385-8947.
- [7] K. Huang, Z. Li, J. Lin, G. Han, and P. Huang, "Two-dimensional transition metal carbides and nitrides (mxenes) for biomedical applications," *Chemical Society Reviews*, vol. 47, no. 14, pp. 5109–5124, 2018, ISSN: 1460-4744.
- [8] S. Manzeli, D. Ovchinnikov, D. Pasquier, O. V. Yazyev, and A. Kis, "2d transition metal dichalcogenides," *Nature Reviews Materials*, vol. 2, no. 8, p. 17 033, 2017, ISSN: 2058-8437.
- [9] Y. D. Kim, H. Kim, Y. Cho, J. H. Ryoo, C. H. Park, P. Kim, Y. S. Kim, S. Lee, Y. Li, S. N. Park, Y. S. Yoo, D. Yoon, V. E. Dorgan, E. Pop, T. F. Heinz, J. Hone, S. H. Chun, H. Cheong, S. W. Lee, M. H. Bae, and Y. D. Park, "Bright visible light emission from graphene," *Nature Nanotechnology*, vol. 10, no. 8, pp. 676–681, 2015, ISSN: 1748-3387.
- [10] Y. M. Lin, C. Dimitrakopoulos, K. A. Jenkins, D. B. Farmer, H. Y. Chiu, A. Grill, and P. Avouris, "100-ghz transistors from wafer-scale epitaxial graphene," *Science*, vol. 327, no. 5966, pp. 662–662, 2010, ISSN: 0036-8075.

- [11] A. Yoffe, "Electronic properties of some chain and layer compounds," *Chemical Society Reviews*, vol. 5, pp. 51–78, 1976, ISSN: 1460-4744.
- [12] G. Casillas, U. Santiago, H. Barrn, D. Alducin, A. Ponce, and M. Jos-Yacamn, "Elasticity of mos2 sheets by mechanical deformation observed by in situ electron microscopy," *The Journal of Physical Chemistry C*, vol. 119, no. 1, pp. 710–715, 2014, ISSN: 1932-7447.
- [13] D. Xia, F. Gong, X. D. Pei, W. B. Wang, H. Li, W. Zeng, M. Q. Wu, and D. V. Papavassiliou, "Molybdenum and tungsten disulfides-based nanocomposite films for energy storage and conversion: A review," *Chemical Engineering Journal*, vol. 348, pp. 908–928, 2018, ISSN: 1385-8947.
- [14] L. J. Cao, S. B. Yang, W. Gao, Z. Liu, Y. J. Gong, L. L. Ma, G. Shi, S. D. Lei, Y. H. Zhang, S. T. Zhang, R. Vajtai, and P. M. Ajayan, "Direct laser-patterned micro-supercapacitors from paintable mos2 films," *Small*, vol. 9, no. 17, pp. 2905–2910, 2013, ISSN: 1613-6810.
- [15] M. L. Tsai, S. H. Su, J. K. Chang, D. S. Tsai, C. H. Chen, C. I. Wu, L. J. Li, L. J. Chen, and J. H. He, "Monolayer mos2 heterojunction solar cells," *Acs Nano*, vol. 8, no. 8, pp. 8317–8322, 2014, ISSN: 1936-0851.
- [16] R. Ramachandramoorthy, W. Gao, R. Bernal, and H. Espinosa, "High strain rate tensile testing of silver nanowires: Rate-dependent brittle-to-ductile transition," *Nano Letters*, vol. 16, no. 1, pp. 255–263, 2016, ISSN: 1530-6984.
- [17] F. Yi, H. Y. Ren, J. Y. Shan, X. Sun, D. Wei, and Z. F. Liu, "Wearable energy sources based on 2d materials," *Chemical Society Reviews*, vol. 47, no. 9, pp. 3152–3188, 2018, ISSN: 0306-0012.
- [18] X. Zhang, J. Grajal, J. L. Vazquez-Roy, U. Radhakrishna, X. Wang, W. Chern, L. Zhou, Y. Lin, P.-C. Shen, and X. Ji, "Two-dimensional mos2-enabled flexible rectenna for wi-fi-band wireless energy harvesting," *Nature*, p. 1, 2019, ISSN: 1476-4687.
- [19] D. Akinwande, C. J. Brennan, J. S. Bunch, P. Egberts, J. R. Felts, H. J. Gao, R. Huang, J. S. Kim, T. Li, Y. Li, K. M. Liechti, N. S. Lu, H. S. Park, E. J. Reed, P. Wang, B. I. Yakobson, T. Zhang, Y. W. Zhang, Y. Zhou, and Y. Zhu, "A review on mechanics and mechanical properties of 2d materials-graphene and beyond," *Extreme Mechanics Letters*, vol. 13, pp. 42–77, 2017, ISSN: 2352-4316.
- [20] S. Zhang, T. Zhu, and T. Belytschko, "Atomistic and multiscale analyses of brittle fracture in crystal lattices," *Physical Review B*, vol. 76, no. 9, p. 094114, 2007.
- [21] T. Zhang and H. Gao, "Toughening graphene with topological defects: A perspective," *Journal of Applied Mechanics-Transactions of the Asme*, vol. 82, no. 5, p. 051001, 2015, ISSN: 0021-8936.
- [22] S. Wang, Z. Qin, G. S. Jung, F. J. Martin-Martinez, K. Zhang, M. J. Buehler, and J. H. Warner, "Atomically sharp crack tips in monolayer mos2 and their enhanced toughness by vacancy defects," *ACS Nano*, vol. 10, no. 11, pp. 9831–9839, 2016, ISSN: 1936-0851.
- [23] G. Lopez-Polin, J. Gomez-Herrero, and C. Gomez-Navarro, "Confining crack propagation in defective graphene," *Nano Letters*, vol. 15, no. 3, pp. 2050–2054, 2015, ISSN: 1530-6984.

- [24] K.-A. N. Duerloo, Y. Li, and E. J. Reed, "Structural phase transitions in two-dimensional monolayer and dichalcogenide monolayers," *Nature Communications*, vol. 5, no. 1, pp. 1–9, 2014, ISSN: 2041-1723.
- [25] R. Ramachandramoorthy, R. Bernal, and H. D. Espinosa, "Pushing the envelope of in situ transmission electron microscopy," *ACS Nano*, vol. 9, no. 5, pp. 4675–4685, 2015, ISSN: 1936-0851.
- [26] T. Li, "Ideal strength and phonon instability in single-layer mos<sub>2</sub>," *Physical Review B*, vol. 85, no. 23, p. 235407, 2012.
- [27] J. A. Stewart and D. Spearot, "Atomistic simulations of nanoindentation on the basal plane of crystalline molybdenum disulfide (mos<sub>2</sub>)," *Modelling and Simulation in Materials Science and Engineering*, vol. 21, no. 4, p. 045003, 2013, ISSN: 0965-0393.
- [28] A. Castellanos-Gomez, M. Poot, G. A. Steele, H. S. J. van der Zant, N. Agrait, and G. Rubio-Bollinger, "Elastic properties of freely suspended mos<sub>2</sub> nanosheets," *Advanced Materials*, vol. 24, no. 6, pp. 772–+, 2012, ISSN: 0935-9648.
- [29] A. Gurarlsan, Y. Yu, L. Su, Y. Yu, F. Suarez, S. Yao, Y. Zhu, M. Ozturk, Y. Zhang, and L. Cao, "Surface-energy-assisted perfect transfer of centimeter-scale monolayer and few-layer mos<sub>2</sub> films onto arbitrary substrates," *ACS Nano*, vol. 8, no. 11, pp. 11522–11528, 2014, ISSN: 1936-0851.
- [30] M. Graf, M. Lihter, M. Thakur, V. Georgiou, J. Topolancik, B. R. Ilic, K. Liu, J. Feng, Y. Astier, and A. Radenovic, "Fabrication and practical applications of molybdenum disulfide nanopores," *Nature protocols*, vol. 14, no. 4, pp. 1130–1168, 2019, ISSN: 1750-2799.
- [31] J. M. Soler, E. Artacho, J. D. Gale, A. Garcia, J. Junquera, P. Ordejón, and D. Sánchez-Portal, "The siesta method for ab initio order-n materials simulation," *Journal of Physics: Condensed Matter*, vol. 14, no. 11, p. 2745, 2002, ISSN: 0953-8984.
- [32] J. P. Perdew, K. Burke, and M. Ernzerhof, "Generalized gradient approximation made simple," *Physical Review Letters*, vol. 77, no. 18, p. 3865, 1996.
- [33] T. Dunning and P. Hay, *Modern Theoretical Chemistry, edited by HF Schaefer*. Plenum, New York, 1977.
- [34] N. Troullier and J. L. Martins, "Efficient pseudopotentials for plane-wave calculations," *Physical review B*, vol. 43, no. 3, p. 1993, 1991.
- [35] J. Moreno and J. M. Soler, "Optimal meshes for integrals in real-and reciprocal-space unit cells," *Physical Review B*, vol. 45, no. 24, p. 13891, 1992.
- [36] R. C. Cooper, C. Lee, C. A. Marianetti, X. Wei, J. Hone, and J. W. Kysar, "Nonlinear elastic behavior of two-dimensional molybdenum disulfide," *Physical Review B*, vol. 87, no. 3, p. 035423, 2013.

- [37] H. Chan, K. Sasikumar, S. Srinivasan, M. Cherukara, B. Narayanan, and S. K. Sankaranarayanan, "Machine learning a bond order potential model to study thermal transport in wse2 nanostructures," *Nanoscale*, vol. 11, no. 21, pp. 10381–10392, 2019.
- [38] S. Plimpton, "Fast parallel algorithms for short-range molecular dynamics," *Journal of Computational Physics*, vol. 117, no. 1, pp. 1–19, 1995, ISSN: 0021-9991.
- [39] A. Togo and I. Tanaka, "First principles phonon calculations in materials science," *Scripta Materialia*, vol. 108, pp. 1–5, 2015, ISSN: 1359-6462.
- [40] A. I. Khan, I. A. Navid, M. Noshin, H. Uddin, F. F. Hossain, and S. Subrina, "Equilibrium molecular dynamics (md) simulation study of thermal conductivity of graphene nanoribbon: A comparative study on md potentials," *Electronics*, vol. 4, no. 4, pp. 1109–1124, 2015.
- [41] D. Frenkel and B. Smit, *Understanding molecular simulation: From algorithms to applications*. Elsevier, 2001, vol. 1, pp. 1–638, ISBN: 0122673514.
- [42] A. Stukowski, "Visualization and analysis of atomistic simulation data with ovito - the open visualization tool," *Modelling and Simulation in Materials Science and Engineering*, vol. 18, no. 1, p. 015012, 2009, ISSN: 0965-0393.
- [43] K. Deb and H. Jain, "An evolutionary many-objective optimization algorithm using reference-point-based nondominated sorting approach, part i: Solving problems with box constraints," *IEEE Transactions on Evolutionary Computation*, vol. 18, no. 4, pp. 577–601, 2013, ISSN: 1089-778X.
- [44] F.-A. Fortin, F.-M. De Rainville, M.-A. G. Gardner, M. Parizeau, and C. Gagn, "Deap: Evolutionary algorithms made easy," *The Journal of Machine Learning Research*, vol. 13, no. 1, pp. 2171–2175, 2012, ISSN: 1532-4435.
- [45] Y. Hold-Geoffroy, O. Gagnon, and M. Parizeau, "Once you scoop, no need to fork," in *Proceedings of the 2014 Annual Conference on Extreme Science and Engineering Discovery Environment*, pp. 1–8.
- [46] X. Zhao, D. Fu, Z. Ding, Y.-Y. Zhang, D. Wan, S. J. Tan, Z. Chen, K. Leng, J. Dan, and W. Fu, "Mo-terminated edge reconstructions in nanoporous molybdenum disulfide film," *Nano Letters*, vol. 18, no. 1, pp. 482–490, 2018, ISSN: 1530-6984.
- [47] X. Zhang, H. Nguyen, J. T. Paci, S. K. Sankaranarayanan, J. L. Mendoza-Cortes, and H. D. Espinosa, "Multi-objective parametrization of interatomic potentials for large deformation pathways and fracture of two-dimensional materials," *Npj Computational Materials*, vol. 7, no. 1, pp. 1–11, 2021, ISSN: 2057-3960.
- [48] G. Henkelman and H. Jansson, "Improved tangent estimate in the nudged elastic band method for finding minimum energy paths and saddle points," *The Journal of Chemical Physics*, vol. 113, no. 22, pp. 9978–9985, 2000, ISSN: 0021-9606.

- [49] G. Henkelman, B. P. Uberuaga, and H. Jnsson, "A climbing image nudged elastic band method for finding saddle points and minimum energy paths," *The Journal of chemical physics*, vol. 113, no. 22, pp. 9901–9904, 2000, ISSN: 0021-9606.
- [50] S. A. Hollingsworth and R. O. Dror, "Molecular dynamics simulation for all," *Neuron*, vol. 99, no. 6, pp. 1129–1143, 2018, ISSN: 0896-6273.
- [51] S. Z. Butler, S. M. Hollen, L. Cao, Y. Cui, J. A. Gupta, H. R. Gutierrez, T. F. Heinz, S. S. Hong, J. Huang, and A. F. Ismach, "Progress, challenges, and opportunities in two-dimensional materials beyond graphene," *ACS Nano*, vol. 7, no. 4, pp. 2898–2926, 2013, ISSN: 1936-0851.
- [52] A. K. Geim and K. S. Novoselov, "The rise of graphene," in *Nanoscience and Technology: A Collection of Reviews from Nature Journals*. World Scientific, 2010, pp. 11–19.
- [53] T. Liang, S. R. Phillpot, and S. B. Sinnott, "Parameterization of a reactive many-body potential for mos systems," *Physical Review B*, vol. 79, no. 24, p. 245 110, 2009.
- [54] D. W. Brenner, O. A. Shenderova, J. A. Harrison, S. J. Stuart, B. Ni, and S. B. Sinnott, "A second-generation reactive empirical bond order (rebo) potential energy expression for hydrocarbons," *Journal of Physics: Condensed Matter*, vol. 14, no. 4, p. 783, 2002, ISSN: 0953-8984.
- [55] F. H. Stillinger and T. A. Weber, "Computer simulation of local order in condensed phases of silicon," *Physical Review B*, vol. 31, no. 8, p. 5262, 1985.
- [56] J. Tersoff, "New empirical approach for the structure and energy of covalent systems," *Physical Review B*, vol. 37, no. 12, p. 6991, 1988.
- [57] T Belytschko, S. Xiao, G. C. Schatz, and R. Ruoff, "Atomistic simulations of nanotube fracture," *Physical Review B*, vol. 65, no. 23, p. 235 430, 2002.
- [58] M. Wen, S. N. Shirodkar, P. Plech, E. Kaxiras, R. S. Elliott, and E. B. Tadmor, "A force-matching stillinger-weber potential for mos2: Parameterization and fisher information theory based sensitivity analysis," *Journal of Applied Physics*, vol. 122, no. 24, p. 244 301, 2017, ISSN: 0021-8979.
- [59] A. Rohskopf, H. R. Seyf, K. Gordiz, T. Tadano, and A. Henry, "Empirical interatomic potentials optimized for phonon properties," *NPJ Computational Materials*, vol. 3, no. 1, pp. 1–7, 2017, ISSN: 2057-3960.
- [60] B. W. Dodson, "Development of a many-body tersoff-type potential for silicon," *Physical Review B*, vol. 35, no. 6, p. 2795, 1987.
- [61] J. S. Arora, *Introduction to optimum design*. Elsevier, 2004, ISBN: 0080470254.
- [62] B. Narayanan, K. Sasikumar, Z.-G. Mei, A. Kinaci, F. G. Sen, M. J. Davis, S. K. Gray, M. K. Chan, and S. K. Sankaranarayanan, "Development of a modified embedded atom force field for zirconium nitride using multi-objective evolutionary optimization," *The Journal of Physical Chemistry C*, vol. 120, no. 31, pp. 17 475–17 483, 2016, ISSN: 1932-7447.

- [63] A. Mishra, S. Hong, P. Rajak, C. Sheng, K.-i. Nomura, R. K. Kalia, A. Nakano, and P. Vashishta, "Multiobjective genetic training and uncertainty quantification of reactive force fields," *Npj Computational Materials*, vol. 4, no. 1, pp. 1–7, 2018, ISSN: 2057-3960.
- [64] A. Kandemir, H. Yapicioglu, A. Kinaci, T. an, and C. Sevik, "Thermal transport properties of mos2 and mose2 monolayers," *Nanotechnology*, vol. 27, no. 5, p. 055 703, 2016, ISSN: 0957-4484.
- [65] A. Ostadhossein, A. Rahnamoun, Y. Wang, P. Zhao, S. Zhang, V. H. Crespi, and A. C. Van Duin, "Reaxff reactive force-field study of molybdenum disulfide (mos2)," *The Journal of Physical Chemistry Letters*, vol. 8, no. 3, pp. 631–640, 2017, ISSN: 1948-7185.
- [66] J.-W. Jiang, "Parametrization of stillingerweber potential based on valence force field model: Application to single-layer mos2 and black phosphorus," *Nanotechnology*, vol. 26, no. 31, p. 315 706, 2015, ISSN: 0957-4484.
- [67] L Lindsay and D. Broido, "Optimized tersoff and brenner empirical potential parameters for lattice dynamics and phonon thermal transport in carbon nanotubes and graphene," *Physical Review B*, vol. 81, no. 20, p. 205 441, 2010.
- [68] J.-W. Jiang, H. S. Park, and T. Rabczuk, "Molecular dynamics simulations of single-layer molybdenum disulphide (mos2): Stillinger-weber parametrization, mechanical properties, and thermal conductivity," *Journal of Applied Physics*, vol. 114, no. 6, p. 064 307, 2013, ISSN: 0021-8979.
- [69] J. D. Gale, "Gulp: A computer program for the symmetry-adapted simulation of solids," *Journal of the Chemical Society, Faraday Transactions*, vol. 93, no. 4, pp. 629–637, 1997.
- [70] R. A. Buckingham, "The classical equation of state of gaseous helium, neon and argon," *Proceedings of the Royal Society of London. Series A. Mathematical and Physical Sciences*, vol. 168, no. 933, pp. 264–283, 1938, ISSN: 0080-4630.
- [71] B. Radisavljevic, A. Radenovic, J. Brivio, I. V. Giacometti, and A. Kis, "Single-layer mos2 transistors," *Nature Nanotechnology*, vol. 6, no. 3, pp. 147–150, 2011, ISSN: 1748-3387.
- [72] W. Wu, L. Wang, R. Yu, Y. Liu, S. Wei, J. Hone, and Z. L. Wang, "Piezophototronic effect in singleatomiclayer mos2 for straingated flexible optoelectronics," *Advanced Materials*, vol. 28, no. 38, pp. 8463–8468, 2016, ISSN: 0935-9648.
- [73] K. S. Kumar, N. Choudhary, Y. Jung, and J. Thomas, "Recent advances in two-dimensional nanomaterials for supercapacitor electrode applications," *ACS Energy Letters*, vol. 3, no. 2, pp. 482–495, 2018, ISSN: 2380-8195.
- [74] D. Jariwala, V. K. Sangwan, L. J. Lauhon, T. J. Marks, and M. C. Hersam, "Emerging device applications for semiconducting two-dimensional transition metal dichalcogenides," *ACS Nano*, vol. 8, no. 2, pp. 1102–1120, 2014, ISSN: 1936-0851.
- [75] X. Gu and C. Zhao, "Thermal conductivity of single-layer mos2(1-x)se2x alloys from molecular dynamics simulations with a machine-learning-based interatomic potential," *Computational Materials Science*, vol. 165, pp. 74–81, 2019, ISSN: 0927-0256.

- [76] A. Apte, V. Kochat, P. Rajak, A. Krishnamoorthy, P. Manimunda, J. A. Hachtel, J. C. Idrobo, S. A. Syed Amanulla, P. Vashishta, and A. Nakano, "Structural phase transformation in strained monolayer mos2 alloy," *ACS Nano*, vol. 12, no. 4, pp. 3468–3476, 2018, ISSN: 1936-0851.
- [77] T. K. Patra, F. Zhang, D. S. Schulman, H. Chan, M. J. Cherukara, M. Terrones, S. Das, B. Narayanan, and S. K. Sankaranarayanan, "Defect dynamics in 2-d mos2 probed by using machine learning, atomistic simulations, and high-resolution microscopy," *ACS Nano*, vol. 12, no. 8, pp. 8006–8016, 2018, ISSN: 1936-0851.
- [78] E. B. Tadmor and R. E. Miller, *Modeling materials: Continuum, atomistic and multiscale techniques*. Cambridge University Press, 2011, ISBN: 1139500651.
- [79] A. Gron, *Hands-on machine learning with Scikit-Learn, Keras, and TensorFlow: Concepts, tools, and techniques to build intelligent systems*. O'Reilly Media, 2019, ISBN: 1492032611.
- [80] Y.-C. Lin, D. O. Dumcenco, Y.-S. Huang, and K. Suenaga, "Atomic mechanism of the semiconducting-to-metallic phase transition in single-layered mos2," *Nature nanotechnology*, vol. 9, no. 5, pp. 391–396, 2014, ISSN: 1748-3395.
- [81] H. Ishibuchi, R. Imada, Y. Setoguchi, and Y. Nojima, "Performance comparison of nsga-ii and nsga-iii on various many-objective test problems," in *2016 IEEE Congress on Evolutionary Computation (CEC)*, IEEE, pp. 3045–3052, ISBN: 1509006230.
- [82] F.-Y. Lin and A. D. MacKerell Jr, "Polarizable empirical force field for halogen-containing compounds based on the classical drude oscillator," *Journal of Chemical Theory and Computation*, vol. 14, no. 2, pp. 1083–1098, 2018, ISSN: 1549-9618.
- [83] K. Vanommeslaeghe, E. Hatcher, C. Acharya, S. Kundu, S. Zhong, J. Shim, E. Darian, O. Guvench, P Lopes, and I. Vorobyov, "Charmm general force field: A force field for druglike molecules compatible with the charmm allatom additive biological force fields," *Journal of Computational Chemistry*, vol. 31, no. 4, pp. 671–690, 2010, ISSN: 0192-8651.
- [84] D. K. Saxena, J. A. Duro, A. Tiwari, K. Deb, and Q. Zhang, "Objective reduction in many-objective optimization: Linear and nonlinear algorithms," *IEEE Transactions on Evolutionary Computation*, vol. 17, no. 1, pp. 77–99, 2012, ISSN: 1089-778X.
- [85] X. Gu and R. Yang, "Phonon transport in single-layer transition metal dichalcogenides: A first-principles study," *Applied Physics Letters*, vol. 105, no. 13, p. 131 903, 2014, ISSN: 0003-6951.
- [86] X. Zhang, D. Sun, Y. Li, G.-H. Lee, X. Cui, D. Chenet, Y. You, T. F. Heinz, and J. C. Hone, "Measurement of lateral and interfacial thermal conductivity of single-and bilayer mos2 and mose2 using refined optothermal raman technique," *ACS Applied Materials & Interfaces*, vol. 7, no. 46, pp. 25 923–25 929, 2015, ISSN: 1944-8244.
- [87] A. Croy, "Bending rigidities and universality of flexural modes in 2d crystals," *Journal of Physics: Materials*, vol. 3, no. 2, 02LT03, 2020, ISSN: 2515-7639.

- [88] A. Jaramillo-Botero, S. Naserifar, and W. A. Goddard III, "General multiobjective force field optimization framework, with application to reactive force fields for silicon carbide," *Journal of Chemical Theory and Computation*, vol. 10, no. 4, pp. 1426–1439, 2014, ISSN: 1549-9618.
- [89] R. M. Betz and R. C. Walker, "Paramfit: Automated optimization of force field parameters for molecular dynamics simulations," *Journal of computational chemistry*, vol. 36, no. 2, pp. 79–87, 2015, ISSN: 0192-8651.
- [90] K. Chenoweth, A. C. Van Duin, and W. A. Goddard, "Reaxff reactive force field for molecular dynamics simulations of hydrocarbon oxidation," *The Journal of Physical Chemistry A*, vol. 112, no. 5, pp. 1040–1053, 2008, ISSN: 1089-5639.
- [91] J. P. Larentzos, B. M. Rice, E. F. Byrd, N. S. Weingarten, and J. V. Lill, "Parameterizing complex reactive force fields using multiple objective evolutionary strategies (moes). part 1: Reaxff models for cyclotrimethylene trinitramine (rdx) and 1, 1-diamino-2, 2-dinitroethene (fox-7)," *Journal of chemical theory and computation*, vol. 11, no. 2, pp. 381–391, 2015, ISSN: 1549-9618.
- [92] J. Lin, S. T. Pantelides, and W. Zhou, "Vacancy-induced formation and growth of inversion domains in transition-metal dichalcogenide monolayer," *ACS Nano*, vol. 9, no. 5, pp. 5189–5197, 2015, ISSN: 1936-0851.
- [93] D. Hull and D. J. Bacon, *Introduction to dislocations*. Elsevier, Amsterdam, Netherlands, 2011, vol. 37, ISBN: 008096673X.
- [94] J. Jiang, T. Xu, J. Lu, L. Sun, and Z. Ni, "Defect engineering in 2d materials: Precise manipulation and improved functionalities," *Research*, vol. 2019, p. 4 641 739, 2019, ISSN: 2639-5274.
- [95] H. Nan, Z. Wang, W. Wang, Z. Liang, Y. Lu, Q. Chen, D. He, P. Tan, F. Miao, and X. Wang, "Strong photoluminescence enhancement of mos2 through defect engineering and oxygen bonding," *ACS Nano*, vol. 8, no. 6, pp. 5738–5745, 2014, ISSN: 1936-0851.
- [96] S. A. Han, T. Kim, S. K. Kim, K. H. Lee, H. Park, J. Lee, and S. Kim, "Pointdefectpassivated mos2 nanosheetbased high performance piezoelectric nanogenerator," *Advanced Materials*, vol. 30, no. 21, p. 1 800 342, 2018, ISSN: 0935-9648.
- [97] P. Lin, L. Zhu, D. Li, and Z. L. Wang, "Defect repair for enhanced piezo-phototronic mos2 flexible phototransistors," *Journal of Materials Chemistry C*, vol. 7, no. 46, pp. 14 731–14 738, 2019.
- [98] T. T. Tran, K. Bray, M. J. Ford, M. Toth, and I. Aharonovich, "Quantum emission from hexagonal boron nitride monolayers," *Nature Nanotechnology*, vol. 11, no. 1, pp. 37–41, 2016, ISSN: 1748-3395.
- [99] G. Grosso, H. Moon, B. Lienhard, S. Ali, D. K. Efetov, M. M. Furchi, P. Jarillo-Herrero, M. J. Ford, I. Aharonovich, and D. Englund, "Tunable and high-purity room temperature single-photon emission from atomic defects in hexagonal boron nitride," *Nature Communications*, vol. 8, no. 1, pp. 1–8, 2017, ISSN: 2041-1723.

- [100] Y. Meng, C. Ling, R. Xin, P. Wang, Y. Song, H. Bu, S. Gao, X. Wang, F. Song, and J. Wang, "Repairing atomic vacancies in single-layer mose2 field-effect transistor and its defect dynamics," *Npj Quantum Materials*, vol. 2, no. 1, pp. 1–5, 2017, ISSN: 2397-4648.
- [101] H.-P. Komsa, J. Kotakoski, S. Kurasch, O. Lehtinen, U. Kaiser, and A. V. Krasheninnikov, "Two-dimensional transition metal dichalcogenides under electron irradiation: Defect production and doping," *Physical Review Letters*, vol. 109, no. 3, p. 035 503, 2012.
- [102] H.-P. Komsa, S. Kurasch, O. Lehtinen, U. Kaiser, and A. V. Krasheninnikov, "From point to extended defects in two-dimensional mos2: Evolution of atomic structure under electron irradiation," *Physical Review B*, vol. 88, no. 3, p. 035 301, 2013.
- [103] S. Kretschmer, T. Lehnert, U. Kaiser, and A. V. Krasheninnikov, "Formation of defects in two-dimensional mos2 in the transmission electron microscope at electron energies below the knock-on threshold: The role of electronic excitations," *Nano Letters*, vol. 20, no. 4, pp. 2865–2870, 2020, ISSN: 1530-6984.
- [104] Y. Shen, T. Xu, X. Tan, L. He, K. Yin, N. Wan, and L. Sun, "In situ repair of 2d chalcogenides under electron beam irradiation," *Advanced Materials*, vol. 30, no. 14, p. 1 705 954, 2018, ISSN: 0935-9648.
- [105] J. Zhao, H. Nam, T. H. Ly, S. J. Yun, S. Kim, S. Cho, H. Yang, and Y. H. Lee, "Chain vacancies in 2d crystals," *Small*, vol. 13, no. 1, p. 1 601 930, 2017, ISSN: 1613-6810.
- [106] J. P. Thiruraman, P. Masih Das, and M. Drndi, "Irradiation of transition metal dichalcogenides using a focused ion beam: Controlled singleatom defect creation," *Advanced Functional Materials*, vol. 29, no. 52, p. 1 904 668, 2019, ISSN: 1616-301X.
- [107] J. Hong, Z. Hu, M. Probert, K. Li, D. Lv, X. Yang, L. Gu, N. Mao, Q. Feng, and L. Xie, "Exploring atomic defects in molybdenum disulphide monolayers," *Nature Communications*, vol. 6, no. 1, pp. 1–8, 2015, ISSN: 2041-1723.
- [108] N. Alem, R. Erni, C. Kisielowski, M. D. Rossell, P. Hartel, B. Jiang, W. Gannett, and A. Zettl, "Vacancy growth and migration dynamics in atomically thin hexagonal boron nitride under electron beam irradiation," *Physica status solidi (RRL) Rapid Research Letters*, vol. 5, no. 8, pp. 295–297, 2011, ISSN: 1862-6254.
- [109] Y. Yang, X. Li, M. Wen, E. Hacıoğlu, W. Chen, Y. Gong, J. Zhang, B. Li, W. Zhou, P. M. Ajayan, Q. Chen, T. Zhu, and J. Lou, "Brittle fracture of 2d mose2," *Advanced Materials*, vol. 29, no. 2, p. 1 604 201, 2017, ISSN: 0935-9648.
- [110] R. Balluffi, "Grain boundary diffusion mechanisms in metals," *Metallurgical Transactions B*, vol. 13, no. 4, pp. 527–553, 1982, ISSN: 0360-2141.
- [111] I. M. Lifshitz and V. V. Slyozov, "The kinetics of precipitation from supersaturated solid solutions," *Journal of physics and chemistry of solids*, vol. 19, no. 1-2, pp. 35–50, 1961, ISSN: 0022-3697.

- [112] C. C. Battaile, “The kinetic monte carlo method: Foundation, implementation, and application,” *Computer Methods in Applied Mechanics and Engineering*, vol. 197, no. 41-42, pp. 3386–3398, 2008, ISSN: 0045-7825.
- [113] Y. Cai, S. Chen, J. Gao, G. Zhang, and Y.-W. Zhang, “Evolution of intrinsic vacancies and prolonged lifetimes of vacancy clusters in black phosphorene,” *Nanoscale*, vol. 11, no. 43, pp. 20 987–20 995, 2019.
- [114] A. Carpio and L. Bonilla, “Periodized discrete elasticity models for defects in graphene,” *Physical review B*, vol. 78, no. 8, p. 085 406, 2008.
- [115] J. Kotakoski, C. Mangler, and J. C. Meyer, “Imaging atomic-level random walk of a point defect in graphene,” *Nature Communications*, vol. 5, no. 1, pp. 1–5, 2014, ISSN: 2041-1723.
- [116] J. Hong, Y. Pan, Z. Hu, D. Lv, C. Jin, W. Ji, J. Yuan, and Z. Zhang, “Direct imaging of kinetic pathways of atomic diffusion in monolayer molybdenum disulfide,” *Nano Letters*, vol. 17, no. 6, pp. 3383–3390, 2017, ISSN: 1530-6984.
- [117] Y. Wang, T. Wakasugi, S. Isobe, N. Hashimoto, and S. Ohnuki, “Interaction of electrons with light metal hydrides in the transmission electron microscope,” *Journal of Electron Microscopy*, vol. 63, no. 6, pp. 437–447, 2014, ISSN: 0022-0744.
- [118] J. Madsen, P. Liu, J. B. Wagner, T. W. Hansen, and J. Schitz, “Accuracy of surface strain measurements from transmission electron microscopy images of nanoparticles,” *Advanced structural and chemical imaging*, vol. 3, no. 1, pp. 1–12, 2017, ISSN: 2198-0926.
- [119] T. H. Courtney, *Mechanical behavior of materials*. Waveland Press, 2005, ISBN: 1478608382.
- [120] W. Zhou, X. Zou, S. Najmaei, Z. Liu, Y. Shi, J. Kong, J. Lou, P. M. Ajayan, B. I. Yakobson, and J.-C. Idrobo, “Intrinsic structural defects in monolayer molybdenum disulfide,” *Nano letters*, vol. 13, no. 6, pp. 2615–2622, 2013, ISSN: 1530-6984.
- [121] M. Mahjouri-Samani, L. Liang, A. Oyedele, Y.-S. Kim, M. Tian, N. Cross, K. Wang, M.-W. Lin, A. Boulesbaa, and C. M. Rouleau, “Tailoring vacancies far beyond intrinsic levels changes the carrier type and optical response in monolayer mose2 x crystals,” *Nano letters*, vol. 16, no. 8, pp. 5213–5220, 2016, ISSN: 1530-6984.
- [122] T. L. Anderson, *Fracture mechanics: Fundamentals and applications*. CRC press, 2017, ISBN: 1498728146.
- [123] F. W. DelRio, R. F. Cook, and B. L. Boyce, “Fracture strength of micro-and nano-scale silicon components,” *Applied Physics Reviews*, vol. 2, no. 2, p. 021 303, 2015, ISSN: 1931-9401.
- [124] F. Barthelat and H. Espinosa, “An experimental investigation of deformation and fracture of nacre-mother of pearl,” *Experimental Mechanics*, vol. 47, no. 3, pp. 311–324, 2007, ISSN: 1741-2765.

- [125] C.-S. Lee, B. Cline, S. Sinha, G. Yeric, and H.-S. P. Wong, “32-bit processor core at 5-nm technology: Analysis of transistor and interconnect impact on vlsi system performance,” in *2016 IEEE International Electron Devices Meeting (IEDM)*, IEEE, pp. 28.3. 1–28.3. 4, ISBN: 1509039023.
- [126] K. S. Novoselov, A. K. Geim, S. V. Morozov, D.-e. Jiang, Y. Zhang, S. V. Dubonos, I. V. Grigorieva, and A. A. Firsov, “Electric field effect in atomically thin carbon films,” *Science*, vol. 306, no. 5696, pp. 666–669, 2004, ISSN: 0036-8075.
- [127] J. Sohn, S. Lee, Z. Jiang, H.-Y. Chen, and H.-S. P. Wong, “Atomically thin graphene plane electrode for 3d rram,” in *2014 IEEE International Electron Devices Meeting*, IEEE, pp. 5.3. 1–5.3. 4, ISBN: 1479980013.
- [128] D. Akinwande, C. Huyghebaert, C.-H. Wang, M. I. Serna, S. Goossens, L.-J. Li, H.-S. P. Wong, and F. H. Koppens, “Graphene and two-dimensional materials for silicon technology,” *Nature*, vol. 573, no. 7775, pp. 507–518, 2019, ISSN: 1476-4687.
- [129] L. Huang, F. Zheng, Q. Deng, Q. H. Thi, L. W. Wong, Y. Cai, N. Wang, C.-S. Lee, S. P. Lau, and M. Chhowalla, “In situ scanning transmission electron microscopy observations of fracture at the atomic scale,” *Physical Review Letters*, vol. 125, no. 24, p. 246 102, 2020.
- [130] Y. Yang, Z. Song, G. Lu, Q. Zhang, B. Zhang, B. Ni, C. Wang, X. Li, L. Gu, and X. Xie, “Intrinsic toughening and stable crack propagation in hexagonal boron nitride,” *Nature*, vol. 594, no. 7861, pp. 57–61, 2021, ISSN: 1476-4687.
- [131] P. Zhang, L. Ma, F. Fan, Z. Zeng, C. Peng, P. E. Loya, Z. Liu, Y. Gong, J. Zhang, X. Zhang, P. M. Ajayan, T. Zhu, and J. Lou, “Fracture toughness of graphene,” *Nature Communications*, vol. 5, p. 3782, 2014, ISSN: 2041-1723.
- [132] F. Z. Li, C. F. Shih, and A Needleman, “A comparison of methods for calculating energy release rates,” *Engineering Fracture Mechanics*, vol. 21, no. 2, pp. 405–421, 1985, ISSN: 0013-7944.
- [133] J. R. Rice, “A path independent integral and the approximate analysis of strain concentration by notches and cracks,” *Journal of applied mechanics*, vol. 35, no. 2, pp. 379–386, 1968, ISSN: 0021-8936.
- [134] T. H. Dunning and P. J. Hay, “Methods of electronic structure theory,” *Modern Theoretical Chemistry*, vol. 3, pp. 1–28, 1977.
- [135] S. Grimme, “Semiempirical gga?type density functional constructed with a long?range dispersion correction,” *Journal of Computational Cshemistry*, vol. 27, no. 15, pp. 1787–1799, 2006, ISSN: 0192-8651.
- [136] A. P. Thompson, H. M. Aktulga, R. Berger, D. S. Bolintineanu, W. M. Brown, P. S. Crozier, P. J. in’t Veld, A. Kohlmeyer, S. G. Moore, and T. D. Nguyen, “Lammmps-a flexible simulation tool for particle-based materials modeling at the atomic, meso, and continuum scales,” *Computer Physics Communications*, p. 108 171, 2021, ISSN: 0010-4655.

- [137] M. J. Powell, “The bobyqa algorithm for bound constrained optimization without derivatives,” *Cambridge NA Report NA2009/06*, University of Cambridge, Cambridge, pp. 26–46, 2009.
- [138] F. Biscani and D. Izzo, “A parallel global multiobjective framework for optimization: Pagmo,” *Journal of Open Source Software*, vol. 5, no. 53, p. 2338, 2020, ISSN: 2475-9066.
- [139] R. E. Jones and J. A. Zimmerman, “The construction and application of an atomistic j-integral via hardy estimates of continuum fields,” *Journal of the Mechanics and Physics of Solids*, vol. 58, no. 9, pp. 1318–1337, 2010, ISSN: 0022-5096.
- [140] F. Jacob and B. Ted, *A first course in finite elements*. Wiley, 2007.
- [141] P Scott, “A review of irradiation assisted stress corrosion cracking,” *Journal of Nuclear Materials*, vol. 211, no. 2, pp. 101–122, 1994, ISSN: 0022-3115.
- [142] X. Zhang, X. Zhang, P. M. Ajayan, J. Wen, and H. D. Espinosa, “Edge-mediated annihilation of vacancy clusters in monolayer molybdenum diselenide (mose2) under electron beam irradiation,” *Small*, vol. n/a, no. n/a, p. 2105194, ISSN: 1613-6810.
- [143] Z. P. Bazant and M. T. Kazemi, “Size effect on diagonal shear failure of beams without stirrups,” *ACI Structural Journal*, vol. 88, no. 3, pp. 268–276, 1991, ISSN: 0889-3241.
- [144] X. Li, Z. Ding, C. Liu, S. Bao, and Z. Gao, “Evaluation and comparison of fracture toughness for metallic materials in different conditions by astm and iso standards,” *International Journal of Pressure Vessels and Piping*, vol. 187, p. 104189, 2020, ISSN: 0308-0161.
- [145] J. Hutchinson, “Singular behaviour at the end of a tensile crack in a hardening material,” *Journal of the Mechanics and Physics of Solids*, vol. 16, no. 1, pp. 13–31, 1968, ISSN: 0022-5096.
- [146] N. C. Admal and E. B. Tadmor, “A unified interpretation of stress in molecular systems,” *Journal of Elasticity*, vol. 100, no. 1, pp. 63–143, 2010, ISSN: 1573-2681.
- [147] V. A. Kuzkin, “Comment on the calculation of forces for multibody interatomic potentials,” *ArXiv preprint arXiv:1003.5267*, 2010.
- [148] M. S. Elapolu, A. Tabarraei, X. Wang, and D. E. Spearot, “Fracture mechanics of multi-layer molybdenum disulfide,” *Engineering Fracture Mechanics*, vol. 212, pp. 1–12, 2019, ISSN: 0013-7944.
- [149] R. A. Soler-Crespo, L. Mao, J. Wen, H. Nguyen, X. Zhang, X. Wei, J. Huang, S. T. Nguyen, and H. D. Espinosa, “Atomically thin polymer layer enhances toughness of graphene oxide monolayers,” *Matter*, in press.
- [150] X. Zhang, H. Nguyen, M. Daly, S. T. Nguyen, and H. D. Espinosa, “Nanoscale toughening of ultrathin graphene oxide-polymer composites: Mechanochemical insights into hydrogen-bonding/van der waals interactions, polymer chain alignment, and steric parameters,” *Nanoscale*, vol. 11, no. 25, pp. 12305–12316, 2019.

- [151] X. Wei, L. Mao, R. A. Soler-Crespo, J. T. Paci, J. Huang, S. T. Nguyen, and H. D. Espinosa, "Plasticity and ductility in graphene oxide through a mechanochemically induced damage tolerance mechanism," *Nature Communications*, vol. 8, p. 14 488, 2017, ISSN: 2041-1723.
- [152] A. Castellanos-Gomez, M. Buscema, R. Molenaar, V. Singh, L. Janssen, H. S. Van Der Zant, and G. A. Steele, "Deterministic transfer of two-dimensional materials by all-dry viscoelastic stamping," *2D Materials*, vol. 1, no. 1, p. 011 002, 2014, ISSN: 2053-1583.
- [153] R. Rojacee and R. Shahbazian-Yassar, "Two-dimensional materials to address the lithium battery challenges," *ACS Nano*, vol. 14, no. 3, pp. 2628–2658, 2020, ISSN: 1936-0851.
- [154] C. W. Lee, J. M. Suh, and H. W. Jang, "Chemical sensors based on two-dimensional (2d) materials for selective detection of ions and molecules in liquid," *Frontiers in chemistry*, vol. 7, p. 708, 2019, ISSN: 2296-2646.
- [155] S. Das, A. Sebastian, E. Pop, C. J. McClellan, A. D. Franklin, T. Grasser, T. Knobloch, Y. Illarionov, A. V. Penumatcha, and J. Appenzeller, "Transistors based on two-dimensional materials for future integrated circuits," *Nature Electronics*, vol. 4, no. 11, pp. 786–799, 2021, ISSN: 2520-1131.
- [156] S. D. Sarma, S. Adam, E. Hwang, and E. Rossi, "Electronic transport in two-dimensional graphene," *Reviews of modern physics*, vol. 83, no. 2, p. 407, 2011.
- [157] C. Lee, X. Wei, J. W. Kysar, and J. Hone, "Measurement of the elastic properties and intrinsic strength of monolayer graphene," *Science*, vol. 321, no. 5887, pp. 385–388, 2008, ISSN: 0036-8075.
- [158] R. A. Soler-Crespo, W. Gao, P. Xiao, X. Wei, J. T. Paci, G. Henkelman, and H. D. Espinosa, "Engineering the mechanical properties of monolayer graphene oxide at the atomic level," *Journal of Physical Chemistry Letters*, vol. 7, no. 14, pp. 2702–2707, 2016, ISSN: 1948-7185.
- [159] E. F. Hacıoğlu, Y. Yang, B. Ni, Y. Li, X. Li, Q. Chen, H. Guo, J. M. Tour, H. Gao, and J. Lou, "Toughening graphene by integrating carbon nanotubes," *Acs Nano*, vol. 12, no. 8, pp. 7901–7910, 2018, ISSN: 1936-0851.
- [160] D. Akinwande, C. J. Brennan, J. S. Bunch, P. Egberts, J. R. Felts, H. Gao, R. Huang, J.-S. Kim, T. Li, and Y. Li, "A review on mechanics and mechanical properties of 2d materialsgraphene and beyond," *Extreme Mechanics Letters*, vol. 13, pp. 42–77, 2017, ISSN: 2352-4316.
- [161] S. Wan, J. Peng, L. Jiang, and Q. Cheng, "Bioinspired graphene-based nanocomposites and their application in flexible energy devices," *Advanced Materials*, vol. 28, no. 36, pp. 7862–7898, 2016, ISSN: 0935-9648.
- [162] M. Daly, M. Reeve, and C. V. Singh, "Effects of topological point reconstructions on the fracture strength and deformation mechanisms of graphene," *Computational Materials Science*, vol. 97, pp. 172–180, 2015, ISSN: 0927-0256.

- [163] K. Erickson, R. Erni, Z. Lee, N. Alem, W. Gannett, and A. Zettl, "Determination of the local chemical structure of graphene oxide and reduced graphene oxide," *Advanced Materials*, vol. 22, no. 40, pp. 4467–4472, 2010, ISSN: 0935-9648.
- [164] A. Lerf, H. He, M. Forster, and J. Klinowski, "Structure of graphite oxide revisited," *Journal of Physical Chemistry B*, vol. 102, no. 23, pp. 4477–4482, 1998, ISSN: 1089-5647.
- [165] M. Daly, C. Cao, H. Sun, Y. Sun, T. Filleter, and C. V. Singh, "Interfacial shear strength of multilayer graphene oxide films," *Acs Nano*, vol. 10, no. 2, pp. 1939–1947, 2016, ISSN: 1936-0851.
- [166] R. A. Soler-Crespo, W. Gao, L. Mao, H. T. Nguyen, M. R. Roenbeck, J. T. Paci, J. Huang, S. T. Nguyen, and H. D. Espinosa, "The role of water in mediating interfacial adhesion and shear strength in graphene oxide," *Acs Nano*, vol. 12, no. 6, pp. 6089–6099, 2018, ISSN: 1936-0851.
- [167] C. Cao, M. Daly, C. V. Singh, Y. Sun, and T. Filleter, "High strength measurement of monolayer graphene oxide," *Carbon*, vol. 81, pp. 497–504, 2015, ISSN: 0008-6223.
- [168] Z. Meng, R. A. Soler-Crespo, W. Xia, W. Gao, L. Ruiz, H. D. Espinosa, and S. Keten, "A coarse-grained model for the mechanical behavior of graphene oxide," *Carbon*, vol. 117, pp. 476–487, 2017, ISSN: 0008-6223.
- [169] J. T. Paci, T. Belytschko, and G. C. Schatz, "Computational studies of the structure, behavior upon heating, and mechanical properties of graphite oxide," *Journal of Physical Chemistry C*, vol. 111, no. 49, pp. 18 099–18 111, 2007, ISSN: 1932-7447.
- [170] K. W. Putz, O. C. Compton, M. J. Palmeri, S. T. Nguyen, and L. C. Brinson, "High-nanofiller-content graphene oxide-polymer nanocomposites via vacuum-assisted self-assembly," *Advanced Functional Materials*, vol. 20, no. 19, pp. 3322–3329, 2010, ISSN: 1616-301x.
- [171] Y. Wang, R. Ma, K. Hu, S. Kim, G. Fang, Z. Shao, and V. V. Tsukruk, "Dramatic enhancement of graphene oxide/silk nanocomposite membranes: Increasing toughness, strength, and young's modulus via annealing of interfacial structures," *Acs Applied Materials & Interfaces*, vol. 8, no. 37, pp. 24 962–24 973, 2016, ISSN: 1944-8244.
- [172] S. Wan, J. Peng, Y. Li, H. Hu, L. Jiang, and Q. Cheng, "Use of synergistic interactions to fabricate strong, tough, and conductive artificial nacre based on graphene oxide and chitosan," *Acs Nano*, vol. 9, no. 10, pp. 9830–9836, 2015, ISSN: 1936-0851.
- [173] K. Vanommeslaeghe, E. P. Raman, and A. D. MacKerell, "Automation of the charmm general force field (cgenff) ii: Assignment of bonded parameters and partial atomic charges," *Journal of Chemical Information and Modeling*, vol. 52, no. 12, pp. 3155–3168, 2012, ISSN: 1549-9596.
- [174] W. Yu, X. He, K. Vanommeslaeghe, and A. D. MacKerell Jr, "Extension of the charmm general force field to sulfonylcontaining compounds and its utility in biomolecular simulations," *Journal of computational chemistry*, vol. 33, no. 31, pp. 2451–2468, 2012, ISSN: 0192-8651.

- [175] A. F. Fonseca, T. Liang, D. Zhang, K. Choudhary, and S. B. Sinnott, "Probing the accuracy of reactive and non-reactive force fields to describe physical and chemical properties of graphene-oxide," *Computational Materials Science*, vol. 114, pp. 236–243, 2016, ISSN: 0927-0256.
- [176] S. Plimpton, "Fast parallel algorithms for short-range molecular-dynamics," *Journal of Computational Physics*, vol. 117, no. 1, pp. 1–19, 1995, ISSN: 0021-9991.
- [177] A. Luzar and D. Chandler, "Hydrogen-bond kinetics in liquid water," *Nature*, vol. 379, no. 6560, pp. 55–57, 1996, ISSN: 0028-0836.
- [178] S. Keten and M. J. Buehler, "Geometric confinement governs the rupture strength of h-bond assemblies at a critical length scale," *Nano Letters*, vol. 8, no. 2, pp. 743–748, 2008, ISSN: 1530-6984.
- [179] S. Wan, H. Hu, J. Peng, Y. Li, Y. Fan, L. Jiang, and Q. Cheng, "Nacre-inspired integrated strong and tough reduced graphene oxide-poly(acrylic acid) nanocomposites," *Nanoscale*, vol. 8, no. 10, pp. 5649–5656, 2016, ISSN: 2040-3364.
- [180] Y. Wu, R. Cao, G. Wu, W. Huang, Z. Chen, X. Yang, and Y. Tu, "From ultratough artificial nacre to elastomer: Poly (n-butyl acrylate) grafted graphene oxide nanocomposites," *Composites Part a-Applied Science and Manufacturing*, vol. 88, pp. 156–164, 2016, ISSN: 1359-835x.
- [181] A. M. Diez-Pascual and A. L. Diez-Vicente, "Poly(propylene fumarate)/polyethylene glycol-modified graphene oxide nanocomposites for tissue engineering," *Acs Applied Materials & Interfaces*, vol. 8, no. 28, pp. 17 902–17 914, 2016, ISSN: 1944-8244.
- [182] R. Auhl, R. Everaers, G. S. Grest, K. Kremer, and S. J. Plimpton, "Equilibration of long chain polymer melts in computer simulations," *Journal of Chemical Physics*, vol. 119, no. 24, pp. 12 718–12 728, 2003, ISSN: 0021-9606.
- [183] V. C. Li, Y. Wang, and S. Backer, "A micromechanical model of tension-softening and bridging toughening of short random fiber reinforced brittle matrix composites," *Journal of the Mechanics and Physics of Solids*, vol. 39, no. 5, pp. 607–625, 1991, ISSN: 0022-5096.
- [184] M. Rubinstein and R. H. Colby, *Polymer physics*. Oxford University Press, New York, 2003, vol. 23.
- [185] K. Karatasos and G. Kritikos, "Characterization of a graphene oxide/poly(acrylic acid) nanocomposite by means of molecular dynamics simulations," *Rsc Advances*, vol. 6, no. 111, pp. 109 267–109 277, 2016, ISSN: 2046-2069.
- [186] A. Milchev and K. Binder, "Static and dynamic properties of adsorbed chains at surfaces: Monte carlo simulation of a bead-spring model," *Macromolecules*, vol. 29, no. 1, pp. 343–354, 1996, ISSN: 0024-9297.
- [187] G Bao and Z Suo, "Remarks on crack-bridging concepts," *Applied Mechanics Reviews*, vol. 45, no. 8, pp. 355–366, 1992, ISSN: 0003-6900.

- [188] I. Benedetti, H. Nguyen, R. A. Soler-Crespo, W. Gao, L. Mao, A. Ghasemi, J. Wen, S. Nguyen, and H. D. Espinosa, "Formulation and validation of a reduced order model of 2d materials exhibiting a two-phase microstructure as applied to graphene oxide," *Journal of the Mechanics and Physics of Solids*, vol. 112, pp. 66–88, 2018, ISSN: 0022-5096.
- [189] D. C. Montgomery, *Design and analysis of experiments*. John Wiley & Sons, 2017, ISBN: 1119113474.
- [190] S. H. Cheng and C. T. Sun, "Size-dependent fracture toughness of nanoscale structures: Crack-tip stress approach in molecular dynamics," *Journal of Nanomechanics and Micromechanics*, vol. 4, no. 4, A4014001, 2013, ISSN: 2153-5434.
- [191] A. Erbas, D. Horinek, and R. R. Netz, "Viscous friction of hydrogen-bonded matter," *Journal of the American Chemical Society*, vol. 134, no. 1, pp. 623–630, 2012.
- [192] R. Sinko and S. Keten, "Traction-separation laws and stick-slip shear phenomenon of interfaces between cellulose nanocrystals," *Journal of the Mechanics and Physics of Solids*, vol. 78, pp. 526–539, 2015, ISSN: 0022-5096.
- [193] L. Cao, Y. Wang, P. Dong, S. Vinod, J. T. Tijerina, P. M. Ajayan, Z. Xu, and J. Lou, "Interphase induced dynamic self-stiffening in graphene-based polydimethylsiloxane nanocomposites," *Small*, vol. 12, no. 27, pp. 3723–3731, 2016, ISSN: 1613-6810.
- [194] P. S. Owuor, C. F. Woellner, T. Li, S. Vinod, S. Ozden, S. Kosolwattana, S. Bhowmick, L. X. Duy, R. V. Salvatierra, B. Wei, S. A. S. Asif, J. M. Tour, R. Vajtai, J. Lou, D. S. Galvao, C. S. Tiwary, and P. M. Ajayan, "High toughness in ultralow density graphene oxide foam," *Advanced Materials Interfaces*, vol. 4, no. 10, p. 1700030, 2017, ISSN: 2196-7350.
- [195] O. C. Compton, S. W. Cranford, K. W. Putz, Z. An, L. C. Brinson, M. J. Buehler, and S. T. Nguyen, "Tuning the mechanical properties of graphene oxide paper and its associated polymer nanocomposites by controlling cooperative intersheet hydrogen bonding," *Acs Nano*, vol. 6, no. 3, pp. 2008–2019, 2012, ISSN: 1936-0851.
- [196] M. Zhang, X. Wang, C. Li, Y. Bai, B. Cheng, and Z. Li, "Effects of hydrogen bonding between mwcnt and pps on the properties of pps/mwcnt composites," *Rsc Advances*, vol. 6, no. 95, pp. 92378–92386, 2016, ISSN: 2046-2069.